Imperial College London

Wake Impacting on a Horizontal Axis Wind Turbine

David Andrew Hankin

Department of Aeronautics
Imperial College London
South Kensington Campus
London SW7 2AZ

Submitted in partial fulfilment of the requirements for the degree of Doctor of Philosophy of Imperial College London and the Diploma of Imperial College London

I hereby declare that I am the sole author of this thesis and that it has not been submitted in whole or in part for publication or any other academic degree or professional qualification. This thesis, to the best of my knowledge, does not infringe upon anyones copyright nor violate any proprietary rights and that any ideas, techniques, quotations, or any other material from the work of other people included in this thesis, published or otherwise, are fully acknowledged in accordance with the standard referencing practices.

David Hankin
October 29, 2014

The copyright of this thesis rests with the author and is made available under a Creative Commons Attribution Non-Commercial No Derivatives licence. Researchers are free to copy, distribute or transmit the thesis on the condition that they attribute it, that they do not use it for commercial purposes and that they do not alter, transform or build upon it. For any reuse or redistribution, researchers must make clear to others the licence terms of this work

Abstract

Offshore wind is set to contribute a significant portion of the UK's renewable energy production. In order to achieve this, installation costs must be reduced and energy density optimised, but this must be balanced with the increase in maintenance costs resulting from fatigue due to wake impact. The aim of this thesis is to investigate the effects of horizontal axis wind turbine wake impact on a downstream rotor.

A force-free wake implementation of the unsteady vortex lattice method has been developed in order to simulate the flow around the downstream rotor, including the effects of an upstream rotor wake, uncorrelated wind field and the dynamic inflow response of the turbine wake. In addition, a series of wind tunnel experiments were undertaken to characterise the wake of a horizontal axis wind turbine and measure time histories of the turbine thrust and blade root bending moments in uniform and turbulent inflow and upstream rotor wake impact.

Comparisons are made between the model and wind tunnel experiments for a range of flow cases: uniform inflow, turbulent inflow and operation in an upstream rotor wake at varying degrees of lateral offset. The upstream flow field is modelled on a Cartesian grid, following the assumption of frozen turbulence. For both the turbulent flow and upstream rotor wake, a simplified model is used as a starting point and then refined to better model the effect of turbulence.

Ambient turbulence is found to have minimal impact on the mean response of the rotor, suggesting that a linearised approach can be taken in the numerical modelling of turbulence effects. The simple model better predicts the low frequency response, but does not capture the per revolution frequencies identified by the refined model, which also better predicts the admittance.

The response of the rotor to an aligned upstream rotor wake is found to be dominated by the wake turbulence, although the proposed model does not reproduce the measured response. However, for laterally offset upstream rotor wakes the mean velocity deficit is the dominant factor and the model captures the response, including the shift to higher bending moment cycles which will contribute to increased fatigue.

Acknowledgments

First and foremost, I would like to thank my supervisor, Professor Mike Graham, for his preeminent knowledge and continual support and advice throughout the development of this thesis. His unequaled ability to elicit more thorough contemplation of my ideas and exposition will be appreciated for many years to come.

My gratitude to all the guys in the workshop, in particular Roland, Ian, Andy, Alan and Jon. Their assistance in the commissioning of my experiments and swift replacement of the odd stray turbine blade made the long hours spent in the Honda wind tunnel considerably less stressful.

I have made many friends during my time at Imperial, both within the department and beyond. Their camaraderie, whether in the Holland Club or the hills around the UK and Europe, made the whole experience considerably more enjoyable. Many thanks to my office mates Ben and Duncan for the many conversations over a cup of coffee. In particular, the long discussions with Duncan on the specifics of the vortex lattice method were most beneficial.

I would also like to thank my parents, Alison and Chris, for the continual support and assistance throughout my education, not least in the latter years of my undergraduate degree and ensuing PhD.

Finally, I reserve my deepest, sincere and most personal gratitude for my wife Anna, whose patience in the proof-reading of this thesis was invaluable and whose enduring love and support helped me survive the rigours of PhD life.

Contents

Abstract **3**

Acknowledgments **4**

List of Tables **7**

List of Figures **7**

Nomenclature **12**

1 Introduction and motivation **15**

1.1 Governing equations 16

1.2 Axis system 18

1.3 Turbine specification 18

1.4 Turbine parameters 21

1.5 Computational methods 21

1.6 Aims and objectives 25

1.7 Thesis overview 25

2 Horizontal axis wind turbine wakes: A review **27**

2.1 Atmospheric turbulence 27

2.2 Wake characteristics 32

2.3 Wake modelling 36

2.4 Wake impacting 51

2.5 Fatigue 52

2.6 Summary 56

3 Aeolus: An unsteady vortex lattice method wake model **58**

3.1 Boundary conditions 58

3.2 The Biot-Savart law 59

3.3 Vortex core 60

3.4 The vortex lattice method 62

3.5 Wake development 64
3.6 Aerodynamic loads 67
3.7 Wind field simulation 68
3.8 Convergence studies 72
3.9 Verification 74
3.10 Summary 84

4 Generating a validation database: Wind tunnel measurements 85
4.1 Experimental setup 85
4.2 Wake measurements 93
4.3 Turbine experiments 103
4.4 Summary 119

5 Ambient turbulence and wake impact: Modelling and discussion 121
5.1 Uniform flow 122
5.2 Ambient turbulence 127
5.3 Upstream rotor wake impact 136
5.4 Summary 148

6 Conclusions and future work 150
6.1 Ambient turbulence 151
6.2 Wake impact 152
6.3 Future work 153

References 155

A Calibrations 171
A.1 Strain gauges 171
A.2 Hot-wire 174
A.3 Tunnel 177

List of Tables

1.1 Experimental turbine blade specification. 19

2.1 Examples of field and wind tunnel investigations of HAWT rotor wakes. 33

5.1 Rotor harmonic frequencies. 132

A.1 Blade calibration load points. 172

List of Figures

1.1 Axis system definition. 18

1.2 Indicative performance curve for the modified Exemplar turbine used in the experiments. 20

2.1 Wake geometry. 37

3.1 Biot-Savart law geometric definitions. 60

3.2 Contours of variation in rotor coefficients with core parameters. . . . 62

3.3 Vortex lattice method discretisation. 63

3.4 Comparison of runtime and loads for wake freezing after one complete rotation. 66

3.5 Section definitions. 69

3.6 Contours of variation in rotor coefficients with panelling parameters. . 73

3.7 Contours of variation in rotor coefficients with time stepping parameters. 74

3.8 Comparison of steady lift curve slope with results of Graham (1971) . 75

3.9 Comparison of settled coefficients with Katz and Plotkin (2001) and Drela and Youngren (2014). 75

3.10 Comparison of impulse response with Wagner's function. 76

3.11 Comparison of impulse response with Katz and Plotkin (2001). 77

3.12 Comparison of response to pitching and heaving motion at $k = 1.0$ with the analytical results of Theodorsen (1935) and Garrick (1936). . 79

3.13 Comparison of heave response with Katz and Plotkin (2001). 80

3.14 Comparison of Aeolus with Blade Element Momentum (BEM) theory. 81

3.15 Comparison of time averaged induction factors from Aeolus and Blade Element Momentum (BEM) theory. 83

4.1 Schematic of experimental setup. 87

4.2 Fractal turbulence grid profiles. 91

4.3 Fractal grid turbulence spectrum. 92

4.4 Comparison between measured and von Kármán coherence behind fractal turbulence grid. 93

4.5 Comparison of wake profiles for varying Λ. 95

4.6 Comparison of lateral and vertical wake profiles. 98

4.7 Velocity deficit measured by fixed hot-wire for each separation distance. 99

4.8 Wake turbulence spectrum. 99

4.9 Comparison between measured and von Kármán coherence of the upstream rotor wake. 100

4.10 Combined flow profiles. 101

4.11 Cross-correlation of meandering wake velocities. 103

4.12 Comparison between turbulent and uniform flow thrust coefficients. . 107

4.13 Comparison between turbulent and uniform flow thrust moment RMS intensity. 107

4.14 Comparison between turbulent and uniform flow blade root bending moment coefficients. 107

4.15 Comparison between turbulent and uniform flow blade root bending moment RMS intensity. 108

4.16 Comparison between turbulent and uniform flow spectra from the thrust loading. 109

4.17 Comparison between turbulent and uniform flow spectra from the blade root bending moment. 110

4.18 Comparison between thrust coefficients for different upstream rotor lateral offsets. 114

4.19 Comparison between blade root bending moment coefficients for different upstream rotor lateral offsets. 114

4.20 Comparison between thrust moment RMS intensity for different upstream rotor lateral offsets. 114

4.21 Comparison between blade root bending moment RMS intensity for different upstream rotor lateral offsets. 115

4.22 Comparison between spectra for different upstream rotor lateral offsets from the thrust loading. 116

4.23 Comparison between flow spectra for different upstream rotor lateral offsets from the blade root bending moment. 117

4.24 Comparison of combined ambient and wake turbulence with individual cases. 120

5.1 Comparison between simulation and experimental thrust coefficient. . 124

5.2 Comparison between simulation and experimental blade root bending moment coefficient. 124

5.3 NACA 643618 Lift curve. ($\mathrm{Re} = 6.4 \times 10^4$). 124

5.4 Comparison between simulation and experimental location of equivalent load point. 125

5.5 Comparison between simulation and experimental thrust coefficient in turbulent flow. 130

5.6 Comparison between simulation and experimental blade root bending moment coefficient in turbulent flow. 130

5.7 Comparison between simulation and experimental thrust coefficient RMS in turbulent flow. 130

5.8 Comparison of simulation thrust coefficient admittance in correlated and uncorrelated turbulence at $\Lambda = 3$. 131

5.9 Comparison between simulation and experimental blade root bending moment coefficient RMS in turbulent flow. 131

5.10 Comparison between measurements and simulation turbulent flow blade root bending moment spectra and admittance. 133

5.11 Variation of wake induction in turbulent flow compared with local velocity. 134

5.12 Comparison of uniform and turbulent fatigue load histograms. 136

5.13 Wake centreline deficit quadratic fit. 138

5.14 Comparison of measurements with wake velocity deficit model. 138

5.15 Comparison between simulation and experimental thrust coefficient in an upstream rotor wake. 140

5.16 Comparison between simulation and experimental blade root bending moment coefficient in an upstream rotor wake. 140

5.17 Comparison between measurements and simulation of upstream rotor wake impact load time histories for increasing lateral offset. 141

5.18 Comparison between measurements and simulation of upstream rotor wake impact azimuthally binned loads for increasing lateral offset. . . 143

5.19 Azimuthal variation of wake induction at $\Lambda = 3$ for different laterally offsets. 145

5.20 Azimuthal variation of wake induction for a $\Delta y = 0.50D$ laterally offset wake for $\Lambda = 1 - 5$. 146

5.21 Comparison of wake impact fatigue load histograms for $\Lambda = 3$. 148

A.1 Blade strain gauge calibration. 173

A.2 Blade resonance spectrum. 173

A.3 Strut strain gauge calibration. 174

A.4 Strut resonance spectrum. 174

A.5 Hot-wire calibration: Uniform flow, Aligned upstream Rotor. 175

A.6 Hot-wire calibration: Uniform flow, $1D$ offset upstream Rotor. 176

A.7 Hot-wire calibration: Turbulent flow, Aligned upstream Rotor. 176

A.8 Hot-wire calibration: Turbulent flow, $1D$ offset upstream Rotor. . . . 176

A.9 Hot-wire calibration: Wake meandering. 177

A.10 Hot-wire calibration: Tunnel calibration. 177

A.11 Tunnel velocity calibration. 178

All figures in this thesis have been produced using a colour-blind safe, print friendly colour scheme as devised by Tol (2012). For further information, the reader is directed to his notes at `http://www.sron.nl/~pault/`.

Reproduction and digitisation of plots was accomplished using PlotDigitizer, available at `http://plotdigitizer.sourceforge.net`.

Roman Uppercase

A	Panel area	m^2
Æ	Aspect ratio	-
C	Influence coefficient	-
C_D	Drag coefficient	-
C_l	Sectional lift coefficient	-
C_L	Lift coefficient	-
C_{M_b}	Bending moment coefficient	-
C_P	Power coefficient	-
C_t	Sectional thrust coefficient	-
C_T	Thrust coefficient	-
D	Rotor diameter	m
F	Force	$\mathrm{kg\ m\ s}^{-2}$
I_u	Turbulence intensity	-
L	Lift	$\mathrm{kg\ m\ s}^{-2}$
L_x	Longitudinal length scale	m
M	Mach number	-
M_b	Blade root bending moment	$\mathrm{kg\ m}^2\ \mathrm{s}^{-2}$
P	Power	$\mathrm{kg\ m}^2\ \mathrm{s}^{-3}$
Q	Total velocity	$\mathrm{m\ s}^{-1}$
R	Blade radius	m
Re	Reynolds number	-
S	Spectral density	Hz^{-1}
T	Axial thrust	$\mathrm{kg\ m\ s}^{-2}$
$\mathbb{T}$	Stress Tensor	$\mathrm{kg\ m}^{-2}\ \mathrm{s}^{-2}$
U	Velocity	$\mathrm{m\ s}^{-1}$
U_∞	Free stream/reference velocity	$\mathrm{m\ s}^{-1}$
ΔU	Velocity deficit	-
V	Induced velocity	$\mathrm{m\ s}^{-1}$
W	Wind velocity	$\mathrm{m\ s}^{-1}$

Roman Lowercase

a	Axial induction factor	-
a'	Swirl induction factor	-
a_0	Lift curve slope	rad^{-1}
a_∞	Speed of sound	$\mathrm{m\ s}^{-1}$
b	Half chord	m
c	Chord	m
f	Frequency	Hz
Δf	Frequency spacing	Hz
g	Gravitational acceleration	$\mathrm{m\ s}^{-2}$
k	Reduced frequency	-
l	Filament length	m
m	Mass	kg
n	Panel normal vector	-
n_b	Number of blades	-
n_x	Number of chordwise nodes	-
n_y	Number of spanwise nodes	-
p	Pressure	$\mathrm{kg\ m}^{-1}\ \mathrm{s}^{-2}$
r	Radial distance	m
$r_\perp$	Perpendicular distance	m
r_c	Core radius	m
t	Time	s
u, v, w	Turbulence velocity components	$\mathrm{m\ s}^{-1}$
u^*	Friction velocity	$\mathrm{m\ s}^{-1}$
x, y, z	Coordinates	m
Δy	Lateral offset	m
Δz	Vertical offset	m

Greek

α	Incidence	rad
γ	Coherence	-
Γ	Circulation	$\mathrm{m}^2\ \mathrm{s}^{-1}$

θ	Angle	rad
λ	Local speed ratio	-
Λ	Tip speed ratio	-
μ	Dynamic viscosity	kg m^{-1} s^{-1}
ρ	Density	kg m^{-3}
σ	RMS (std. dev.) velocity	m s^{-1}
τ	Non-dimensional time	-
ϕ	Local inflow angle	rad
Φ	Velocity potential	m^2 s^{-1}
ψ	Azimuth	rad
ω	Angular frequency	rad s^{-1}
Ω	Angular velocity	rad s^{-1}

Acronyms

BEM	Blade Element Momentum
HAWT	Horizontal Axis Wind Turbine
RMS	Root Mean Square
VLM	Vortex Lattice Method

1 Introduction and motivation

With dwindling global reserves of fossil fuels and rising energy prices, energy security is an increasing concern for governments worldwide. In conjunction with this, growing concern over global warming means there is increasing pressure on governments to move to low carbon and renewable forms of energy production. European Union Directive 2009/28/EC (European Parliament and Council of the European Union, 2009) places legal obligations on member states to this end, which in the UK translates to 15% of energy production from renewable sources by 2020.

Offshore wind is seen as one of the UK's key renewable resources and is therefore likely to contribute a large proportion of the renewable energy required to meet the 2020 target and beyond. The current installed capacity is only 3.5 GW, but the UK government has forecast a total 16 GW installed capacity by 2020, with potential for this to be increased further to 39 GW by 2030 (Department of Energy & Climate Change, 2013). In order to achieve this it will be necessary to reduce the cost of installation and operation of wind farms.

In terms of capital cost, there is a trade-off between wake effects, cabling costs and other installation costs, whilst trying to maximise the energy density of the farm (The Crown Estate, 2012). Cabling represents around 20% of the installation costs of a turbine (Barthelmie et al., 1996; The Crown Estate, 2012), meaning that a denser packing is desirable. However, this is likely to increase the frequency and extent of wake impact on downstream rotors, which will have implications in terms of fatigue and associated maintenance costs. Therefore, it is important that the effects of wake impact are fully understood in order to facilitate correct decisions about the spacing of wind turbines.

With a view to encouraging and supporting research into wind energy in the United Kingdom, the SUPERGEN Wind Energy Technologies Consortium was established in 2006 as part of the Engineering and Physical Sciences Research Council (EPSRC) funded SUstainable PowER GENeration and supply (SUPERGEN) programme. The principle aim of the consortium is

'To undertake research to achieve an integrated, cost-effective, reliable & available offshore wind power station.'

The focus of this thesis was in part motivated by the requirements of Deliverable 2.2 (Rotor-wind field interaction) of Phase 2 of this consortium. The developed model has also been coupled with a structural beam model developed at the Rutherford Appleton Laboratory as part of Deliverable 4.4.3, although this work will not be discussed here.

The contribution of this thesis is the development and validation of a new analysis tool in the study of wake impact and corresponding observations regarding the implications of wake impact loading. The impact of an upstream rotor wake on a downstream rotor can be considered in terms of two separate effects: the deterministic once per revolution loading associated with interaction of the blade with the mean velocity deficit of the upstream rotor wake and the stochastic loading due to the increased turbulence in the wake. The effects of both components are investigated. In respect of the latter, a model of ambient turbulence and its effects is also investigated to give further insight into stochastic loading of the wind turbine prior to development of the wake turbulence model.

1.1 Governing equations

Prior to the development of any numerical model, the governing equations of the flow being investigated should be identified. The governing equations of fluid motion can be derived from the conservation of mass

$$\frac{\partial \rho}{\partial t} + \rho \left(\nabla \cdot \mathbf{Q} \right) = 0 \tag{1.1}$$

and conservation of momentum, the Navier-Stokes equation,

$$\rho \frac{D\mathbf{Q}}{Dt} = -\rho g - \nabla p + \nabla \mathbb{T} \tag{1.2}$$

where $D/Dt = \partial/\partial t + \mathbf{Q} \cdot \nabla$ is the total derivative, ρ is the density, $\mathbf{Q}$ is the total velocity, t is the time, g is gravitational acceleration, p is the pressure and $\mathbb{T}$ is the stress tensor.

1.1.1 Incompressible flow assumption

The conditions for incompressible flow can be determined from the Navier-Stokes and Continuity equations, assuming small harmonic motions, as $M \ll 1$ and $kM \ll 1$ where M is the Mach number and $k = \omega b/U$ is the characteristic reduced frequency of the unsteady motion, where ω is the angular frequency, U is the incident velocity and b is the half chord; preferred to the chord, c, for historical reasons.

In the case of wind turbines, which have high aspect ratio blades and low tip speeds, the characteristic reduced frequency, based on the rotation frequency, is of $O(10^{-1})$. Most common models operating today have a tip speed of less than 100 m s^{-1} (Vermeer et al., 2003), which in standard atmospheric conditions gives a Mach number of around $M = 0.29$. Therefore, compressibility can be neglected.

1.1.2 Conservation of mass

For incompressible flows Equation 1.1 becomes $\nabla \cdot \mathbf{Q} = 0$. As the Reynolds number, $Re = \rho U c/\mu$ where μ is the dynamic viscosity, of the flow around the blades is $O(10^6)$ the flow can also be assumed inviscid outside of the boundary layers and wakes, which implies the local flow around the blades is irrotational. Therefore, the velocity can be expressed as the gradient of the velocity potential, Φ, giving Laplace's equation,

$$\nabla^2 \Phi = 0. \tag{1.3}$$

This is the governing equation for potential flow.

1.1.3 Conservation of momentum

For incompressible flow the stress tensor becomes $\nabla \mathbb{T} = \mu \nabla^2 \mathbf{Q}$ where μ is the dynamic viscosity, which in inviscid flow can be neglected giving the Euler equation for the conservation of momentum.

$$\rho \frac{D\mathbf{Q}}{Dt} = \rho \left[\frac{\partial \mathbf{Q}}{\partial t} + (\mathbf{Q} \cdot \nabla)\, \mathbf{Q} \right] = -\rho g - \nabla p \tag{1.4}$$

As the local flow is also assumed irrotational this can be rewritten in terms of the velocity potential and integrated along a stream line to give the unsteady form of Bernoulli's equation,

$$\rho\frac{\partial\Phi}{\partial t} + \tfrac{1}{2}\rho\left(\nabla\Phi\cdot\nabla\Phi\right) + \rho g z + p = f(t). \tag{1.5}$$

where z is height and $f(t)$ is the integration constant and is a function of time only.

1.2 Axis system

The axis system adopted is a right handed coordinate system, as defined in Figure 1.1, with x in the free stream, U_∞, direction, defining the axis of rotation, z perpendicular to the Earth's surface and y chosen to complete the right handed system, i.e. positive to the left when looking from upstream. The corresponding turbulence velocities are u, w and v, respectively.

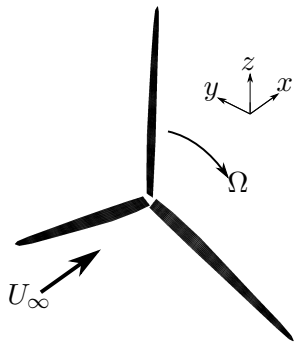
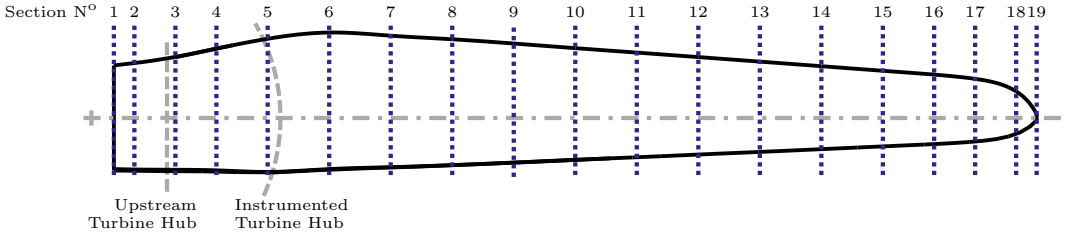


Figure 1.1: Axis system definition.

1.3 Turbine specification

The turbine used in both the numerical and experimental work described in this thesis was based on the Exemplar 5MW turbine designed by the SUPERGEN Wind Energy Consortium (Leithead and Watson, 2009). The Exemplar turbine is a three bladed upwind variable speed pitch regulated turbine designed for operation in offshore wind farms. It has a rotor diameter of 126 m, hub diameter of 3 m and hub height of 90 m. The cut-in wind speed is 4 m s^{-1}, with linearly increasing rotational velocity from 0.5 rad s^{-1} to rated wind speed of 11.5 m s^{-1}, above which it operates at a constant rotational velocity of 1.267 rad s^{-1}. The cut-out wind speed is 25 m s^{-1}. The full specification also includes coning and tilt of the rotor, although this has been neglected for simplicity.



Section N°	1	2	3	4	5	6
Radius, R (m)	0.00595	0.01138	0.02222	0.03307	0.04663	0.06290
Chord, c (m)	0.02778	0.02857	0.03059	0.03307	0.03617	0.03692
Pitch Axis (%c)	0.500	0.490	0.460	0.430	0.395	0.375
Twist, β (°)	13.308	13.308	13.308	13.308	13.000	11.600
Aerofoil Section	CIRCYLINDER	CIRTRAN172D	CIRTRAN105D	CIRTRAN071D	DU-00W2-401	DU-00W2-350

Section N°	7	8	9	0	11	12
Radius, R (m)	0.07917	0.09025	0.11171	0.12798	0.14425	0.16052
Chord, c (m)	0.03538	0.03372	0.03180	0.02975	0.02779	0.02584
Pitch Axis (%c)	0.375	0.375	0.375	0.375	0.375	0.375
Twist, β (°)	10.162	9.011	7.795	6.544	5.361	4.188
Aerofoil Section	DU-00W2-350		DU-91W2-250		DU-93-W-210	

Section N°	13	14	15	16	17	18	19
Radius, R (m)	0.17679	0.19306	0.20933	0.22288	0.23373	0.24458	0.25000
Chord, c (m)	0.02389	0.02194	0.01998	0.01836	0.01656	0.01126	0.00159
Pitch Axis (%c)	0.375	0.375	0.375	0.375	0.375	0.375	0.375
Twist, β (°)	3.200	2.319	1.526	0.863	0.400	0.106	0.000
Aerofoil Section				NACA-643618			

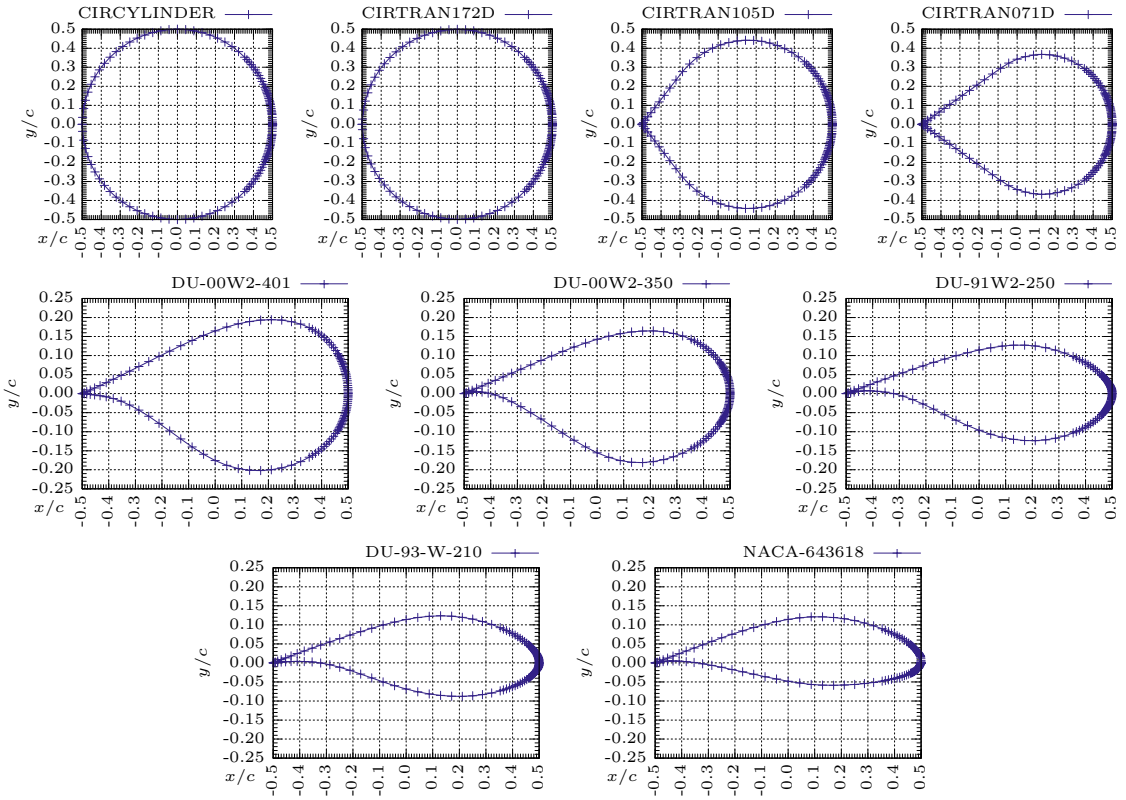


Table 1.1: Experimental turbine blade specification: Profile, sectional properties & aerofoil cross-sections.

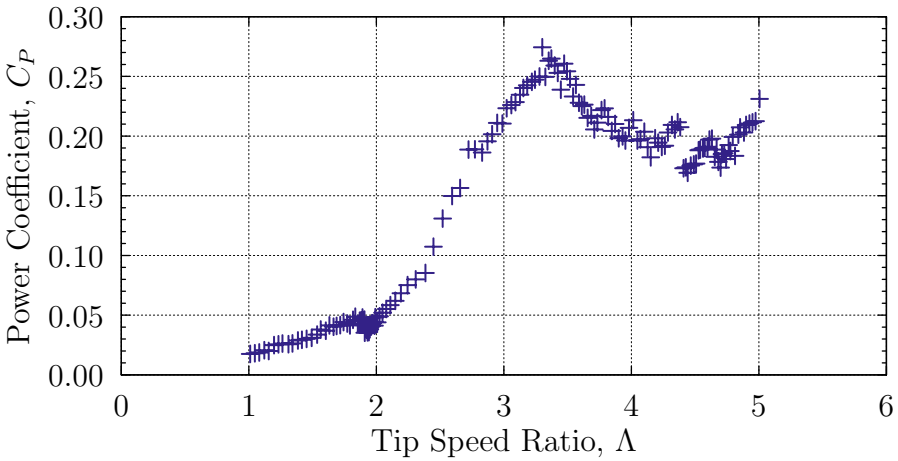


Figure 1.2: Indicative performance curve for the modified Exemplar turbine used in the experiments.

The experimental model was scaled to 1 : 250, and as such the scaled chord was increased by a factor of 2 to improve the structural strength, with the added benefit of marginally improved Reynolds scaling at the expense of double the solidity of the full scale. The blade specification is given in Table 1.1 in the form of tabulated sectional characteristics and plots of the cross-section aerofoil profile thickness normalised by the chord, y/c. When operating in the upstream rotor wake the maximum tip speed ratio, due to stall of the turbine, is reduced due to the mean velocity deficit. This was observed in preliminary tests and is in agreement with the observations of Adaramola and Krogstad (2011). Therefore the blade pitch was adjusted from 3.84°, as prescribed by the Exemplar control curve (Leithead and Watson, 2009) for 12 m s^{-1} flow, to 3.5° allowing operation over the range of interest.

Figure 1.2 shows the measured performance curve for the modified turbine. It should be noted that the values presented are only indicative due to some uncertainty in the calibration factor, but the curve serves to illustrate the stall region, below a tip speed ratio of 2, and peak power, at a tip speed ratio of around 3.5.

Unless otherwise stated, all results presented in this thesis, both experimental and numerical, correspond to the aforementioned turbine.

1.4 Turbine parameters

Several non-dimensional parameters fundamental to the aerodynamics of wind turbines have been defined. Of these, perhaps the most important is the tip speed ratio, Λ, which governs the scaling of loads on the wind turbine. The tip speed ratio is defined as

$$\Lambda = \frac{\Omega R}{U_\infty} \tag{1.6}$$

where Ω is the angular velocity of the turbine, R is the blade radius and U_∞ is the free stream velocity.

For comparison between different load cases, it is normal practice to represent the loads in terms of non-dimensional coefficients integrated over the rotor plane. The corresponding coefficients for the axial thrust, T, and power, P, are:

$$C_T = \frac{T}{\frac{1}{2}\rho U_\infty^2 \pi R^2} \tag{1.7}$$

$$C_P = \frac{P}{\frac{1}{2}\rho U_\infty^3 \pi R^2} \tag{1.8}$$

The out-of-plane blade root bending moment, M_b, coefficient is defined as

$$C_{M_b} = \frac{M_b}{\frac{1}{2}\rho U_\infty^2 \pi R^3} \tag{1.9}$$

Taken about the connection of the blade to the rotor hub with the rotation plane defined as the plane perpendicular to the rotation axis.

1.5 Computational methods

The simplest numerical model of wind turbine aerodynamics is the Actuator Disc Theory; first proposed by Rankine in 1865 with application to propellers and formalised by Froude (1889). The wind turbine is modelled as an actuator disc, which extracts energy from 1D flow, assumed uniform over the disc. By considering the rate of change of momentum due to the pressure difference across the disc it is possible to derive expressions of the axial thrust

$$C_T = 4a(1-a)$$

and extracted power

$$C_P = 4a(1-a)^2$$

where $a = 1 - U_{AD}/U_\infty$ is the axial induction factor and U_{AD} is the velocity at the disc. Maximising the latter equation gives $C_P|_{max} = 16/27$ for $a = 1/3$, known as the Lanchester-Betz limit. This can be physically interpreted as the limitation of energy extracted from the flow due to the need to have flow through the turbine in order to generate power. Whilst the actuator disc theory provides some useful insight into the aerodynamics of wind turbines, its applicability to more complex flows when used in isolation is somewhat limited. However, as will be seen, this and similar approaches have been used to simplify the modelling of wind turbines in the application of Navier-Stokes solvers, e.g. for macro-scale flow through wind turbine arrays.

The Blade Element Momentum (BEM) method, first proposed by Glauert in 1935, calculates the induction factors along the blade using the equivalence between the sectional loading and change of momentum in annular rings of the wake. The loading on the turbine is calculated from the sectional properties accounting for the induction, often requiring iteration of the solution. Combined with engineering models of 3D and unsteady flow effects, BEM is the current standard for rotor design codes (Vermeer et al., 2003). One of the fundamental assumptions of BEM theory is that the spanwise gradient of loading is small, such that each of the rotor annuli can be treated as independent. This implies that 3D effects, such as tip loss, must be corrected for and wake expansion is neglected. However, the main limitations of BEM theory are the assumption of steady flow for the momentum balance and axisymmetric flow such that the solution is independent of azimuth. Whilst BEM theory is able to accurately predict the performance of wind turbines under steady flow conditions, given sufficiently accurate aerofoil data, the necessity of corrections for modelling of 3D and unsteady flow effects makes it unsuitable for the investigation of either ambient turbulence or wake impact.

At the other end of the scale, the Navier-Stokes equations can be solved directly using a finite element or finite volume approach. However, direct numerical simulation

(DNS) is very computationally expensive due to the need to have highly refined discretisation in the regions of interest in order to resolve very small scale structures, such as the boundary layers around lifting surfaces or the smallest scales of turbulent flow. As such, it is common practice to use simplified approaches such as Large Eddy Simulation (LES), which models the smallest scales of turbulence rather than resolving them directly, or Reynolds Averaged Navier-Stokes (RANS) equations, which model all scales of turbulence and solve for the mean velocity field. To further simplify the model and reduce computational expense, particularly when modelling the flow through a wind farm, these models are often coupled with actuator disc representations of the rotor so that the flow around the blades need not be modelled. Even so, these methods are still relatively computationally expensive, limiting their use until computational power can be further increased.

The vortex lattice method is an intermediate solution for modelling rotor aerodynamics, which is able to capture most of the required 3D and unsteady effects with significantly reduced computational expense. The vortex lattice method has been applied to many different problems involving unsteady flows: Rossow (1995) used it to model aircraft performance, Fiddes and Gaydon (1996) investigated the flow past Yacht sails and Dumitrescu and Frunzulică (2004) used it to study Helicopter wakes. Katz and Plotkin (2001) present a comprehensive description of the method and its application to unsteady flows. The vortex lattice method is a potential flow solution where the lifting surface of the rotor blades is discretised into a lattice of vortex ring elements. In the unsteady formulation, bound vorticity on the blade is shed at the end of each time step to form a wake behind the rotor consisting of vortex ring elements. The wake is propagated downstream according to a specified velocity. Existing models applied to horizontal axis wind turbines are either prescribed wake (Robison et al., 1995; Coton and Wang, 1999), where the geometry of the wake, and hence propagation velocity, is known *a-priori*, or free wake (Bareiß and Wagner, 1993; Simoes and Graham, 1992; Pesmajoglou and Graham, 2000), where the wake is propagated according to the local velocity. The latter has the added benefit of being more general as it explicitly models the shape of the wake for a given inflow, at the expense of increased computational effort associated with

calculating the velocity field. In practice, most free wake methods could more accurately be termed semi-free in the sense that, in order to deal with the increased computational expense, the far wake tends to be frozen, i.e. treated in a prescribed manner and propagated with the free stream velocity.

One of the main advantages of the vortex lattice method is the explicit modelling of the wake influence and its response to unsteady flow, known as dynamic inflow. Hansen and Butterfield (1993) identify dynamic inflow as one of the two main forms of unsteady flow in wind turbines, the other being dynamic stall which will not be covered here, but is reviewed by for example Leishman (2002). Dynamic inflow is the effect of the induced velocity due to vorticity in the wake and associated delay in the response of blade loads to unsteady flow. Several engineering type models have been developed over the years to correct the results of BEM theory to account for dynamic inflow, probably the most commonly used being the model of Pitt & Peters (Leishman, 2006). However, Sørensen and Madsen (2006) note that most models of dynamic inflow were developed with reference to helicopters, which are designed to operate at low induction factors as opposed to the relatively high values associated with wind turbines, and hence may not be applicable. Snel and Schepers (1992) discuss several engineering models of dynamic inflow applied to blade element momentum theory and compared with a free wake vortex model, including an implementation of the Pitt & Peters model. The authors found that dynamic inflow effects contribute to large load overshoots for pitching transients, and less so for coherent wind gusts, and as such are significant in terms of the unsteady loading of wind turbines. Therefore, it is important that these effects are included in the simulation of unsteady inflow. In conjunction with the more generalised approach, another advantage of the vortex lattice method with respect to dynamic inflow is that the wake influence can be evaluated directly by considering only the wake vorticity in the solution.

Several computational methods for simulation of wind turbine aerodynamics have been outlined in this section. The vortex lattice method is preferred for the investigations in this thesis due to its implicit modelling of key 3D and unsteady effects

and explicit modelling of the wake influence, at a reduced computational cost when compared with Navier-Stokes methods.

1.6 Aims and objectives

The aim of this project is to study the impact of horizontal axis wind turbine (HAWT) rotor wakes on downstream turbine rotors in large arrays of wind turbines. The wake of a wind turbine consists of two key features: the mean velocity deficit and added turbulence. Therefore, in order to model wake impact a model of turbulent inflow is also required. In order to investigate upstream rotor wake impact, several objectives have been defined:

1. Development of a free-wake vortex lattice method model of a horizontal axis wind turbine under conditions of ambient turbulence and wake impact;
2. Measurement of time histories of the turbine thrust and rotor blade root bending moments on an instrumented model turbine operating in ambient turbulence and the wake of a similar turbine;
3. Validation of the model against wind tunnel measurements.

Once these objectives have been completed the effects of ambient turbulence and wake impact on the rotor can be characterised using the developed model.

1.7 Thesis overview

In this chapter the general problem area and governing equations have been identified and the aims and objectives of this thesis defined.

In Chapter 2 a review of the pertinent literature is presented, including a discussion of current understanding of wind turbine rotor wakes and corresponding models, as well as an overview of atmospheric turbulence.

A description of the developed free-wake horizontal axis wind turbine model, named Aeolus after the Keeper of the Winds in Greek Mythology, is presented in Chapter 3. This includes a general overview of the model and load calculations, optimisation and verification against existing models. Modelling of the wind field, including ambient turbulence, is also discussed in this chapter.

Chapter 4 gives an overview of the experiments and presents the results and discussion of both hot-wire investigations of the upstream rotor wake profile and time histories of the blade root bending moment and turbine thrust.

Validation of the model against the wind tunnel measurements and further discussion of the effects of ambient turbulence and wake impact are presented in Chapter 5.The unsteady response of the rotor wake, dynamic inflow, and the fatigue implications of wake impact are discussed.

In the final chapter, Chapter 6, the conclusions of the research are presented along with suggestions for further work that would improve the developed model.

2 Horizontal axis wind turbine wakes: A review

Several reviews of wind turbine aerodynamics have been conducted over the years (e.g. Vries (1983), Hansen and Butterfield (1993) and Snel (1998, 2003)) and latterly have begun to focus more on wake aerodynamics and modelling (e.g. Vermeer et al. (2003) and Sanderse (2009)). The following is a review of horizontal axis wind turbine (HAWT) wakes as pertains to this thesis, i.e. wake characterisation and numerical modelling for the purpose of studying wake impacting on downstream turbines in large arrays. For information regarding the general aerodynamics of wind turbines the reader is referred to one of the aforementioned reviews.

The characteristics of HAWT wakes are discussed (Section 2.2), followed by a summary of some of the proposed models (Section 2.3). The literature pertaining to wake impacting is discussed in Section 2.4 and a brief discussion of fatigue loading is presented in Section 2.5. Prior to this, a brief overview of ambient turbulence and its effects on HAWT is presented.

It is noted that the nomenclature within this chapter is primarily consistent with the relevant references, rather than the convention adopted in the main body of the thesis, and has been clearly defined where necessary.

2.1 Atmospheric turbulence

The profile of the wind and in particular the nature of turbulence in the atmospheric boundary layer has been extensively studied over the last few decades due to their importance to civil structures and meteorology. An overview of engineering models and applications of atmospheric turbulence can be found in, for example, the work of Panofsky and Dutton published in 1984 or the CIRIA report of Deaves and Harris in 1978, both of which are widely cited in the literature. The following is a general overview of wind in the atmospheric boundary layer and relevant models of the turbulence spectrum.

Harris (1970) presents a thorough overview of 'The nature of the wind' including approaches to model the mean and fluctuating components of the wind velocities. Based upon measurements by Van der Hoven (1957), Harris (1970) identifies an averaging period of approximately one hour as appropriate for separating out the effects of turbulence fluctuations, with time scales around one minute, and larger synoptic and diurnal weather patterns, with times scales around four days and twenty four hours, respectively, giving stable averages for the mean wind velocity. The latter effects are caused by surface temperature variations, and the resulting changes in pressure, due to solar irradiation. The former effect, which is of relevance to this thesis, is caused by surface friction. In this way, the properties of the mean flow and turbulence can be treated separately.

Connell (1988) identifies two main factors which govern the characteristics of turbulence in the atmospheric boundary layer: energy generation by shearing of wind on the earth's surface or shear layers in the flow and thermal stratification, which defines the static stability. Burton et al. (2011) define the classes of stability as: *unstable*, where rising pockets of hot air cannot cool to the surrounding temperature and hence continue to rise, and vice versa for falling pockets of cold air; *stable*, where rising pockets cool below their surroundings and sink; and *neutral*, where pockets of air remain in equilibrium with its surroundings. They also note that neutral stability is the most important in terms of wind turbines as it corresponds to strong winds with high turbulence, whereas stable stability give high wind shear and unstable stability promote gusts.

Similarly, Rohatgi and Barbezier (1999) note, based upon the observations of wind shear under different stabilities of Hiester and Pennell (1981), that neutral stability is the better for the fatigue life of the rotor, but suggest that unstable conditions may be advantageous for power generation due to the generally higher wind speeds. Conversely, they identify stable stratification as the worst case due to a combination of high wind shear and low wind speeds. Barthelmie et al. (1996) indicate that offshore winds tend to be close to neutral.

Turbulent flow at a point can be characterised by: an integral length scale, of the

order of 150 m to 250 m in atmospheric flows for heights relevant to wind turbine design (Harris, 1970); turbulence intensity, the ratio of the RMS and mean velocities; and the mean velocity. However, Connell (1988) notes that the coherence, defined as

$$\gamma_{ij}^2(f) = \frac{S_{ij}^2(f)}{S_{ii}(f)S_{jj}(f)} \tag{2.1}$$

where f is frequency, S_{ii} and S_{jj} are the power spectral density functions and S_{ij} the cross spectral density function of two points x_i and x_j, is important in the application of turbulence to wind turbine loading as it defines the variation of turbulence over the rotor disc.

2.1.1 Turbulence models

In order to model turbulent inflow, it is necessary to define the frequency spectrum of the fluctuating velocities. von Kármán (1948) proposed a model of the longitudinal spectrum of isotropic and homogeneous turbulence, given by Graham (1976) as

$$S_u(f) = \frac{4\sigma^2 L_x}{U}\left\{1 + 4\pi\frac{\Gamma^2\left(\frac{1}{3}\right)L_x^2 f^2}{\Gamma^2\left(\frac{5}{6}\right)U^2}\right\}^{-\frac{5}{6}} \tag{2.2}$$

where Γ is the gamma function, see e.g. Spiegel (1968), L_x is the integral length scale and σ and U are the RMS and mean velocities. von Kármán (1948) compared his model with measurements behind a regular grid in a wind tunnel and found good agreement.

Burton et al. (2011) note that whilst the von Kármán spectrum gives a good fit to wind tunnel turbulence, the Kaimal et al. (1972) model may be a better description of atmospheric turbulence. Although, it is also noted that the former is still the more commonly used. Kaimal et al. (1972) developed empirical expressions of the wind spectra based on a comprehensive set of data from flow over a flat, uniform site in Kansas, USA. For neutral stability, the spectra of the turbulence velocity components are:

$$S_u(f) = \frac{105u^{*2}z}{U}\left\{1 + 33\frac{zf}{U}\right\}^{-\frac{5}{3}} \tag{2.3a}$$

$$S_v(f) = \frac{17u^{*2}z}{U}\left\{1 + 9.5\frac{zf}{U}\right\}^{-\frac{5}{3}} \tag{2.3b}$$

$$S_w(f) = \frac{2u^{*2}z}{U}\left\{1 + 5.3\left(\frac{zf}{U}\right)^{\frac{5}{3}}\right\}^{-1} \tag{2.3c}$$

where z is the vertical coordinate and u^* is the friction velocity.

Harris (1970) proposed a spectrum identical in form to that proposed by von Kármán (1948) and derived the corresponding coherence of the longitudinal component as:

$$\gamma_{ij}^2 = \left(\frac{2}{\Gamma\left(\frac{5}{6}\right)}\left\{\left(\frac{\eta}{2}\right)^{\frac{5}{6}} K_{\frac{5}{6}}(\eta) - \left(\frac{\eta}{2}\right)^{\frac{11}{6}} K_{\frac{1}{6}}(\eta)\right\}\right)^2 \tag{2.4}$$

where K is the modified Bessel function of the second kind, see e.g. Spiegel (1968), and

$$\eta = \Delta r\sqrt{\left(\frac{\pi^{\frac{1}{2}}\Gamma\left(\frac{5}{6}\right)}{\Gamma\left(\frac{1}{3}\right)L_x}\right)^2 + \left(\frac{2\pi f}{U}\right)^2}$$

where $\Delta r = \sqrt{\Delta y^2 + \Delta z^2}$. In the case of the Kaimal spectrum, it is not possible to derive a simple analytical expression for the coherence and empirical models must be used (Burton et al., 2011), e.g.

$$\gamma_{ij}^2 = e^{-1.4\eta}.$$

Probably the most commonly adopted empirical relation for the coherence function was proposed by Davenport in 1961 (Kristensen and Jensen, 1979) as

$$\gamma_{ij}^2 = e^{-a\frac{f\Delta r_{ij}}{U}} \tag{2.5}$$

where a is a constant defining the rate of decay and Δr_{ij} is the distance between two points i and j. However, Kristensen and Jensen (1979) note that the value of C strongly depends on the static stability, and rather than being a constant is a function of the turbulence intensity and length scale. Consequently, the authors derive and propose a form of the coherence similar to that of Harris (1970) and compare this with measurements from the Sotra suspension bridge, Norway, finding reasonable agreement. Saranyasoontorn et al. (2004) compare the Davenport model, among others, with data from the Longterm Inflow and Structural Test (LIST) program and determine that it may not be able to accurately describe coherence at large separations or low frequencies. However, the von Kármán coherence is found to give more favourable agreement.

Schlez and Infield (1998) propose an alternative expression of the coherence for large separations,

$$\gamma_{ij}^2(\alpha) = e^{-\sigma \frac{\Delta r f}{U} \left(\left(\frac{a_1}{U} \cos\alpha \right)^2 + (a_2 \sin\alpha)^2 \right)^{\frac{1}{2}}} \tag{2.6}$$

where α is the orientation of the wind to the separation and a_1 and a_2 are empirical decay constants for longitudinal and lateral separations, respectively. A good fit with measurements at the Rutherford Appleton Laboratory test site, UK, was found for $a_1 = 30$ and $a_2 = 35$ s m^{-1}.

Solari (1987) presents a review of common models of turbulence and proposes an alternative spectrum, which has similar form to the previous two but with a random parameter, $\beta = \beta_m + \mu_\beta \Delta\beta$, in place of the usual length scale,

$$S(f) = \frac{2.21 u_*^2 \beta^{2.5} \frac{z}{U}}{\left(1 + 3.31 \left(f \beta^{1.5} \frac{z}{U}\right)\right)^{\frac{5}{3}}} \tag{2.7}$$

where μ_β is a uniformly distributed random variable in the range $[-1, 1]$ and the coefficients of β are defined by

$$\beta_m = \begin{cases} 7.5 & z_0 \leq 0.03 \\ 4.5 - 0.856 \ln(z_0) & 0.03 \leq z_0 \leq 1.0 \\ 4.5 & z_0 \geq 1.0 \end{cases}$$

$$\Delta\beta = \begin{cases} 2.5 & z_0 \leq 0.03 \\ 2.0 - 0.143 \ln(z_0) & 0.03 \leq z_0 \leq 1.0 \\ 2.0 & z_0 \geq 1.0 \end{cases}$$

where z_0 is the surface roughness height. This expression incorporates the various models discussed in the review. However, Solari (1987) notes that the precision is reduced at low frequencies and models that explicitly include the length scale should be used when the low frequency response is important. Similarly, Solari (1987) also proposes a form of the exponential coherence function, Equation 2.5, replacing the velocity with an average of the two points and the coherence decrement with

$$C_{ij} = b \left(\frac{\Delta r_{ij}}{z_m} \right)^{0.25}$$

where z_m is the average height of the two points and $b = 12 + 5\mu_b$.

2.1.2 Summary

Riziotis and Voutsinas (2000) investigate loading of wind turbines in complex terrains and conclude that ambient turbulence is a significant factor in terms of fatigue loads, in particular the turbulence intensity is the key parameter. Lubitz (2014) identifies that the impact of turbulence is governed by the corresponding frequencies: inertia of the wind turbine prevents it from responding to high frequency turbulence events. Further investigation of turbulence effects is generally considered in conjunction with wake measurements, e.g. Chu and Chiang (2014), and as such will be covered in the following sections.

Several models of the spectra and coherence of ambient turbulence in the atmospheric boundary layer have been discussed. As will be seen in Section 4.1.3, the von Kármán model gives good agreement with the experiments and hence is the preferred choice for the investigations in this thesis.

2.2 Wake characteristics

The structure of horizontal axis wind turbine wakes has been investigated extensively over the last few decades. Both field and wind tunnel investigations have been undertaken, examples of which are summarised in Table 2.1, and several reviews (e.g. Ainslie (1988), Elliott (1991) & Vermeer et al. (2003)) written on the subject. The following discussion highlights some of the key findings.

Alfredsson and Dahlberg (1979) identified two regions in the wake: a region dominated by the tip vortex and a decay region; these are commonly referred to as the near and far wake, respectively. Transition between the two regions is found to occur between four rotor diameters ($4D$) downstream of the turbine (Pascheke and Hancock, 2008; Högström et al., 1988) and $5D$ beyond which the axial mean velocity profile is approximately Gaussian (Ainslie, 1988). Alfredsson and Dahlberg (1979) also investigated the effect of increased ambient turbulence on wake development, identifying that the distance to transition between the wake regions is reduced to

Author(s)	Type	Method	Rotor Characteristics
Alfredsson and Dahlberg (1979)	Wind tunnel	Hot-wire Anemometry	2-Bladed & $D = 0.25$ m
Högström et al. (1988)	Field	SODAR[1], Tala Kites & Meteorological Mast	2 MW 2-Bladed, $D = 75$ m & $H = 77$ m
Grant et al. (1991, 2000)	Wind tunnel	PIV[2]	2, 3 & 6-Bladed, $D = 0.9$ m
Elliott and Barnard (1990)	Field	Meteorological Mast	2.5 MW 2-Bladed, $D = 91$ m & $H = 61$ m
Infield et al. (1993, 1994)	Field	PIV[2]	Stall regulated, $D = 17$ m & $H = 15.5$ m
Ebert and Wood (1997, 1999, 2001)	Wind tunnel	Hot-wire Anemometry	2-Bladed, $D = 0.25$ m
Vermeer (2001)	Wind tunnel	Hot-wire Anemometry & Flow Visualisation	2-Bladed, $D = 1.2$ m & $H = 2.33$ m
Barthelmie et al. (2004, 2006, 2010)	Field	Meteorological Mast, SODAR[1] & SCADA[3]	Various
Maeda et al. (2004)	Wind tunnel	LDV[4]	200 W & $D = 0.6$ m
Aubrun et al. (2007)	Wind tunnel	Hot-wire Anemometry	Porous disks, $D = 0.1$, 0.2 & 0.3 m
Pascheke and Hancock (2008)	Wind tunnel	LDA[4]	1:300 scale 5 MW, $D = 0.42$ m
Yang et al. (2011)	Wind tunnel	PIV[2] & Force Balance	1:350 scale, $D = 0.254$ m & $H = 0.225$ m

[1] SOnic Detection And Ranging; [2] Particle Image Velocimetry; [3] Supervisory Control And Data Acquisition; [4] Laser Doppler Velocimetry/Anemometry.

Table 2.1: Examples of field and wind tunnel investigations of HAWT rotor wakes.

$2-3D$. On the contrary, Maeda et al. (2004) conclude that increased ambient turbulence has little effect, although the former would appear to be more reasonable due to the increased mixing that would result. Ebert and Wood (1997), in the first of a series of papers based on hot-wire measurements in a closed circuit wind tunnel, make several general observations about the near wake. In particular, they determine that the bound vorticity and velocity profile in the near wake are roughly radially constant, with an abrupt change between the wake and free stream. The implication of this observation is that the near wake structure may be dominated by the rotor loading.

The tip vortex is found to decay $2-3D$ downstream (Ainslie, 1988; Whale et al., 1996), with some coalescence of vortices between $1-1.5D$ observed by Whale et al. (2000) using Particle Image Velocimetry (PIV) in a water channel. Whale et al. (2000) also determine that the tip vortex pitch decreases and the vortex strength increases with tip speed ratio, in agreement with the observations of Ebert and Wood (1997). Yang et al. (2011) agree with the former, but find the opposite true for the latter, noting that the strength of the vortex is found to decay with downstream distance. This behaviour is also observed by Vermeer (2001) and Grant et al. (1991). Vermeer (2001) suggests that the vortex strength is proportional to the bound circulation on the blade, which agrees with the observations of Infield et al. (1993), who find that differences in the blade loading are linked with the strength of the tip vortex. In the second paper in their series, Ebert and Wood (1999) indicate that the tip vortex absorbs an increased amount of power with increased tip speed ratio, which would otherwise be output by the turbine. Finally, the tip vortex is identified as having a helical structure (Yang et al., 2011) with pitch, p, determined by Whale et al. (1996) as

$$p = 2\pi\frac{U}{\Omega R}$$

where U is the transport velocity of the tip vortex, similar to the equation proposed by Ebert and Wood (2001) in their final paper. Grant et al. (1991) observed that the tip vortex pitch remained constant with downstream distance.

Ainslie (1988) identified that the velocity deficit is governed by the thrust coefficient,

whilst the ambient turbulent intensity determines the rate at which it decays with downstream distance; this is corroborated by Elliott (1991), who determines that the profiles are symmetric about the centre line in the lateral plane, Högström et al. (1988) and Elliott and Barnard (1990), who indicate that the maximum mean velocity deficit is located at the wake centreline. Elliott and Barnard (1990) note that the highest mean velocity deficits are seen for low turbulence intensity and low wind speeds and vice versa: The effect of wind speed on the deficit is more pronounced at low turbulence intensity and similarly turbulence intensity level has a greater impact at low wind speeds. Alfredsson and Dahlberg (1979) determined that the centreline velocity deficit is a decreasing function of turbulence described by

$$\frac{U_\infty - U_w}{U_\infty} \sim \left(\frac{x}{D}\right)^k$$

where subscript w denotes the wake, $k = -1.23$ in uniform flow and $k = -1.1$ in all other cases. Högström et al. (1988) find an exponent of $k = -1.06$ and constant of proportionality of 1.02 gives good agreement with field data from $2 - 15D$, and give the wake radius in the same region as $R = 53\,(x/D)^{0.47}$.

Vermeer et al. (2003) indicate that the wake increases the turbulence intensity, which is a more persistent effect than the velocity deficit, but also decays downstream. Increased wake turbulence is also observed by Pascheke and Hancock (2008), Elliott (1991), Elliott and Barnard (1990), who identify a peak around the periphery of the wake due to the tip vortex, and Högström et al. (1988), who quantify the longitudinal component of the wake turbulence intensity, I_w, as

$$I_w = 0.35\left(\frac{x}{D}\right)^{-0.5}$$

between $2 - 10D$ downstream, similar to the proposed velocity deficit profile, and note that wake rotation leads to an asymmetry of the turbulence profile. The latter observation is supported by the significant swirl observed by Pascheke and Hancock (2008) up to $7D$. Vermeer et al. (2003) note that the wake turbulence is more isotropic than the ambient conditions and Ainslie (1988) gives the length scales as $O(D)$.

Based on the above observations, among others, several models have been proposed to model the wake behind a HAWT. Some of these models are discussed in the next section.

2.3 Wake modelling

González-Longatt et al. (2012) identify three principal factors in the choice of wake model:

1. Computational cost;
2. Required accuracy of prediction;
3. Available wind parameters.

The authors refer to Kiranoudis and Maroulis (1997) for the classification of wake models into explicit (empirically determined, self similar velocity profiles) and implicit (more elaborate models based on Navier-Stokes equations), but also cite Barthelmie et al. (2006) as concluding that there is little difference between the two in terms of accuracy. Alternatively, Thomsen and Madsen (2005) classify wake models according to their intended application: mean velocity deficit models for predicting power performance in large arrays and turbulence equivalent models for load prediction on downstream turbines. As the former tend to be of the explicit type and the latter implicit, the prior classification is adopted in the following discussion.

2.3.1 Explicit models

The model of Lissaman (1979) is often cited as the seminal work on individual wake modelling paving the way for the development of many explicit, or kinematic, wake models. The model assumes all turbines are identical and requires the position of each, along with the diameter, hub height and power coefficient. The wake is separated into the near wake, dominated by momentum and rotor generated turbulence, with velocity deficit, based on the work of Abramovich (1963) on coflowing jets,

given by

$$\frac{U_w}{U_\infty} = \begin{cases} (1-a) & ;\ 0 < r \leq r_c \\ (1-a) + a\left(1-\eta^{1.5}\right)^2 & ;\ r_c \leq r \leq R \end{cases} \tag{2.8a}$$

where a is the axial induction factor, r_c is the radius of the wake core and R is the wake radius as defined in Figure 2.1, and

$$\eta = \frac{r - r_c}{R - r_c},$$

and the far wake, dominated by ambient turbulence, with velocity deficit given by

$$\frac{U_w}{U_\infty} = 1 - \Delta U \left(1 - \left(\frac{r}{R}\right)^{1.5}\right)^2 \tag{2.8b}$$

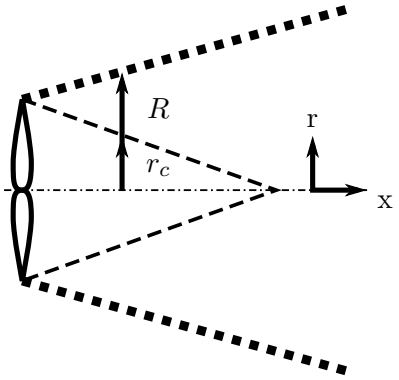


Figure 2.1: Wake geometry.

for $0 < r < R$, where ΔU is the normalised centreline velocity deficit. Assuming that the ambient and wake generated turbulence length scales are comparible, then the turbulent kinetic energy is the sum of the individual energies giving the wake growth as

$$\left(\frac{dR}{dx}\right)^2 = \sqrt{\left(\frac{dR}{dx}\right)_m^2 + \left(\frac{dR}{dx}\right)_a^2} \tag{2.8c}$$

where the ambient term is given by

$$\left(\frac{dR}{dx}\right)_a = \frac{\alpha}{0.5I}$$

with $\alpha = 0.05$ and the wake (momentum) term given by

$$\left(\frac{dR}{dx}\right)_m = 0.22\left[\frac{a-3}{a\Delta U}\right]^{-1}.$$

Whilst both terms are initially of the same order, the ambient term is quickly found to dominate. The effect of the ground on wake development is modelled using imaging and combination of the physical wake with the image wake assuming linear superposition conserving the momentum deficit and thus drag. A non-uniform inflow can be applied by assuming the same disturbance as in the uniform flow, and non-uniform turbulence by assuming growth governed by the respective components.

Tower shadow can be modelled using a drag producing cylinder with associated wake. Lissaman (1979) compared the model with limited field data available at the time and found the results to be promising, but indicated that further data was needed to make any conclusion. Notably, Högström et al. (1988) found good agreement with field measurements, obtaining the same profile of the velocity deficit in the far wake.

Katic et al. (1987) proposed a simple wake model for determining power losses across an array, which is found to give good agreement both with more detailed models and limited field data from the Nibe wind farm. The authors identify the key parameters as the direction and speed of the wind and the turbine and wake characteristics. The model assumes that the wake expands linearly with downstream distance, X, from the turbine diameter:

$$D_w = D + 2kX \tag{2.9a}$$

where k is the wake decay constant. The velocity deficit is asumed to have a 'top hat' profile with velocity:

$$1 - \frac{U_w}{U_\infty} = \left(1 - \sqrt{1 - C_T}\right) \left(\frac{D}{D_w}\right)^2. \tag{2.9b}$$

Where C_T is the thrust coefficient. Interaction between wakes is assumed to give a kinetic energy deficit equal to the sum of the individual wakes:

$$\left(1 - \frac{U_w}{U_\infty}\right)^2 = \left(1 - \frac{U_{w,1}}{U_\infty}\right)^2 + \left(1 - \frac{U_{w,2}}{U_\infty}\right)^2 \tag{2.9c}$$

which quickly approaches an equilibrium in agreement with experimental data. Ground effect is treated in the same way, using a mirror image of the wake about the ground plane. The wake decay constant is influenced by both ambient and wake turbulence as well as atmospheric stability. González-Longatt et al. (2012) propose a similar model with the wake decay constant inversely proportional to the logarithmic height profile, replacing the wake width with

$$D_w = D + \left(\ln(z/z_0)\right)^{-1} X)$$

where z_0 is the roughness height.

Ainslie (1988) assumes the wake is axisymmetric, fully turbulent with zero circumferential velocities and Gaussian in profile,

$$\frac{U_\infty - U_w}{U_\infty} = \delta e^{-3.56\left(\frac{r}{D_w}\right)^2} \tag{2.10}$$

which is valid from $2D$ downstream. From wind tunnel data, the initial velocity deficit is

$$\delta = C_T - 0.05 - \frac{(16C_T - 0.5)\, I_\infty}{10}$$

where I_∞ is the ambient turbulent intensity and the wake width, D_w, is given by conservation of momentum

$$D_w = \sqrt{\frac{3.56C_T}{8\delta\,(1 - 0.5\delta)}}.$$

This wake profile is then used as the initial condition for a 2D eddy viscosity model.

The Larsen et al. (1996) model is based on the Prandtl turbulent boundary layer equations. This gives the wake induced velocity as,

$$\frac{U_\infty - U_w}{U_\infty} = \frac{1}{9}\left(C_t A x^{-2}\right)^{\frac{1}{3}} \left\{ r^{\frac{3}{2}} \left(3c_1^2 C_T A x\right)^{-\frac{1}{2}} - \left(\frac{35}{2\pi}\right)^{\frac{3}{10}} \left(3c_1^2\right)^{-\frac{1}{5}} \right\}^2 \tag{2.11a}$$

and wake radius, R_w,

$$R_w = \left(\frac{35}{2\pi}\right)^{\frac{1}{5}} \left(3c_1^2\right)^{\frac{1}{5}} \left(C_T A x\right)^{\frac{1}{3}} \tag{2.11b}$$

Where A is the rotor area, c_1 is the non-dimensional mixing length,

$$c_1 = l\left(C_T A x\right)^{\frac{1}{3}}$$

and l is Prandtl's mixing length. The initial wake radius at the rotor plane is set equal to the rotor radius and a second empirical boundary condition, based on data from the Vindeby wind farm combined with the Lissaman (1979) model, prescribes the wake diameter at $9.5D$ downstream as

$$D_w = 1.08D + 21.7D\,(I_\infty - 0.05)$$

valid for ambient turbulent intensities of $0.05 \leq I_\infty \leq 0.15$. Agreement of the model with both a full Navier-Stokes simulation and single wake measurements from the

Vindeby wind farm is found to be satisfactory, with a slight tendency to under-predict the field data.

Frandsen et al. (2006) propose a wake model that encompasses the flow characteristics of large wind farms. This is further developed by Rathmann et al. (2006) based on a comparison with data from the Middegrunden and Horns Rev wind farms. For a single turbine, the wake is assumed axisymmetric with a 'top hat' profile, velocity deficit

$$\frac{U_w}{U_\infty} = \frac{1}{2}\left(1 + \sqrt{1 - 2\frac{A}{A_w}C_T}\right) \tag{2.12a}$$

and wake diameter, modified by Rathmann et al. (2006),

$$D_w(x) = D \max\left[\beta^{\frac{k}{2}}, \Gamma + \alpha\frac{x}{D}\right]^{\frac{1}{k}} \tag{2.12b}$$

where $k = 2$ and

$$\beta = \frac{1 + \sqrt{1 - C_T}}{2\sqrt{1 - C_T}}.$$

In the original model the decay factor was proposed as

$$\alpha = \beta^{\frac{k}{2}}\left[\left(1 + 0.1\frac{x}{D}\right)^k - 1\right]\frac{D}{x}$$

based on a comparison with the N.O. Jensen model and $\alpha = 0.7$ is found to give the best fit to the measured data. The parameter Γ is a dimensionless parameter which starts at zero for $x = 0$ and increments as the wake passes each turbine according the change in the streamtube area. The near wake model is found to compare well with the field data in terms of the wake velocity deficit and width. Once neighbouring rows have merged, Frandsen et al. (2006) proposed that the wake growth is simply vertically linear at a rate governed by the spacing, velocity deficit and thrust coefficient.

It is noted that, based on observations from the Alsvik wind farm, Magnusson (1996) propose that the pertinent parameter for wake development is the transport time as opposed to the distance travelled, although this approach has not been widely adopted. Assuming Taylor's frozen turbulence hypothesis this is given by

$$t(z) = \frac{x}{U_\infty(z)}.$$

In the near wake, the profile has twin peaks located at the blade midspan that reduce to a single peak due to momentum transport as the wake moves downstream. The time at which the single peak is formed, and transition to the far wake begins, is given by

$$t_0 = C_1 \frac{1}{f} \ln\left(\frac{H}{z_0}\right) \frac{R}{H} \tag{2.13}$$

where H is the hub height, f is the rotational frequency and $C_1 = 1$ gives a good fit to the field data. This assumes independence from C_T and increased effectiveness of momentum transport at increased hub height due to larger eddies. Comparison with a variety of data from both wind tunnel studies and field data give good agreement supporting these assumptions. For the far wake, Magnusson (1996) fits

$$\left(\frac{U_\infty - U_w}{U_\infty}\right)_w = C_2 \ln\left(\frac{t_0}{t}\right) + C_T \; ; t > t_0$$

where $C_2 = 0.4$. This implies $(U_\infty - U_w)/U_\infty = C_T$ at $t = t_0$. This expression compares well with available data, apart from where the averaging times are increased, which the author suggests can lead to an underestimate of the velocity deficit by up to 20% due to wake meandering.

2.3.2 Implicit models

Whilst the above models offer significant insight, and are generally found to be in good agreement with experimental data, more recent efforts have employed the Navier-Stokes solutions in an attempt to yield a more general and physically accurate approach.

Porté-Agel et al. (2011) propose that large eddy simulation (LES) offers the best compromise between the excessive complexity and computation cost of direct numerical simulation (DNS) and the limited applicability of Reynolds Averaged Navier-Stokes (RANS) due to the parameterisation of turbulence. The authors also compare several models for the wind turbine: the actuator disc approach with uniform loading across the rotor; a modified actuator disc approach that uses blade element momentum (BEM) theory to distribute loads across the rotor; the actuator line approach of Sørensen and Shen (2002). The authors find that the latter two perform better than

the first, indicating the importance of wake rotation and non-uniform loading across the rotor. Given these conclusions, it is somewhat unsurprising that the majority of implicit models use a combination of LES and the actuator line model (e.g. Lee et al. (2013), Machefaux et al. (2012) & Troldborg et al. (2010, 2011)), although alternatives do exist such as the actuator disc model of Thomsen and Madsen (2005) or RANS model of Seydel and Aliseda (2013). In general, these models are found to be in good agreement with experimental data, with discrepancies attributed to inflow conditions, yaw misalignment (Machefaux et al., 2012) or lack of a turbine nacelle model (Troldborg et al., 2010).

Sørensen and Shen (2002) developed the Actuator line model as an improvement over Actuator disc approaches used in earlier 3D Navier-Stokes solvers. The model applies radially distributed body forces, calculated using combination of BEM and aerofoil lookup tables, along lines corresponding to the rotor blades. The model is compared with field data from a Nordtank turbine and found to give good agreement up to the point where the rotor is stalled, after which the power is overestimated by around 5%, probably due to inaccuracies in the aerofoil data. The authors note that as there is no production of vorticity, except that which is diffused into the flow from along the blade lines, the rotor radius Reynolds number has limited effect on the results above a minimal value, defined as $Re_R = 5000$ by Sørensen et al. (1998) based on numerical simulations.

Troldborg et al. (2011) hypothesise, based on the comparison of the standard deviation with velocity deficit predicted by their LES model, that the largest turbulence energy content is at the highest deficit gradients, supporting the use of an eddy viscosity model in engineering approaches, as adopted in almost all of the models presented in this discussion. Troldborg et al. (2010) also note that the tangential velocities indicate that Helmholtz's theorem for conservation of circulation holds.

Madsen and Paulsen (1990) propose an integrated rotor and turbulent wake model based on actuator disc theory combined with the Euler equations and an eddy

viscosity model.

$$\frac{\partial U_x}{\partial x} = -\frac{\partial p}{\partial x} + f_x - \left(U_x \frac{\partial U_x}{\partial x} + U_y \frac{\partial U_x}{\partial y} \right) - \frac{\partial \overline{u_x u_y}}{\partial y}$$
$$\frac{\partial U_y}{\partial x} = -\frac{\partial p}{\partial y} + f_y - \left(U_x \frac{\partial U_y}{\partial x} + U_y \frac{\partial U_y}{\partial y} \right) \tag{2.14a}$$

where f_x and f_y are volume forces representing the rotor loading. This is combined with the continuity equation and turbulent stresses given by

$$-\overline{u_x u_y} = k R_w \left(U_{xmax} - U_{xmin} \right) \frac{\partial U_x}{\partial y} \tag{2.14b}$$

where R_w is the wake half width, $(U_{xmax} - U_{xmin})$ is the maximum velocity deficit and k is a constant. The key advantages of this model are indicated to be the calculation of performance at higher rotor loadings, indicating that the Betz limit (maximum $C_p = 0.593$ derived from momentum theory) does not hold, increased power coefficient due to turbulent stresses in agreement with measurements and analysis of turbine arrays with wake interactions. The model identifies the near wake region, with velocity deficit given by the rotor loading, which decays downstream with increased deficit at the centreline until the far wake Gaussian profile is recovered, similar to the observations of Troldborg et al. (2010). A comparison of the flap bending moment for both partial ($0.47R$) and full immersion in the wake of a turbine at $2.1D$ upstream show reasonably good agreement with measurements, although the model tends to slightly under-predict. However, the authors note that the measurements will include both yaw and once-per-revolution ($1P$) effects meaning they will give higher moments.

The ECN WAKEFARM model (Schepers, 2003) divides the turbine wake into a near wake inviscid expansion region and a far wake region modelled by a parabolised Navier-Stokes solution with $\kappa - \epsilon$ turbulence eddy viscosity model. The near wake extends up to $2.25D$ downstream with velocity deficit

$$\frac{U_w(x)}{U_\infty} = \frac{1}{2} \left(1 + \frac{x}{\sqrt{x^2 + R^2}} \right) \tag{2.15a}$$

with initial diameter equal to the rotor and expanded downstream diameter of

$$D_\infty = D \sqrt{\frac{1-a}{1-2a}} \tag{2.15b}$$

given by inviscid momentum theory expansion and neglecting turbulent mixing. At $2.25D$ the inviscid expansion is assumed complete and the near wake profile describes the initial condition for the far wake. As a first approximation, the near wake profile was assumed constant across the diameter of the wake with deficit

$$U_w = \frac{1}{2}\left(1 - \sqrt{1 - C_T}\right) U_\infty \tag{2.15c}$$

However, based upon the observations of the ENDOW project, this was later modified to a Gaussian profile,

$$U_w(z) = 1.3\left(1 - \sqrt{1 - C_T}\right) e^{-\frac{1}{2}\left(\frac{y}{r\sigma_y}\right)^2} e^{-\frac{1}{2}\left(\frac{z-h}{r\sigma_z}\right)^2} \tag{2.15d}$$

where $\sigma_y = \sigma_z = D_w/2D$ from wind tunnel experiments, which was found to give improved agreement with measured data.

The ECN WAKEFARM model assumes axial pressure, as well as streamwise diffusion, can be neglected to parabolise the governing equations, which is strictly only true in the far wake. As such, the empirical near wake model, described above, is required. Schepers and van der Pijl (2007) propose that an *a-priori* database of the streamwise pressure gradient, as a function of the axial induction, be used as an alternative to calculate wake expansion of a top hat velocity profile at the rotor corresponding to the given induction. Both models are compared with wind tunnel data giving similar results, but the latter is preferred as it demonstrates a more general validity.

Fletcher and Brown (2010) present a model based on the vorticity transport equation, derived from the Navier-Stokes equations in vorticity-velocity formulation and assuming incompressibility.

$$\frac{\partial \zeta}{\partial t} + \mathbf{U}\nabla\zeta - \zeta\nabla\mathbf{U} = S + \nu\nabla^2\zeta \tag{2.16}$$

where ζ is the vorticity, ν is the kinematic viscosity,

$$S = -\frac{d}{dt}\zeta_b + \mathbf{U}_b\nabla\zeta_b$$

and subscript b denotes the bound vorticity modelled using lifting line theory. The velocity field is then determined using the differential form of the Biot-Savart law

$$\nabla^2\mathbf{U} = -\nabla \times \zeta.$$

The Reynolds number is assumed high enough to solve the flow in its inviscid form. The authors suggest that the velocity deficit appears to be governed by the inviscid breakdown of the wake and hence viscous dissipation may have a minimal effect.

2.3.3 Comparison

Several of the models described were developed and/or improved upon as part of the ENDOW (Efficient Development of Offshore Wind Farms) project. These include:

1. Risø Engineering model, a collection of largely empirical sub models for the mean wake deficit, turbulence intensity and length scale and the coherence decay factor (partly based on work by Larsen et al. (1996));
2. Risø WAsP model (Katic et al., 1987);
3. Risø Analytical model (Frandsen et al., 2006);
4. University of Oldenburg (UO) FLaP model (based on Ainslie (1988));
5. ECN WAKEFARM model (Schepers, 2003).

Other models considered include: A fully elliptic turbulent Navier-Stokes model developed at the Robert Gordon University (RGU); An analytical model based on transport time using Taylor's hypothesis developed by the Meteorological Institute at Uppsala University (MIUU); Garrad Hassan's axis-symmetric CFD Navier-Stokes solver (WindFarmer).

In addition, Barthelmie et al. (2004) present an overview of wind farm databases also compiled as part of the ENDOW project: Bockstigen in the Baltic Sea, 5×500 kW Wind World stall regulated turbines with $D = 37.3$ m and $H = 41.5$ m; Horns Rev in the North Sea, 80×2 MW Vestas pitch regulated turbines with $D = 80$ m and $H = 67$ m; Middelgrunden, 2 km North of Copenhagen, 20×2 MW Bonus stall regulated turbines with $D = 76$ m and $H = 64$ m; Vindeby, 2 km from the coast of Denmark, 11×450 kW Bonus stall regulated turbines.

Rados et al. (2001) were the first to compare the proposed wake models, using data from the Vindeby and Bockstigen wind farms. Considerable variability was observed

between the different models. All over-predict the wake influence far downstream at Vindeby, although the turbulent intensities are well predicted, with the exception of the MIUU model. The ECN and RGU models predict both the velocity and turbulent intensity profiles reasonably well. However, along with the UO model, they over predict the turbulent intensity at Bockstigen, which is correctly predicted by the Risø and WindFarmer models.

Given the unexpectedly poor comparison, several improvements were made and the results reported by Barthelmie et al. (2004). The near wake, turbulence representation and wake superposition were improved in the various models, resulting in better agreement and reduced variability for the single wake case. Differences were greater at low turbulence levels, but the match at high turbulence was very good. The authors recommended development of wake meandering, as well as further improvement of wake superposition and the near wake representation. To that end, a series of wake measurements were undertaken at the Vindeby wind farm using a ship mounted SODAR (SOnic Detection And Ranging) system. A regression fit of the SODAR data for the hub height velocity with downstream distance gave

$$\frac{U_\infty - U_w}{U_\infty} = 1.07 \left(\frac{x}{D}\right)^{-1.11}$$

which agrees well with the observations of Alfredsson and Dahlberg (1979) and Högström et al. (1988).

Barthelmie et al. (2006) compare the SODAR measurements with the wake models. Significantly, the authors suggest that no particular model gives consistently better results, both in terms of the velocity and cumulative momentum deficit, with little difference in the accuracy between high and low turbulence cases. All the models compare poorly in the near wake, which is understandable as none were designed to operate in this region, but also tend to over-predict the velocity deficit in the far wake.

Following on from the ENDOW project, Barthelmie et al. (2010) compare the WaSP, WindFarmer and WAKEFARM models with NTUA's fully elliptic 3D turbulent RANS and data from the Horns Rev and Nysted wind farms. The Nysted wind

farm consists of 72 × 2.3 MW Siemens stall regulated wind turbines with $D = 82.4$ m and $h = 69$ m. The authors find that all models are capable of predicting the wake width, and the latter three the power deficit, with generally improved performance for higher wind speeds and axially aligned flow.

Vølund (1992) compared the explicit Katic et al. (1987) model and the implicit model of Madsen and Paulsen (1990) with field data from a 250 kW turbine operating in an upstream rotor wake. The author finds that both models sufficiently predict partial submersion, although the Madsen model does slightly better. Neither model is able to predict the $1P$ variation in the flap moment due to wind shear in the case of full submersion, although the Madsen model does accurately predict the mean deficit.

Duckworth and Barthelmie (2008) compare the explicit Katic et al. (1987), Ainslie (1988) and Larsen et al. (1996) wake models. The authors find the Ainslie model to be the most accurate in terms of the wake width and centreline deficit, whilst being strongly dependent on the value of C_T, when compared with field data from several wind farms. This parametrisation is not present in the other two models, although the Larsen model does account for the effects of turbulence intensity.

It is evident from the above comparison that whilst implicit models do offer some improvement, explicit models are equally capable of estimating the wake of an upstream turbine. Of the latter type, models utilising a Gaussian profile, such as Ainslie (1988), appear to perform the best, as identified by Vermeer et al. (2003).

2.3.4 Turbulence characteristics

In addition to the mean velocity deficit, the turbine wake adds a notable degree of turbulence into the flow, although this effect is more noticeable in low ambient turbulence than high (Stefanatos et al., 1996) due to increased mixing and subsequent wake recovery. In order to simulate wake turbulence explicitly, avoiding the large computation cost of the implicit models, engineering models based on empirical observations have been proposed by several authors.

Højstrup (1999) investigates the turbulence in wind turbine wakes using data from the Nørrekær Enge II wind farm. The author found that turbulence generated by wake shear has length scales in the order of the wake diameter, in agreement with Larsen et al. (1996) and significantly smaller than the ambient length scale, and is input at the higher end of the frequency spectrum, confirming the observations of Hassan et al. (1988). In the near wake, Højstrup (1999) found that the turbulence intensity is increased across the wake, with a slight peak in the tip region, and decreases monotonically towards the background levels ($11 - 13\%$) with increased downstream distance. Effects are still visible as far downstream as $14.5D$.

Crespo and Hernández (1996) proposed a model of the turbulence spectrum in the wake based on the assumption that the wake spectrum has the same formal dependence on frequency as the ambient flow with modified length and velocity scales, noting that both flows should be considered anisotropic. The added turbulence intensity in the wake is defined as

$$\Delta I = \sqrt{I^2 - I_\infty^2} = 1.026\frac{\sqrt{\Delta k}}{U_\infty} \tag{2.17a}$$

and the wake spectrum becomes

$$nS_u = 19\frac{f'k}{(1+33f')^{\frac{5}{3}}} \tag{2.17b}$$

where $f' = nz'/U_\infty$ and $z' = \left(2.5(k/5.47)^{3/2}\right)/\epsilon$, k is the turbulent kinetic energy and ϵ is the dissipation of k in the wake. In the near wake,

$$\Delta k = k - k_\infty = \frac{1}{2}\left(U_\infty - u\right)\left(U_\infty - u + \Delta U_z\right) \tag{2.17c}$$

where ΔU_z is the velocity deficit across the ambient shear boundary layer. The maximum value is $\Delta k_{\max} = \Delta U_0^2/8$ which gives

$$\Delta I_{max} = 0.725a = 0.362\left[1 - \sqrt{1 - C_T}\right].$$

In comparison with wind tunnel and field data, this is generally in good agreement up to around $4D$ where assumptions start to break down. Therefore, it was necessary to determine an alternative expression for the far wake, given as

$$\Delta I_{max} = 0.73a^{0.8325} I_\infty^{0.0325}\left(\frac{x}{D}\right)^{-0.32}$$

derived from a least squares fit of parabolised Navier-Stokes simulation results.

Larsen et al. (1996) also describe an engineering turbulence model applied to the whole wind farm.The authors presume that the turbulence within the farm is preserved from the first turbine, meaning it can be characterised by a turbulence intensity and length scale. The wake turbulence intensity is assumed a function of the turbine spacing, S, and the free stream velocity, given as

$$I_w = K\left(DS\right)^{-\frac{1}{3}}\sqrt{1-\sqrt{1-C_T}} \tag{2.18a}$$

valid for $S \geq 1$, where $K = 0.93$ calibrated against data from the Vindeby and Nørrekær Enge wind farms. Assuming a linear relation between thrust and mean wind speed gives the lengthscale as

$$L_w = L_\infty\left(1 - \frac{12.2\left(1-\frac{D}{L_\infty}\right)}{U_\infty S_r^{0.6}}\right) \tag{2.18b}$$

where L_∞ is the ambient lengthscale and the reduced spacing is defined as

$$S_r = 2^{0.8} + \left(S-2\right)^{0.8}$$

valid for $S \geq 2$. This model has the advantage of using a single equation for the entire length of the wake, which is found to give a satisfactory agreement with measurements from the Vindeby and Nørrekær Enge wind farms. Additionally, Duckworth and Barthelmie (2008) find that the model performs better than other models proposed in the literature, although all tend to over-predict the turbulence intensity.

Højstrup (1999) compare measured spectral coherence with a simple model,

$$\gamma(f) = \sqrt{\frac{-z_a S f}{U}}$$

where S is the spacing and $z_a = 12 + 22(z_2 - z_1)/(z_2 + z_1)$, and find reasonable agreement in both the lateral and vertical planes, although the coherence drops off much quicker at higher frequencies in the latter case. The author notes that in lower ambient turbulence, such as that found in the offshore environment, the coherence in the wake could decrease as the wake effects extend further downstream.

2.3.5 Superposition

Another consideration when modelling wind turbine wakes is the superposition of interacting wakes within an array. Rathmann et al. (2006) propose two alternative models for wake superposition: The mosaic tile wake combination model

$$\frac{1}{\rho U_\infty^2} \sum_{i=1}^{n} T_i = \sum_{k=1}^{n} \sum_{J^k} A_{J^k} \delta_{J^k} \left(1 - \delta_{J^k}\right) \tag{2.19}$$

where J^k denotes a tile associated with a subset of k wakes with area A_{J^k} and deficit δ_{J^k} and the semi-linear wake combination model based on superposition of individual wakes. Only the semi-linear model is implemented in the paper, but due to an overestimate of the velocity deficit in overlapping regions the authors propose development of the mosaic tile model. Similarly, Stefanatos et al. (1996) conclude that the linear superposition of wakes gives a poor description of the flow.

However, Stefanatos et al. (1996) also found that lateral interaction of wind turbine wakes was minimal, indicating that whilst the centreline velocity deficit was slightly reduced, the majority of the wake profile remained unchanged. Conversely, Barthelmie et al. (2010) found that lateral merging of the wakes increased the power deficit across the wake, but had little effect on the centreline peak. Even so, the authors also conclude that the downstream superposition of wakes has minimal impact and identify the power deficit as principally being determined by the nearest upstream turbine.

There appear to be conflicting observations of wake superposition, suggesting that further investigation is required in this area as identified early on by Ainslie (1988) and more recently by Barthelmie et al. (2004). However, the present thesis only deals with the single wake case and as such the discussion here has been brief.

2.3.6 Wake meandering

Wake meandering, the lateral oscillation of the downstream wake position, has been identified as one difference between field and wind tunnel data by Ainslie (1988) and as a key area of interest by Barthelmie et al. (2004) and Sanderse (2009). Barthelmie

et al. (2006) found that, in general, correcting model data for wake meandering improves the agreement with field measurements acquired using SODAR.

Corrections proposed by Ainslie (1988) and Högström et al. (1988), among others, and a more physical model developed by Larsen et al. (2007), exist in the literature. However, as this effect was not observed in the wind tunnel experiments carried out as part of this thesis, Section 4.2.3, it has been neglected from the modelling.

2.4 Wake impacting

It is well documented that the power generated by a turbine operating in the wake of an upstream rotor is significantly reduced. This behaviour has been observed in both numerical simulations (e.g. Fletcher and Brown (2010) & González-Longatt et al. (2012)) and field/wind tunnel experiments (e.g. McKay et al. (2013)), although Adaramola and Krogstad (2011) identify a shortage of sufficiently detailed experimental data for verification of numerical models for turbines operating under the influence of wake interference. Adaramola and Krogstad (2011) identify the velocity deficit as the principal reason for reduced C_T and C_P, decreasing with increased spacing due to wake recovery, which is corroborated by the vorticity transport simulations of Fletcher and Brown (2010). Adaramola and Krogstad (2011) also identify that the lowest C_P at the downstream turbine occurs for optimal operation of the upstream turbine.

McKay et al. (2013) observed that the greatest deficit, approximately 35% at $3D$ separation, occurs between the first and second turbine in a row, but is reduced to 30% thereafter. Interestingly the authors also observe that, under the direct influence of an upstream rotor wake, downstream rotors tend to yaw their position in order to capture higher winds as a result of lateral mixing.

Magnusson and Smedman (1999) found that the velocity deficit behind the downstream turbine is lower than expected due to higher turbulence mixing in the wake of the upstream turbine. Lee et al. (2013) indicate that, in general, the effect of wake generated turbulence was to increase the fatigue loads on the downstream tur-

bine. They also found that increased atmospheric turbulence increases the fatigue loading, also observed by Troldborg et al. (2011), but reduces the relative difference between the upstream and downstream turbines suggesting it may also mitigate the wake impact.

Seydel and Aliseda (2013) observe a load minimum, for laterally spaced turbines, coinciding with the blade passing through the upstream rotor wake. The streamwise spacing seems impractically small, $1D$, which the authors do not discuss although they do note that their observations may be specific to the given layout. However, Fletcher and Brown (2010) use a slightly more reasonable spacing of $2D$ and find similar results. In the latter study, a lateral offset of $1D$ was found to be sufficient in negating the wake influence. The authors note that the impact of the strong $1P$ variation as the blade passes through the wake will be an increased fatigue loading. Troldborg et al. (2011) investigate more realistic spacings, $3.3 - 6.6D$, and find for full wake operation the downstream turbine shows increased loading with increased turbulence, but for the laterally offset case the average loading is actually decreased, supported by the observations of Maeda et al. (2004), but with increased standard deviation. Vølund (1992) also observed an increase in standard deviation for lateral offsets and attributes this to the increased turbulence intensity and $1P$ variation with blade passing through the upstream rotor wake and notes that wake interaction excites the $1P$, $2P$ and $4P$ modes, with the latter attributed to structural dynamics.

It is clear from these observations that, in addition to the power deficit, one of the key effects of upstream rotor wake impacting is increased fatigue loading. As such, a brief discussion of wind turbine fatigue loading follows.

2.5 Fatigue

In their review of wake modelling methods, Crespo et al. (1999) indicate a shortfall in the literature pertaining to modelling of fatigue loads, but indicate clear experimental evidence for an increase in the equivalent loads due to submersion in a wake.

Whilst the authors find explicit type wake models to give reasonable results for the flow behind a turbine, assuming the correct tuning of parameters, they indicate that only full 3D approaches offered by implicit models are capable of modelling the turbulence accurately enough for fatigue estimation.

However, Thomsen and Sørensen (1999) compare a modified form of the Risø PARK wake model (Katic et al., 1987) assuming a Gaussian profile with field data from the Vindeby wind farm in terms of fatigue loads generated by the flapwise bending moment and find good agreement. The Gaussian profile allows the wind speed influence on fatigue loads to be modelled by a horizontal shear,

$$u(y) = \sqrt{2}e^{-\frac{1}{2}}\left(1 - \sqrt{(}1 - C_T)\right)\left(\frac{D}{D + 2kX}\right)^3 U_\infty \frac{2y}{D},$$

where X is the streamwise spacing and $k \approx 0.5I_u$. The fatigue loads are then given by a damage equivalent load range

$$R_{eq}^m = \sum_i \frac{M_i^m n_i}{n_e q}$$

where m is the Wöhler exponent, $M_i(n_i)$ is the rainflow counting result and n_{eq} is the equivalent number of load cycles. The authors found, in agreement with Frandsen (1996), that the increased turbulence intensity and reduced length scales in the wake were the most important factors in fatigue loading, which increased by $\approx 5\%$ for operation in an upstream rotor wake. Frandsen (1996) also indicate that the turbulence levels and equivalent fatigue widths for single, double and multiple wake cases are roughly the same and that at low wind speeds the structure of turbulence is dominated by wake generated turbulence, but at higher speeds the ambient turbulence dominates. As such, operation in an upstream rotor wake will have a higher impact in the former case.

The rainflow counting method was first proposed by Matsuishi and Endo in a paper presented to the Japanese Society of Mechanical Engineers in 1968. Dowling (1971) indicates that the rainflow method gives a much more accurate estimate of fatigue life for complicated time histories than other methods that have been proposed. Downing and Socie (1982) describe one basic algorithm as follows:

1. Reorder the time series to start and finish with the maximum peak or minimum valley;
2. Read each peak or valley into an array in turn;
3. Calculate the stress range between the current and previous point;
4. Compare the current range with the previous and if greater then count the previous range and remove its peak and valley from the array;
5. Otherwise continue to next point.

The end result will be a set of stress ranges with corresponding cycle numbers, which allows the fatigue life to be assessed using Miner's Rule (Ragan and Manuel, 2007).

Rychlik (1987) proposes an alternative, but equivalent, algorithm to the rainflow counting method for fatigue life called the 'Toplevel-Up Cycle' counting method. For each local maximum $y(t)$ of a stress time series $y(s)$ in the range $-T \leq s \leq T$, define two ranges bound by t^+ as the time of the next up-crossing of $y(t)$ and $t-$ the previous down-crossing, either taking the s-extremum value if no such crossing exists, and calculate the stress amplitude of each as

$$H^-(t) = y(t) - \min\left\{y(s); t^- < s < t\right\}$$
$$H^+(t) = y(t) - \min\left\{y(s); t < s < t^+\right\}.$$

The number of cycles are then counted according to:

1. For $H^+(t) \geq H^-(t)$ and $t^- > -T$ or $H^+(t) < H^-(t)$ and $t^+ < T$, one cycle is defined with an amplitude

$$H(t) = \min\left\{H^-(t), H^+(t)\right\}.$$

2. If $t^- = -T$ or $t^+ = T$ one half cycle is counted with the respective maxima $H^-(t)$ or $H^+(t)$.
3. All other cases count two half cycles with amplitudes $H^-(t)$ and $H^+(t)$.

This method has the advantage of being both stationary and time invariant, whereas the rainflow counting method is time invariant only, meaning the solution is independent of the start point.

Ragan and Manuel (2007) propose that Dirlik's method for estimating fatigue damage from power spectra offers an advantage over traditional time domain methods utilising rainflow counting, which require many simulations to realise the more important larger stress ranges. However, whilst the method performs well for tower bending loads, the periodic components of the blade loads lead to over estimation of both edge and flapwise bending fatigue damage.

Addressing the same limitation, Sutherland and Osgood (1992) propose, instead, to use the average frequency spectra of a real time series to generate synthetic time series for rainflow counting. Deterministic signals are removed by subtracting the azimuth averaged signal from the time series. Synthetic time series are then generated with 50% RMS in the average spectrum for 95% of the signal and large excursions of 110% in the remaining 5% of the signal. This approach gives good agreement with cycle counts from the real time series, even in the high stress tail, and is therefore proposed as an effective method of determining fatigue life.

Dahlberg et al. (1992) investigate the effect of an upstream rotor wake on the fatigue loads of wind turbines using data from the Alsvik wind farm. Three 180 kW Danwin turbines ($D = 23$ m) are located in a row, with a forth located such that it is 5, 7 and $9.5D$ downstream of each of the other turbines. Blade root bending moments, with dead weight moments subtracted, and power output are sampled at 31.25 Hz. For operation in undisturbed flow of 10 m s^{-1} and $I_u = 0.03$, the flap bending moment shows a clear $1P$ variation due to the wind shear and a lesser $4P$ peak due to tower excitation of a symmetric rotor mode. Partial shadowing by the wake of a turbine $5D$ upstream results in half the power production and a 30% reduction in the mean flap bending moment, but three fold increase in the standard deviation. The bending moment deficit is decreased with downstream distance and is lower when fully aligned with the upstream wake. The $1P$ peak is further excited, whilst the $4P$ peak is suppressed. Converting the load-time series to fatigue load spectra using the rainflow counting technique shows an increased stress range for operation in a wake, in agreement with Hassan et al. (1988), decreasing with distance downstream, although the effect is still clear even at $9.5D$.

Hassan et al. (1988) investigated the impact of turbine wakes on fatigue life using data from the Nibe wind turbines. They found that the load spectrum increased by a scale factor indicating that the increase is due to the increased turbulence intensity. Conversely, the authors found that the length scale had little effect.

2.6 Summary

The wake of a wind turbine can be characterised as a mean velocity deficit and increased turbulence intensity at length scales corresponding to the rotor diameter. The far wake velocity is found to be suitably approximated by a Gaussian profile and to decrease with downstream distance.

Both explicit and implicit wake models have been examined. The general consensus is that, whilst implicit models are more physically accurate and generally applicable, models of the explicit type are sufficient to capture the turbine wake.

The principal influence of upstream rotor wake impacting is identified as reduced power production and increased loading, which has been identified as a cause of increase fatigue loads and reduced rotor life. In order to quantify the latter, a model of the wake turbulence, as well as the mean profile, is required. However, whilst there has been some effort to quantify the thrust loading under wake impacting, the majority or research has focused on the former due to the inherent cost implications for energy production. With the move to offshore wind farms, the implications of thrust loading and associated fatigue failure of turbine blades will have a more significant financial impact. Therefore, an investigation of the influence of wake impact on rotor thrust loads is of increasing interest.

Both the longitudinal and lateral spacing of turbines will influence the effect of wake impact. A greater distance between turbines will allow increased mixing and greater recovery of the turbine wake before reaching the downstream turbine, thereby reducing the effect of wake impact. However, as has been previously noted, offshore wind farms will require a denser packing of turbines to reduce cost. As longitudinal spacings are reduced the impact of lateral spacing will increase: lateral spacing

offers the possibility of mitigating wake impact by offsetting the upstream rotor wake. However, whilst both approaches require further research, the former has been the focus of several projects, but the latter has been less widely investigated.

For these reasons the following work will focus on the lateral offset of the upstream turbine, fixing the downstream position at a representative length for offshore wind farms, and will principally investigate the thrust loading implications.

3 Aeolus: An unsteady vortex lattice method wake model

As discussed in Section 1.5, the Vortex Lattice Method (VLM) implicitly models both 3D and dynamic inflow effects thereby making it a suitable choice for investigation of the unsteady effects of ambient turbulence and wake impact on a horizontal axis wind turbine rotor.

The continuous vortex line singularity is one of a set of analytical solutions to the governing equation of potential flow in 3D: Equation 1.3 derived in Section 1.1.2:

$$\nabla^2 \Phi = 0,$$

where Φ is the velocity potential. This forms the basis of the vortex lattice method, which is a potential flow panel method using quadrilateral elements made up of straight line vortex filaments to define the circulation around a thin lifting surface.

The specifics of the developed unsteady implementation of the vortex lattice method, Aeolus, will be discussed in Sections 3.1 – 3.5, followed by a description of the load calculations in Section 3.6, and the approach to wind field simulation in Section 3.7. The sensitivity of the model to various input parameters is investigated in Section 3.8. Finally, in Section 3.9 the developed code is verified against analytical results for a flat plate and existing models for turbine load calculations.

3.1 Boundary conditions

The boundary conditions that apply to potential flow are the far-field boundary condition and the solid surface boundary condition.

The far-field boundary condition specifies that the disturbance to the flow is negligible in the far field and is implicitly satisfied by the vortex ring solution.

$$\lim_{r \to \infty} \nabla \Phi = 0, \tag{3.1}$$

where r is the radial distance from the surface.

The solid surface boundary condition can be determined in one of two ways: the Neumann type boundary condition specifies the value of the normal derivative of the velocity potential at the surface; the Dirichlet type boundary condition specifies value of the velocity potential internal to a closed surface. As the vortex lattice method is applied to a lifting surface representation of the body, an open surface, the Neumann type is used, specifying that the velocity normal to the surface is zero.

$$\nabla\Phi.\mathbf{n} = 0, \tag{3.2}$$

where $\mathbf{n}$ is the solid surface normal vector. In order to satisfy this condition all of the local velocity components normal to the solid surface, including the induced velocities from each of the vortex ring singularities, must be known.

3.2 The Biot-Savart law

The induced velocity, V, at a point due to a vortex filament is given by the Biot-Savart law, expressed in scalar form as:

$$V = \frac{\Gamma}{4\pi}\int \frac{\sin\theta}{|r|^2}dl, \tag{3.3}$$

where Γ is the circulation of the vortex filament, r is the radial vector between the filament and calculation point, l is the length along the vortex filament and θ is the angle between the vortex filament and r.

Substituting

$$r = \frac{r_\perp}{\cos\theta} \qquad \text{and} \qquad dl = \frac{r_\perp}{\cos^2\theta}d\theta$$

where $r_\perp$ is the perpendicular distance between the filament and calculation point and integrating along the length of the filament gives

$$\begin{aligned} V &= \frac{\Gamma}{4\pi r_\perp}\int_{\theta_1}^{\theta_2} \sin\theta d\theta \\ &= \frac{\Gamma}{4\pi r_\perp}\big[\cos\theta_1 - \cos\theta_2\big], \end{aligned} \tag{3.4}$$

where θ_n are the angles between the vortex filament and the vector connecting the ends of the filament to the calculation point and subscripts 1 and 2 denote the start

and end of the filament, respectively. For the case of a filament of infinite length, $\theta_1 = 0$ and $\theta_2 = \pi$, resulting in the 2D form of the vortex velocity field.

$$V = \frac{\Gamma}{2\pi r_\perp} \tag{3.5}$$

Expressing Equation 3.4 in vector form using

$$r_\perp = \frac{|\mathbf{r}_1 \times \mathbf{r}_2|}{|\mathbf{r}_0|} \quad \text{and} \quad \cos\theta_i = \frac{\mathbf{r}_i \mathbf{r}_0}{|\mathbf{r}_i|\,|\mathbf{r}_0|}$$

and noting that the direction of the tangential velocity component is given by

$$\mathbf{n} = \frac{\mathbf{r}_1 \times \mathbf{r}_2}{|\mathbf{r}_1 \times \mathbf{r}_2|}$$

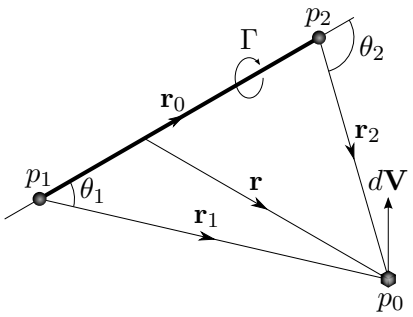


Figure 3.1: Biot-Savart law geometric definitions.

gives a generalised formula for the induced velocity of a finite length vortex filament.

$$\mathbf{V} = \frac{\Gamma}{4\pi} \frac{\mathbf{r}_1 \times \mathbf{r}_2}{|\mathbf{r}_1 \times \mathbf{r}_2|^2} \cdot \mathbf{r}_0 \left(\frac{\mathbf{r}_1}{|\mathbf{r}_1|} - \frac{\mathbf{r}_2}{|\mathbf{r}_2|} \right) \tag{3.6}$$

where the vectors $\mathbf{r}_n$ are defined in Figure 3.1.

3.3 Vortex core

Calculation of the induced velocity at any point along the line colinear with a vortex filament gives rise to either a singularity in, or indeterminacy of, Equation 3.6. Consequently, an excessively large velocity is induced at positions approaching a vortex filament. In particular, as two filaments pass close together the velocities they induce on each other lead to unrealistic convection, and eventual destabilisation, in the numerical solution due to the discrete nature of the time stepping procedure. As noted by Snel (1998), in physical terms, vorticity in the flow is not concentrated along lines of zero thickness. Also, in the VLM the vortex filaments represent the continuous vorticity on a sheet of zero thickness. Therefore, this problem is of a purely numerical nature. One solution is to add some numerical damping by assuming a concentrated vortex filament structure with a solid body core.

Vatistas et al. (1991) propose an empirical formula for the tangential velocity induced by an infinitely long concentrated vortex filament.

$$V = \frac{\Gamma}{2\pi} \frac{r_\perp}{(r_c^{2n} + r_\perp^{2n})^{\frac{1}{n}}} \tag{3.7}$$

where r_c is the core radius and the exponent n is used to describe a family of curves with the limits $n = 1$, corresponding to the Scully (1975) vortex model, and $n = \infty$, corresponding to the Rankine vortex model. The authors find that $n = 2$ gives the best fit to experimental data for integer values of n, although it should be noted that within the aforementioned limits n is a continuous parameter. This is further supported by the results of shadowgraph visualisations of a rotor tip vortex by Bagai and Leishman (1993).

Dumitrescu and Frunzulică (2004) use this model in their application of the vortex lattice method applied to helicopter rotors, but give no details of the implementation.

Equation 3.7 can be factorised as the product of the induced velocity of a 2D point vortex, Equation 3.5, and a radial basis function, $\xi(r_\perp)$, which passes through the origin and asymptotes to unity.

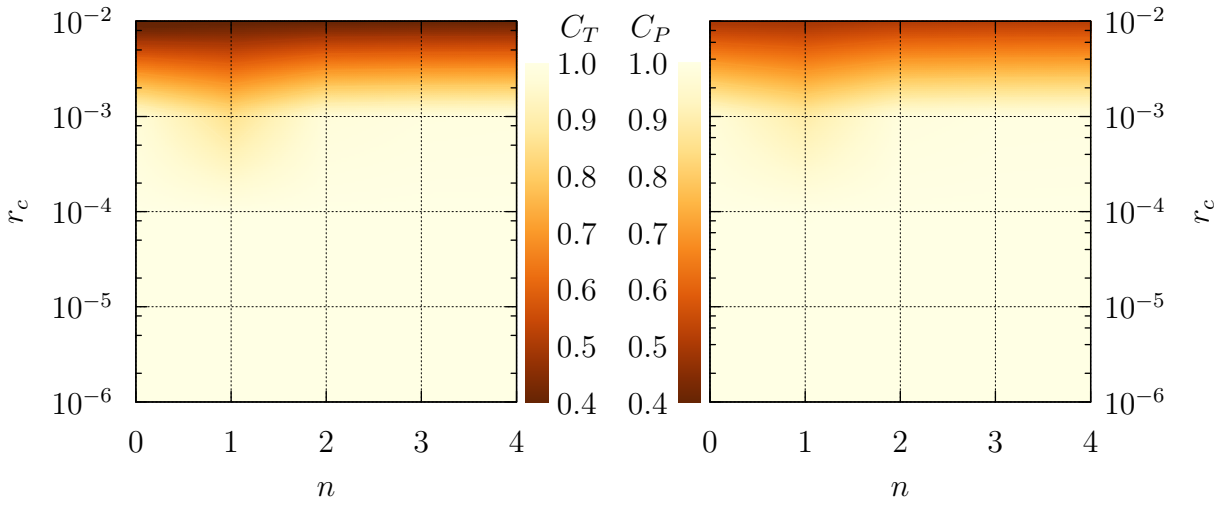
$$\xi(r_\perp) = \frac{r_\perp^2}{(r_c^{2n} + r_\perp^{2n})^{\frac{1}{n}}}$$

Applying this radial basis function to the equation for a finite length vortex filament, Equation 3.6, gives the generalised form of the induced velocity for a concentrated vortex filament.

$$V = \frac{\Gamma}{4\pi} \frac{\mathbf{r}_1 \times \mathbf{r}_2}{\left(\epsilon^{2n} + |\mathbf{r}_1 \times \mathbf{r}_2|^{2n}\right)^{\frac{1}{n}}} \cdot \mathbf{r}_0 \left(\frac{\mathbf{r}_1}{|\mathbf{r}_1|} - \frac{\mathbf{r}_2}{|\mathbf{r}_2|} \right) \tag{3.8}$$

where $\epsilon = \mathbf{r}_0 r_c$.

In order to investigate the influence of the proposed core model on the numerical solution, simulations of the rotor described in Section 1.3 with varying values of the core parameters were compared. Contours of the variation of the rotor load coefficients with the core parameters are shown in Figure 3.2, normalised by the values obtained without the core model. For $n = 0$ a simple cut-off core model, which prescribes $V = 0$ for $r < r_c$, was implemented, otherwise the values of n



(a) Thrust Coefficient, C_T

(b) Power Coefficient, C_P

Figure 3.2: Contours of variation in rotor coefficients with core parameters normalised by the equivalent coreless coefficients for $\Lambda = 3$.

correspond to the core model of Equation 3.8. The Scully (1975) vortex model results in the largest deficit in the rotor coefficients, with little difference between the higher values of n. The solution becomes highly sensitive to the core radius above $r_c = 10^{-3}$, dropping below 50% of the undamped value by $r_c = 10^{-2}$. This is caused by an overlap of the trailing edge wake filament vortex core with the collocation point on the trailing edge panels towards the tip. For $n = 2$ the coefficients correspond to the undamped value for $r_c = 10^{-4}$ and $r_c = 10^{-5}$ for the thrust and the power, respectively.

Several authors (e.g. Giannakidis and Graham (1996) & Dumitrescu and Frunzulică (2004)) have proposed the use of a growing core radius to model viscous dissipation. This approach is not adopted here as the intention is to remove the numerical instability rather than attempt to provide a physical model of the vortex core.

3.4 The vortex lattice method

The vortex lattice method solves for potential flow around a blade by satisfying the surface boundary condition, Equation 3.2, on a camber surface representation of

the blade using a network of vortex ring singularities; equivalent to the edges of a quadrilateral doublet source panel of constant strength $\mu = \Gamma$ (Lamb, 1945).

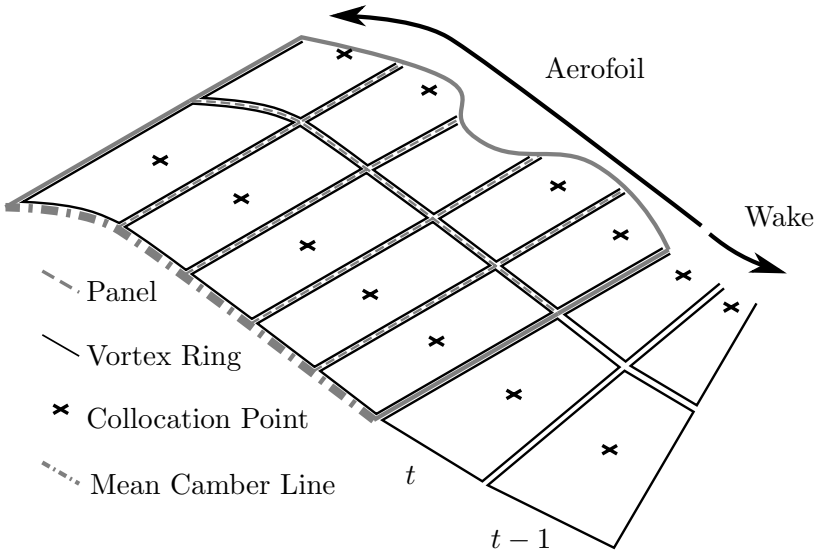


Figure 3.3: Vortex lattice method discretisation.

The lifting surface is first discretised into panels. A vortex ring element is then assigned to each panel and a collocation point is defined at the middle of each ring, shown schematically in Figure 3.3. Therefore, each panel intersection has two opposing vortex filaments with strengths corresponding to the adjacent panels. The panel normal n is defined at the collocation point as the cross product of the two vectors defined by the panel diagonals. The surface boundary condition in Equation 3.2 is applied at each of the collocation points.

$$\nabla\Phi_m.\mathbf{n}_m = \left[U_\infty + \Omega r_m + \sum_{blade} C_{mn}\Gamma_n + \sum_{wake} C_{mo}\Gamma_o\right].\mathbf{n}_m = 0$$

where U_∞ is the free stream velocity, Ω is the angular velocity and subscripts m denotes the current calculation panel and n and o denote the blade and wake panels, respectively. The influence coefficient, C, is given by either Equation 3.6 or 3.8 with unit circulation for the blade and wake, respectively. For a given position in time, the circulation strengths in the wake are known and hence the above equation can be rearranged to give a set of simultaneous equations allowing the circulation strengths

of the lifting surface vortex rings to be determined.

$$\begin{Bmatrix} \Gamma_1 \\ \vdots \\ \Gamma_m \end{Bmatrix} = \begin{bmatrix} C_{11} & \dots & C_{1n} \\ \vdots & \ddots & \vdots \\ C_{m1} & \dots & C_{mn} \end{bmatrix}^{-1} \begin{Bmatrix} Q_1 \\ \vdots \\ Q_n \end{Bmatrix} \tag{3.9}$$

where Q is the total velocity, a sum of the rotational, free stream and wake induced velocity components. The inversion of the coefficient matrix is performed using Gauss-Jordan elimination. The inverted matrix is stored and is only recalculated as necessary, e.g. when the blade deforms during aeroelastic coupling.

Several panel distributions were considered: cosine and half cosine distributions concentrate panels in the regions of higher loading gradients, namely the blade tip and root and the leading edge, and as such result in faster convergence of the results and greater resolution of the tip vortex, which significantly influences the aerodynamics of the blade. However, as the intention is to investigate uncorrelated stochastic inflow, an equispaced distribution is preferred so as to ensure the inflow features are adequately captured along the length of the blade.

3.5 Wake development

In order to calculate the wake induced velocities, the vorticity in the wake must be defined. This is achieved with a time stepping procedure.

Helmholtz's theorems (von Helmholtz, 1978) of vortex motion can be stated as:

1. An irrotational fluid remains irrotational;
2. A vortex filament is propagated according to the motion of the fluid;
3. The circulation is constant along the length of a vortex filament and conserved in time.

It follows that, as circulation is constant along the length it cannot suddenly reduce to zero, and hence a vortex filament cannot end in a fluid and must either form a closed loop or terminate at a solid boundary. For this reason the bound vorticity on the blade is shed at the end of each time step to form the wake.

The wake panel structure follows on from the blade panelling described in the previous section. At the beginning of each time step a new vortex filament is defined in the wake, coincident with the trailing filament of the bound vortex ring, simultaneously defining the trailing filament of the current wake panel and the leading filament of the previous wake panel. The wake panel is completed by connecting the leading and trailing filaments by straight line filaments and assigning the vortex strength of the shedding panel. In this way, each wake panel is equivalent to the space traversed in a time step by the trailing edge.

In accordance with Helmholtz's second theorem, the wake is propagated according to the local velocity field in the form of a force-free wake:

$$\Delta x = \mathbf{Q}\Delta t. \tag{3.10}$$

This involves the computationally expensive calculation of the self induced velocity of the wake at each time step, but affords a more generalised approach to prescribed wake methods which use empirical time histories of the incident velocity to convect the wake.

Given $n_y - 1$ spanwise panels and n_b blades, the number of wake panels after t time steps is given by $n_b\left(n_y - 1\right)t$. Equivalently, there are $n_b n_y\left(t + 1\right)$ nodes and $4n_b\left(n_y - 1\right)t$ filaments within the wake. Therefore, the total number of computations of the wake induced velocity per step is $4n_b^2 n_y t\left(n_y - 1\right)\left(t + 1\right)$, which, as t increases, increases with $O(t^2)$.

In order to reduce the expense of computing the self induced velocity of the wake, the far wake is frozen. After the wake has developed one complete rotation the self induced velocity term is dropped from the local velocities, meaning the wake is convected by the free stream alone. The maximum number of free wake nodes is reduced to $2\pi n_b n_y / \left(\Omega\ dt\right)$ reducing the computation to a linear dependence on t. As the number of revolutions of the rotor increases the relative computational time asymptotes to zero. At 5 revolutions, the computational time required is 30% of the unfrozen free wake and the increase in both the thrust and power coefficients is less than 1%, as shown in Figure 3.4 for $\Lambda = 3$.

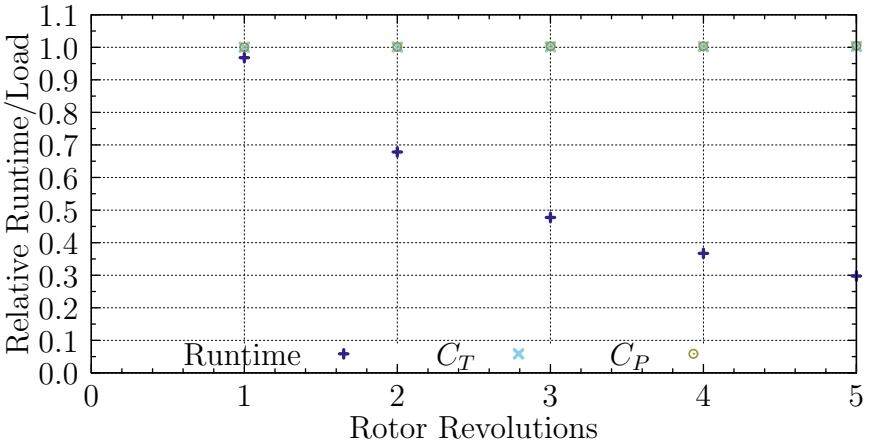


Figure 3.4: Comparison of runtime and loads for wake freezing after one complete rotation.

Kelvin's circulation theorem (Thomson, W. (Lord Kelvin), 1869) states:

> 'The circulation in any closed line moving with the fluid, remains constant through all time.' (p. 248)

Stated mathematically as:

$$\frac{D\Gamma}{Dt} = 0. \tag{3.11}$$

This is equivalent to Helmholtz's third theorem. The implication of these two theorems is that the circulation strengths of the shed vortex ring elements in the wake are kept constant.

The final condition that must be satisfied by the wake shedding procedure is the Kutta condition. Devinant et al. (1999) analytically derive the 3D unsteady Kutta condition for a thin lifting surface in potential flow as continuity of the potential jump and the gradient normal component across the trailing edge. For the case of a constant strength panel discretisation, the components contributing to the latter disappear leaving the classical condition as implemented by Katz and Plotkin (2001) among others. This is satisfied, in combination with the force free development of the wake and conservation of the wake ring strengths, by setting the shed wake vortex ring strength to that of the shedding bound vortex ring at each time step.

3.6 Aerodynamic loads

Once the bound circulation distribution has been defined, the loads on the lifting surface can be calculated in one of several ways.

The pressure loading on the blades is determined by taking the difference between the upper and lower surface of the unsteady form of Bernoulli's equation, e.g. see Katz and Plotkin (2001). Decomposing the tangential velocity into spanwise and chordwise components and noting that $\Delta\Phi = \Gamma$ gives

$$\Delta p_{ij} = \rho \left[\mathbf{U} \cdot \tau_i \frac{\Gamma_{i,j} - \Gamma_{i-1,j}}{\Delta c_{ij}} + \mathbf{U} \cdot \tau_j \frac{\Gamma_{i,j} - \Gamma_{i,j-1}}{\Delta b_{ij}} + \frac{\partial \Gamma}{\partial t} \right] \tag{3.12}$$

where τ is a line vector, i is the chordwise index, j is the spanwise index, c is the local panel chord and b is the local panel span. The unsteady derivative of Γ with respect to t is calculated using a backward difference. This approach is chosen as it is numerically stable and relies only on known values of Γ. The associated truncation error is of $O(dt)$, where dt is the time step increment.

The most common method of calculating the aerodynamic forces on the blade is to integrate the pressure loading over the surface.

$$\mathbf{F}_N = -\sum_{ij} \left(\Delta p_{ij} A_{ij} \right) . \mathbf{n}_{ij} \tag{3.13}$$

where A_{ij} is the panel area. Integrating over each of the blades and resolving into the axial and rotor plane directions gives the rotor thrust and power. However, due to the camber surface representation, and corresponding absence of a finite thickness leading edge to integrate over, the resolved forces neglect the component due to acceleration of the flow around the leading edge, known as the leading edge suction force, and are insufficient to accurately predict the in-plane force and hence the power of a turbine.

Katz and Plotkin (2001) correct for this in the limited case of a lifting surface in forward motion by assuming the in-plane force, in this case the induced drag, is the force parallel to the flow direction due to the induced downwash of the chordwise vortex filaments in combination with the fluid acceleration.

$$\Delta D_{ij} = \rho \left[\left(w_{ind} + w_W \right)_{ij} \Gamma_{ij} \Delta b_{ij} + \frac{\partial \Gamma_{ij}}{\partial t} \Delta A_{ij} \sin \alpha_{ij} \right] \tag{3.14}$$

where w is the induced downwash. This only applies to motion without side slip and only accounts for the drag due to chordwise vorticity. It can be extended to more complex wing motions assuming the direction of the in-plane force component can be identified.

The current implementation calculates the aerodynamic loads directly from the vortex filaments, circumventing the pressure distribution. The vortex ring is decomposed into straight line filaments and the contribution of each filament is calculated using the unsteady form of the Kutta-Joukowski theorem, as applied by Drela (1999) and Pesmajoglou and Graham (2000) among others. These are then combined to give the load on the vortex ring:

$$\mathbf{F}_i = \rho \Gamma_m \mathbf{Q}_i \times \mathbf{r}_0 \tag{3.15}$$

where $\mathbf{Q}_i$ is the total velocity at midpoint of the vortex filament and subscript i denotes the vortex filament and m the calculation panel. In addition to these loads the unsteady component is calculated for each panel as:

$$\mathbf{F}_m = \rho A_m \frac{\partial \Gamma_m}{\partial t} \mathbf{n}_m \tag{3.16}$$

These forces are then summed over the surface of the blade and resolved into the axial direction and rotor plane to give the torque and thrust. This has the advantage of taking into account the drag of every vorticity element and is able to incorporate more complex motions without modification. Simpson et al. (2013) compared this method with the correction proposed Katz & Plotkin and found that whilst both were able to accurate predict the drag with sufficient discretisation, the so called 'Joukowski' method converged significantly quicker.

3.7 Wind field simulation

In the present work, it is intended to model the effects of both ambient turbulence and upstream rotor wake impact, which includes added turbulence. To facilitate the implementation of these velocity fields, a Cartesian grid is superimposed over the simulation domain. The grid nodes are propagated according to the mean free

stream velocity at hub height. This implies an assumption of Taylor's frozen turbulence hypothesis (Taylor, 1938) for any velocity profile convected on the grid. These velocities are then linearly interpolated from the grid as necessary for computation of the local velocity for both the blade loading and wake propagation.

The unsteady loading on a turbine rotor due to the incident wind field is assumed to be dominated by the effect of length scales of the order of the rotor diameter, D, (Hansen and Butterfield, 1993). Similarly, Ainslie (1988) identified the dominant length scales of wake turbulence to be $O(D)$. Schlipf et al. (2010) have shown that Taylor's hypothesis holds for these length scales based on the coherence and phase lag of lidar (light radar) measurements.

Both ambient and wind turbine wake turbulence have been measured to be anisotropic: Crespo and Hernández (1996) give the standard deviations, σ, of turbulence as

$$\sigma_u = 2.4u^*;\ \sigma_v = 1.9u^*;\ \sigma_w = 1.25u^*$$

where u^* is the turbulent friction velocity. It is evident that of these the longitudinal component is the more dominant, but all three are of the same order. From Figure 3.5 the local inflow at a given blade section is

$$\phi = \arctan\left(\frac{U_\infty\left(1-a\right)+u}{\Omega r\left(1+a'\right)+f\left(v,w,\psi\right)}\right)$$

where a and a' are the axial and swirl induction factors, respectively, and $f\left(v,w,\psi\right) = v\cos\psi + w\sin\psi$ is a function of the azimuth, ψ. The incidence, α, of the section is the difference between the inflow angle and twist. The thrust is dominated by the lift coefficient, which is given by thin aerofoil theory as $C_L = 2\pi\sin\alpha$. Making the appropriate substitutions and rearranging gives an expression for the sectional lift in terms of the velocity components and blade twist:

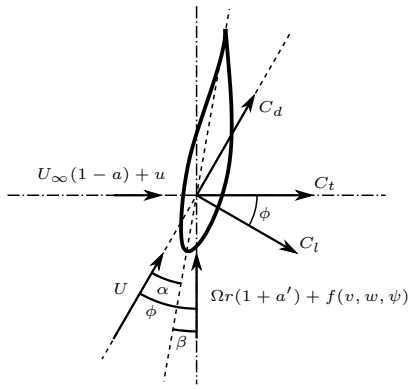


Figure 3.5: Section definitions.

$$C_L = 2\pi\left\{\frac{\left(U_\infty\left(1-a\right)+u\right)\cos\beta}{\sqrt{\left(U_\infty\left(1-a\right)+u\right)^2+\left(\Omega r\left(1+a'\right)+f\left(v,w,\psi\right)\right)^2}}\right.$$

$$- \frac{(\Omega r\,(1+a') + f\,(v,w,\psi))\sin\beta}{\sqrt{(U_\infty\,(1-a)+u)^2 + (\Omega r\,(1+a') + f\,(v,w,\psi))^2}} \Bigg\} \quad (3.17)$$

It is evident that for small angles of twist and large values of Ωr that the longitudinal component u is the most significant in terms of the variation of the inflow angle and corresponding lift, and hence the thrust loading on the rotor. Consequently, to simplify the numerical modelling only the longitudinal component will be considered.

Finally, distortion of the turbulence due to the presence of the rotor will also be neglected. In order to model this implicitly, a description of the free stream vorticity would be required, in place of the velocity components, with the associated computational cost of calculating velocity fields. An alternative may be to model this empirically by pre-adjusting the input spectrum, e.g. according to the model proposed by Graham (1976) for flow through a porous disc, although this has not been attempted in this thesis.

Veers (1984) proposed a method for generating a Gaussian wind series, $V(t)$, from a given discrete power spectral density (PSD), $S(f)$, by a Fourier series at n discrete frequencies, f_m,

$$W(t) = \overline{W} + \sum_{m=1}^{n} \left[A_m \sin 2\pi f_m t + B_m \cos 2\pi f_m t\right] \quad (3.18)$$

where $\overline{W}$ is the mean wind velocity and

$$A_m = \sqrt{\frac{1}{2} S_m \Delta f}\,\sin\phi_m \qquad ; \qquad B_m = \sqrt{\frac{1}{2} S_m \Delta f}\,\cos\phi_m$$

and S_m is the magnitude of the m^{th} component of the PSD, Δf is the discrete frequency spacing and ϕ is a uniformly distributed random variable in the range $[0, 2\pi]$ that imparts random phase. If the frequency spacing is uniform and the frequencies start from zero, the time series can be calculated using the inverse Fourier transform. As the number of discrete frequencies becomes large the velocity will approach a Gaussian distribution. Veers (1984) notes that if the turbulence components are uncorrelated each of them can be generated independently using this procedure.

Developing this method further, Veers (1984) generates a fully 3D spatially varying wind field from independently generated Gaussian time histories of N points within

a plane perpendicular to the free stream velocity assuming Taylor's frozen turbulence hypothesis. The spectral matrix,

$$S_{ij}(f) = \gamma_{ij}^2(f) S_{ii}(f) S_{jj}(f)$$

where i and j are the indices of, and γ_{ij}^2 is the coherence between, two points x_i and x_j, is decomposed into its lower triangular form.

$$\begin{aligned} H_{ii}(f) &= \left(S_{ii}(f) - \sum_{j=1}^{i-1} H_{ij}(f)^2 \right)^{\frac{1}{2}} \\ H_{ij}(f) &= \left(S_{ij}(f) - \sum_{k=1}^{j-1} H_{ik}(f) H_{jk}(f) \right) / H_{jj}(f) \quad \text{for } i < j \end{aligned} \tag{3.19a}$$

Combining the N signals into a diagonal matrix, $X(f)$, the fluctuating component, $W'(t)$, of the 3D wind field is then obtained as,

$$W'(t) = \mathcal{F}^{-1}\left(HX\right)[1] \tag{3.19b}$$

where [1] is a column vector of 1's, which acts to sum the rows of HX.

In a later paper, Veers (1988) refers to this method as the Sandia method and gives further details of the specific elements of Equation 3.19b. The j^{th} input of the matrix of independent input signals is generated at the m^{th} frequency component by,

$$X_{ij}(f) = \begin{cases} e^{\mathrm{i}\phi_{jm}} & i = j \\ 0 & i \neq j \end{cases} \tag{3.19c}$$

which has unit magnitude and random phase, ϕ, uniformly distributed in the range $[0, 2\pi]$. To maintain the correct variance, the discrete spectral matrix is derived from the one-sided PSD, $G_{ii}(f)$, using

$$S_{ii}(f) = \frac{G_{ii}(f)\Delta f}{2}. \tag{3.20}$$

Several options are presented for the one-sided spectrum, including the Kaimal et al. (1972) and von Kármán (1948) spectra, but the author prefers a spectrum derived by Solari (1987) for applications involving rotational sampling due to the use of random coefficients.

The main disadvantage of the Sandia method is the storage requirement (Veers, 1988), which for a time series of length T at N points within a plane requires more than $T\left(N^2+N\right)/2$ storage locations. In addition, Mann (1998) points to the computational expense $O\left(N_1 N_2^3 N_3^3\right)$ as a significant limitation and proposes an alternative method that only requires $O\left(N_1 N_2 N_3\right)$ computations and incorporates anisotropic turbulence and non-zero shear stresses.

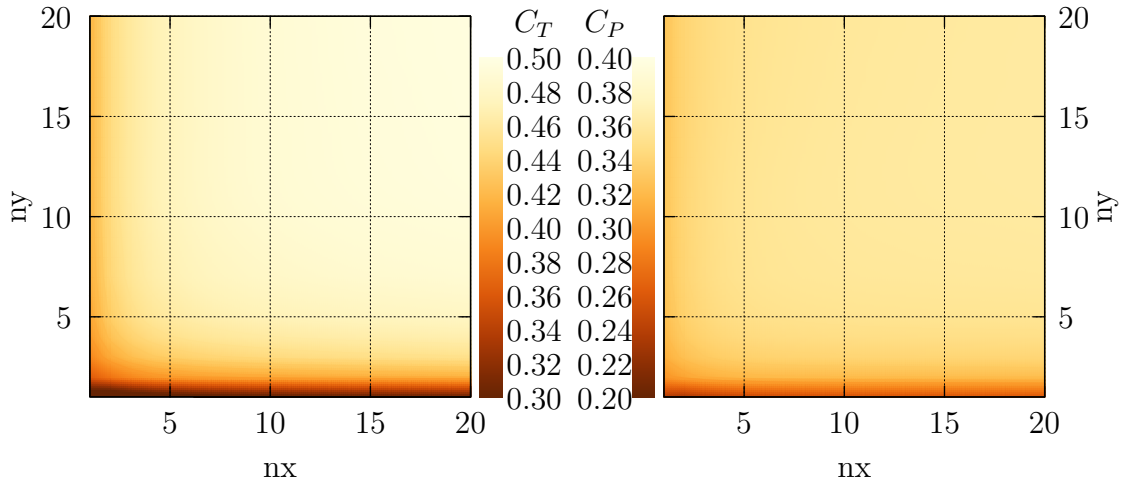
However, due to the assumptions made to simplify the derivation, and due to periodicity of the velocity field, the method proposed by Mann (1998) requires a large domain of $O(L_1 \gg L_x)$, which may be suitable for full CFD computations but is considered excessive for the methods employed in this thesis. Furthermore, given the relatively small grid used, the computational expense becomes negligible in comparison with the cost of the simulation. Therefore, the Sandia method will be adopted for the simulation of fully 3D wind fields.

3.8 Convergence studies

An investigation of the sensitivity of the solution to both panelling and time step parameters is presented. The purpose of such studies is to ensure that the solutions presented are not unduly influenced by the selection of input parameters, increasing the confidence in any conclusions that may be made. For the purposes of this thesis, the rotor described in Section 1.3 is used as the basis of the following studies.

3.8.1 Panel convergence

Contours of the variation of the rotor performance coefficients with the numbers of panels in the chordwise, n_x, and spanwise, n_y, directions are shown in Figure 3.6. Both coefficients behave in a similar manner: the coefficient is initially highly sensitive to and increasing with the number of spanwise panels. However, between around 3 and 7 panels the dependence shifts to the number of chordwise panels and above 10 panels the resulting value is fairly invariant to the spanwise distribution. The same limits apply to the chordwise dependence, meaning that for 9 panels in



(a) Thrust Coefficient, C_T (b) Power Coefficient, C_P

Figure 3.6: Contours of variation in rotor coefficients with panelling parameters for $\Lambda = 3$.

both directions the result can be seen to be relatively invariant to the increase in panelling.

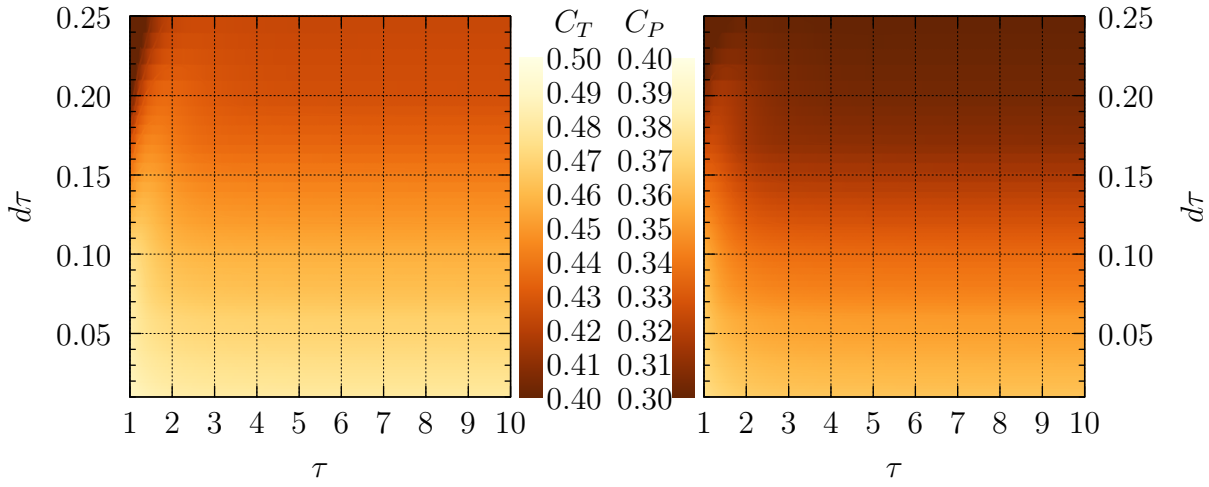
3.8.2 Time step convergence

The non-dimensional time parameter, τ, for a rotor is defined as:

$$\tau = \frac{\Omega t}{2\pi} \tag{3.21}$$

and can be interpreted as the number of rotor revolutions traversed by the rotor wake.

Contours of the rotor coefficients for increasing τ and $d\tau$, the equivalent parameter for a given time step, are shown in Figure 3.7. The initial value of the coefficients varies significantly with τ up to $3-4$ rotations. This is attributed to the transient response to an impulsive start. Conversely, the asymptotic value is governed by $d\tau$, as indicated by the relative invariance of the coefficients with τ above $5-6$ revolutions, and is increased with decreasing $d\tau$. These observations indicate that a minimum of $\tau = 5$ is required in order for the impulsive transient to decay and $d\tau$ should be minimised to give the best compromise between reasonable run time and increased accuracy, but not exceeding $d\tau = 0.10$.



(a) Thrust Coefficient, C_T

(b) Power Coefficient, C_P

Figure 3.7: Contours of variation in rotor coefficients with time stepping parameters for $\Lambda = 3$.

3.9 Verification

For the purpose of verification of the developed model, two test cases will be considered. The simplest case is that of a flat plate wing, for which there are several analytical solutions that can be used to verify both the steady and unsteady response of the VLM. The second case is that of a rotor which will be compared with Blade Element Momentum (BEM) theory .

3.9.1 Wing case

In order to verify the steady response of the flat plate wing, the variation in the lift curve slope with the inverse of the aspect ratio is compared to results obtained by Graham (1971), based upon the first approximation of a set of dual integral equations derived by applying a Fourier transform to the downwash equation, presented in Figure 3.8. The predictions from Aeolus are between $5 - 10\%$ higher, but the trend is matched accurately and agreement is generally considered acceptable.

Extension of the verification of the steady response to 3D is achieved via comparison of the settled coefficients for a flat plate wing of varying aspect ratio with results from

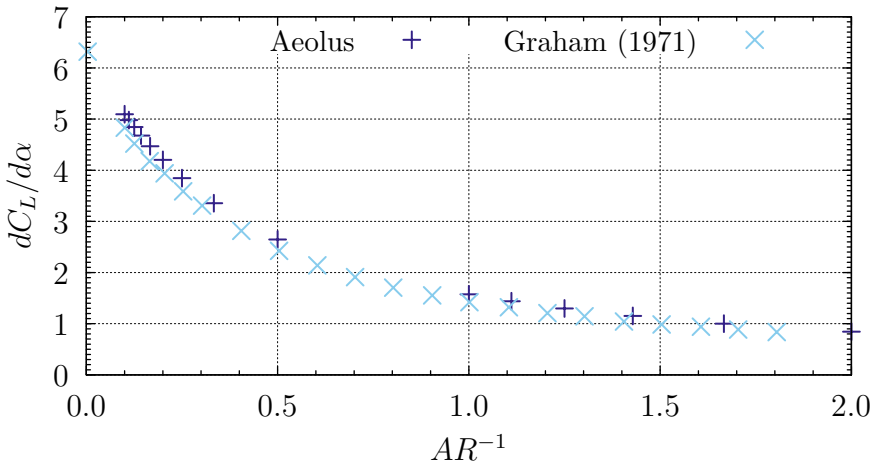
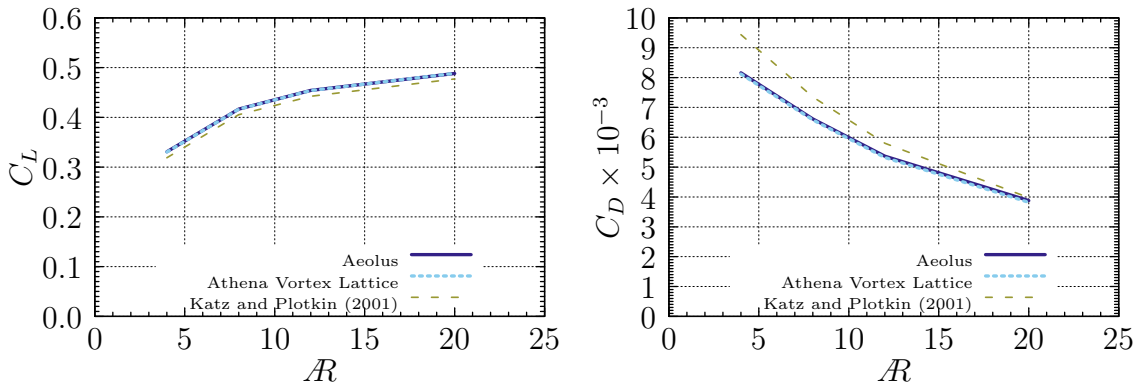


Figure 3.8: Comparison of steady lift curve slope with results of Graham (1971)

Katz and Plotkin (2001) and the Athena Vortex Lattice (AVL) code developed by Drela and Youngren (2014), shown in Figure 3.9. The AVL code is a quasi-steady implementation of the vortex lattice method using horseshoe vortices in place of vortex rings and the Kutta-Joukowski theorem to calculate the loads. All results are obtained for thirteen spanwise and four chordwise panels and incidence of five degrees. Katz and Plotkin (2001) predict marginally lower lift at all $\mathcal{R}$, within $2-4\%$, and significantly higher drag at low $\mathcal{R}$, 15% at $\mathcal{R}=4$ decreasing to 3% by $\mathcal{R}=20$. However, the agreement between Aeolus and AVL is excellent: in the limiting case the spanwise filaments cancel to give horseshoe vortices, and the unsteady forces in Equation 3.16 vanish, matching exactly the implementation in



(a) Lift Coefficient.

(b) Drag Coefficient.

Figure 3.9: Comparison of settled coefficients with Katz and Plotkin (2001) and Drela and Youngren (2014).

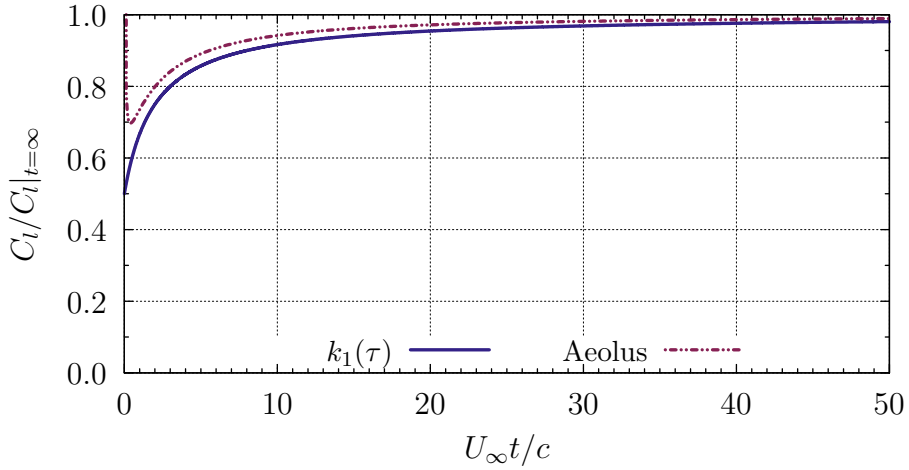


Figure 3.10: Comparison of impulse response with a rational approximation to Wagner's function (Garrick, 1938)

AVL. Therefore, the steady response is assumed to be accurate with the discrepancy in the comparison with Katz and Plotkin (2001) attributed to the different methods of load calculation.

The unsteady lift response of a flat plate aerofoil to an impulsive start is described by Wagner's function, $k_1(\tau)$,

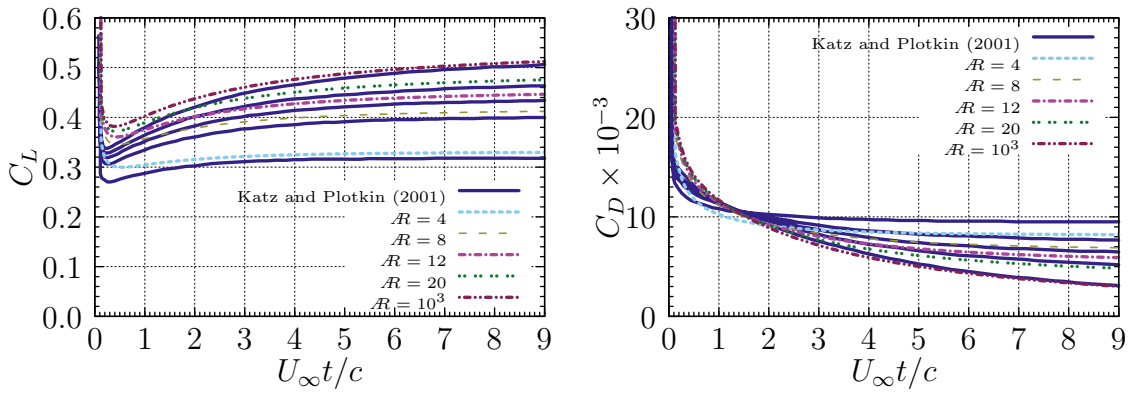
$$L = \pi\rho c U_\infty U k_1(\tau)$$

where $U = U_\infty \sin\alpha$ is the relative velocity, c is the chord and $\tau = Udt/c$. Garrick (1938) suggests

$$k_1(\tau) = 1 - \frac{2}{4 + 2\tau} \tag{3.22}$$

as a good approximation to Wagner's function, agreeing within 2% over the entire range $0 < \tau < \infty$. Figure 3.10 shows a comparison with the centreline loads from the developed code for an aspect ratio $O(10^3)$. As the aspect ratio increases, 3D effects associated with the wing tips become less significant and hence the asymptote approaches the 2D value obtained from Equation 3.22.

The initial transient in Figure 3.10 is a result of the unsteady force given by Equation 3.16. For an impulsive start the initial rate of change of circulation is infinite, theoretically. However, the effect is rapidly reduced and the unsteady transient response decays with time allowing the lift to converge gradually to Wagner's result.



(a) Lift Coefficient.

(b) Drag Coefficient.

Figure 3.11: Comparison of impulse response with Katz and Plotkin (2001).

This is consistent with the findings of Graham (1983), who used a point vortex wake and potential flow around a Kármán-Trefftz aerofoil to investigate the starting flow around an aerofoil. Furthermore, Wagner's result was derived assuming a planar wake, whereas Aeolus assumes a free wake. Consequently, there is a slight increase in the lift predicted by Aeolus.

Once again, the verification of the impulse response can be extended to 3D by comparison with Katz and Plotkin (2001), shown in Figure 3.11. The difference in the steady values has already been discussed, and is attributed to the difference in the load calculations. Therefore, the principle difference between the two methods is in the strength of the initial transient. Both models were run with the same parameters: $n_x = 5$, $n_y = 14$ and $U_\infty dt/c = 0.0625$. However, Katz and Plotkin (2001) note that the initial transient is sensitive the positioning of the trailing wake vortex filament: in their model they suggest positioning the shed filament slightly closer to the trailing edge than given by Equation 3.10, justified as the difference between a discrete vortex and continuous sheet of vorticity, which will increase the amplitude of the transient response. This approach has not been adopted in the current implementation and as such there exists the discrepancy seen in Figure 3.11.

Further verification of the unsteady response in the wing case is given by comparison with the results of Theodorsen (1935). Based on velocity potentials of the circulatory

and non-circulatory flow, Theodorsen derived expressions for the response of an aerofoil to sinusoidal pitching, α, and heaving, h, motions. The lift force is

$$P = -\pi\rho b^2(U\dot{\alpha} + \ddot{h} - ba\ddot{\alpha}) - 2\pi\rho UbC(k)Q \tag{3.23}$$

and pitching moment

$$M_\alpha = -\pi\rho b^3\left[\left(\frac{1}{2} - a\right)U\dot{\alpha} + b\left(\frac{1}{8} + a^2\right)\ddot{\alpha} - a\ddot{h}\right] + 2\pi\rho Ub^2\left(a + \frac{1}{2}\right)C(k)Q \tag{3.24}$$

where b is the half chord, a is the coordinate of the pitch axis and

$$Q = U\alpha + \dot{h} + b\left(\frac{1}{2} - a\right)\dot{\alpha}.$$

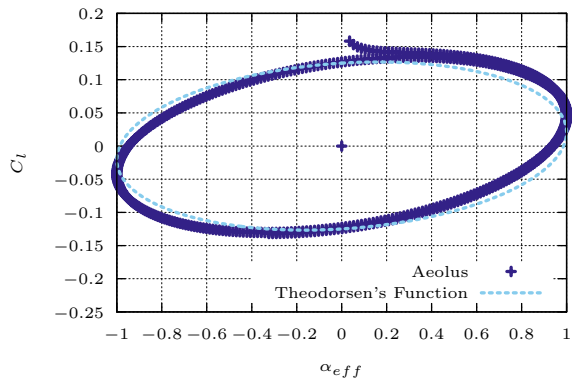
Garrick (1936) extends this to give an expression for the unsteady drag

$$P_x = \pi\rho\Re\left(S\right)^2 + \alpha\Re\left(P\right) \tag{3.25}$$

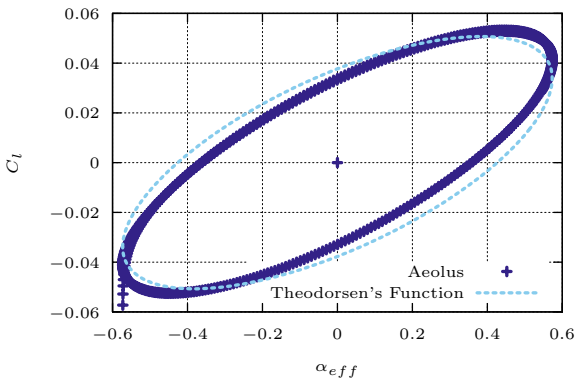
where $S = (\sqrt{2}/2)\left[2C(k)Q - b\dot{\alpha}\right]$ is the suction force. These analytical results are compared with the centreline forces of an $\mathcal{AR} = O(10^3)$ wing due to forced sinusoidal pitching and heaving motion of the developed model at a reduced frequency $k = \omega b/U_\infty = 1.0$ in Figure 3.12. The amplitude of the pitching motion is 1° and the heaving is $h = 0.01$ m.

In general the agreement is found to be acceptable with the biggest discrepancies in the drag and pitching moments, in particular the drag for the case of heaving motion. Both the drag and pitching moment will be more sensitive than the lift to small changes in the incident velocity. As with Wagner's function, Theodorsen derives the above results assuming a planar wake. Whilst the wake in Aeolus was frozen, the relative motion of the trailing edge still imparts a 3D structure, which will modify the velocities on the blade and accounts for the small discrepancies in the results.

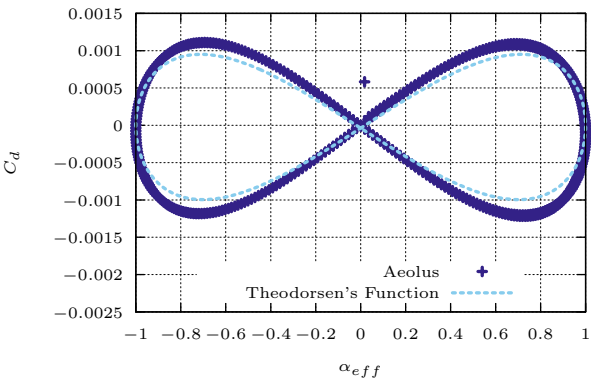
Finally, comparison with results from Katz and Plotkin (2001) are used to extend the heaving motion verification to 3D, shown in Figure 3.13. The agreement is good, although there appears to be a slight phase lead in the $k = 0.1$ case and a slight phase lag in the $k = 0.5$ case, which may simply be a misalignment of the plots as



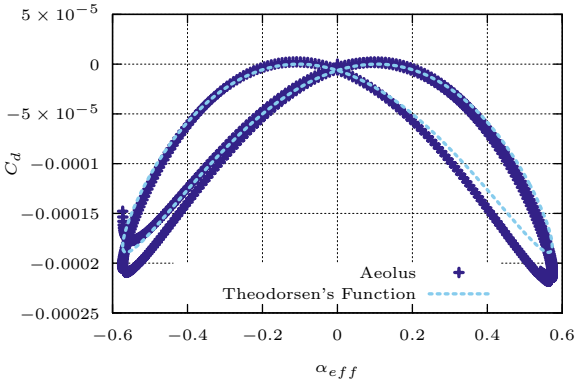
(a) Pitching - Lift Coefficient.



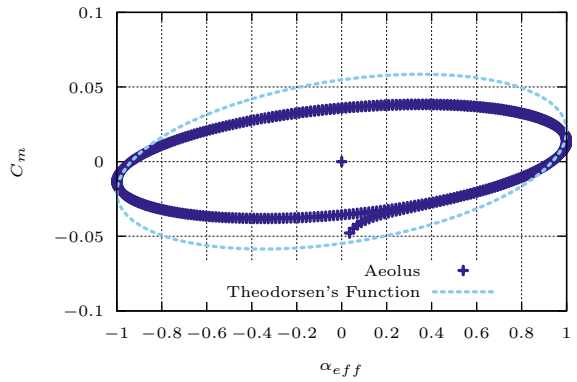
(b) Heaving - Lift Coefficient.



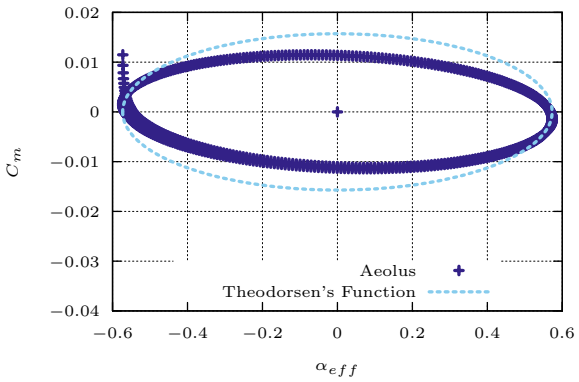
(c) Pitching - Drag Coefficient.



(d) Heaving - Drag Coefficient.



(e) Pitching - Pitch Moment Coefficient.



(f) Heaving - Pitch Moment Coefficient.

Figure 3.12: Comparison of response to pitching and heaving motion at $k = 1.0$ with the analytical results of Theodorsen (1935) and Garrick (1936).

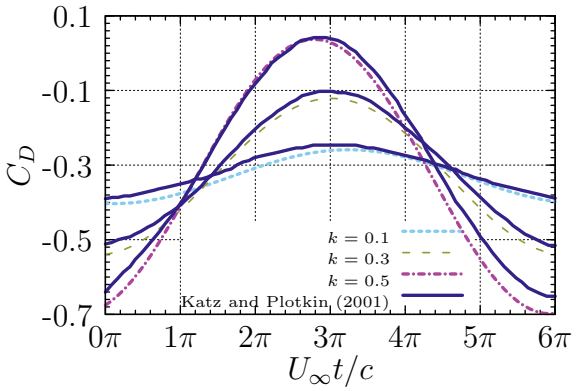


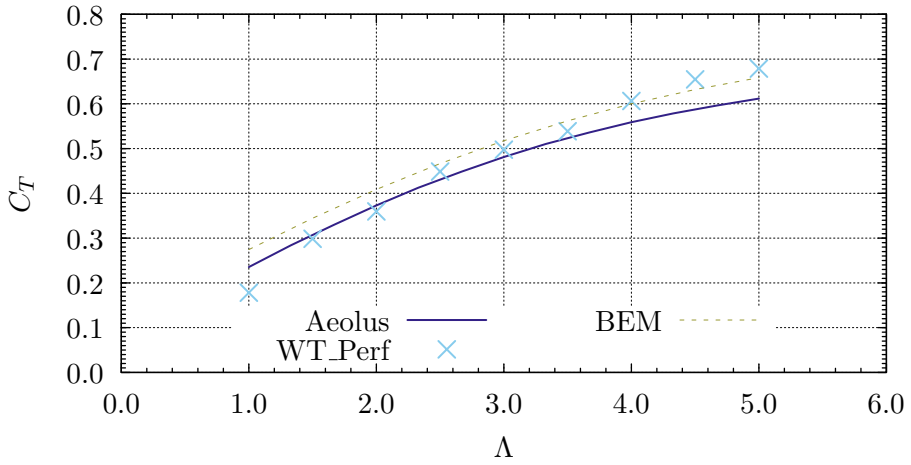
Figure 3.13: Comparison of heave response with Katz and Plotkin (2001).

it is not entirely clear from what point Katz and Plotkin (2001) define the settled response. There is also a small difference in the magnitudes, the largest being 7%, which most likely derives from the issues regarding positioning of the trailing wake filament, as discussed previously.

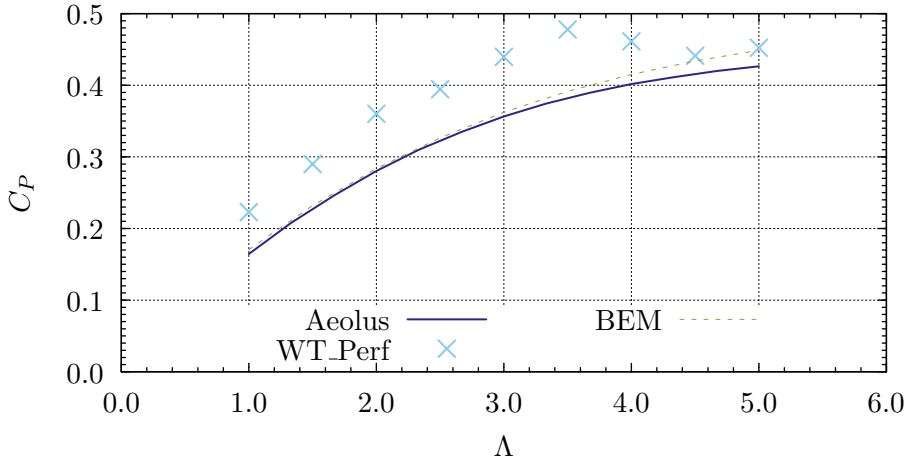
3.9.2 Rotor case

Having verified the wing response, the next step is to compare with the results of Blade Element Momentum theory, see e.g. Leishman (2006), for uniform inflow, shown in Figure 3.14. This represents the simplest flow scenario minimising both 3D flow and dynamic inflow effects. For a direct comparison with the potential flow results of Aeolus, thin aerofoil theory load coefficients, $C_l = 2\pi \sin(\alpha)$ and $C_d = 0$, are assumed in the BEM code. In addition, Prandtl tip and hub losses are applied as the associated 3D effects are expected to be implicitly modelled by Aeolus. The blade modelled corresponds to the rotor used in the experiments, described in Section 1.3.

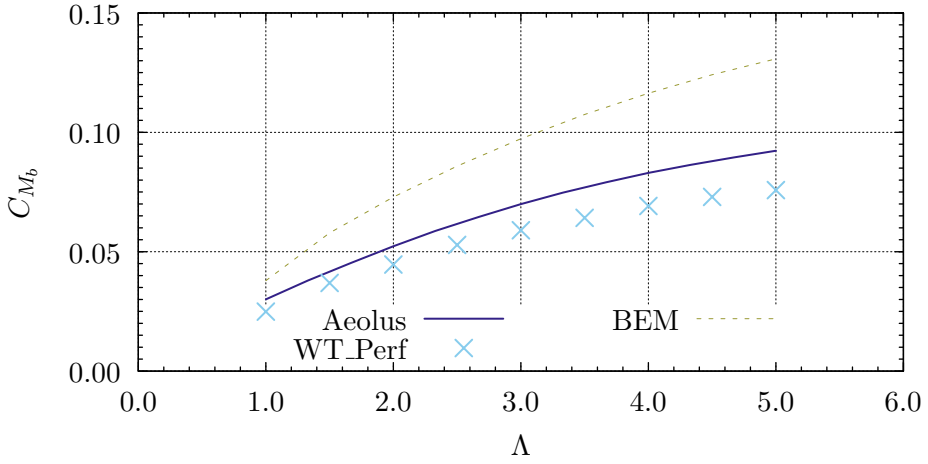
Results from the WT_Perf BEM code developed at NREL (Platt, 2012) are also included in Figure 3.14. It is noted that the authors of the WT_Perf code have discontinued distribution due to 'known bugs'. This presumably accounts for some of the discrepancy between the two BEM implementations and discontinuities in the WT_Perf results. However, as the agreement is generally acceptable it is assumed that the BEM is adequate for comparison with Aeolus.



(a) Rotor thrust coefficient.



(b) Rotor power coefficient.



(c) Blade root bending moment coefficient.

Figure 3.14: Comparison of Aeolus with Blade Element Momentum (BEM) theory.

Good agreement is found for the thrust coefficient, with Aeolus predicting marginally lower values compared with both BEM implementations. The maximum difference in the thrust coefficient is 9%, excluding $\Lambda = 1$, which is 32% larger for WT_Perf or 15% smaller than the BEM.

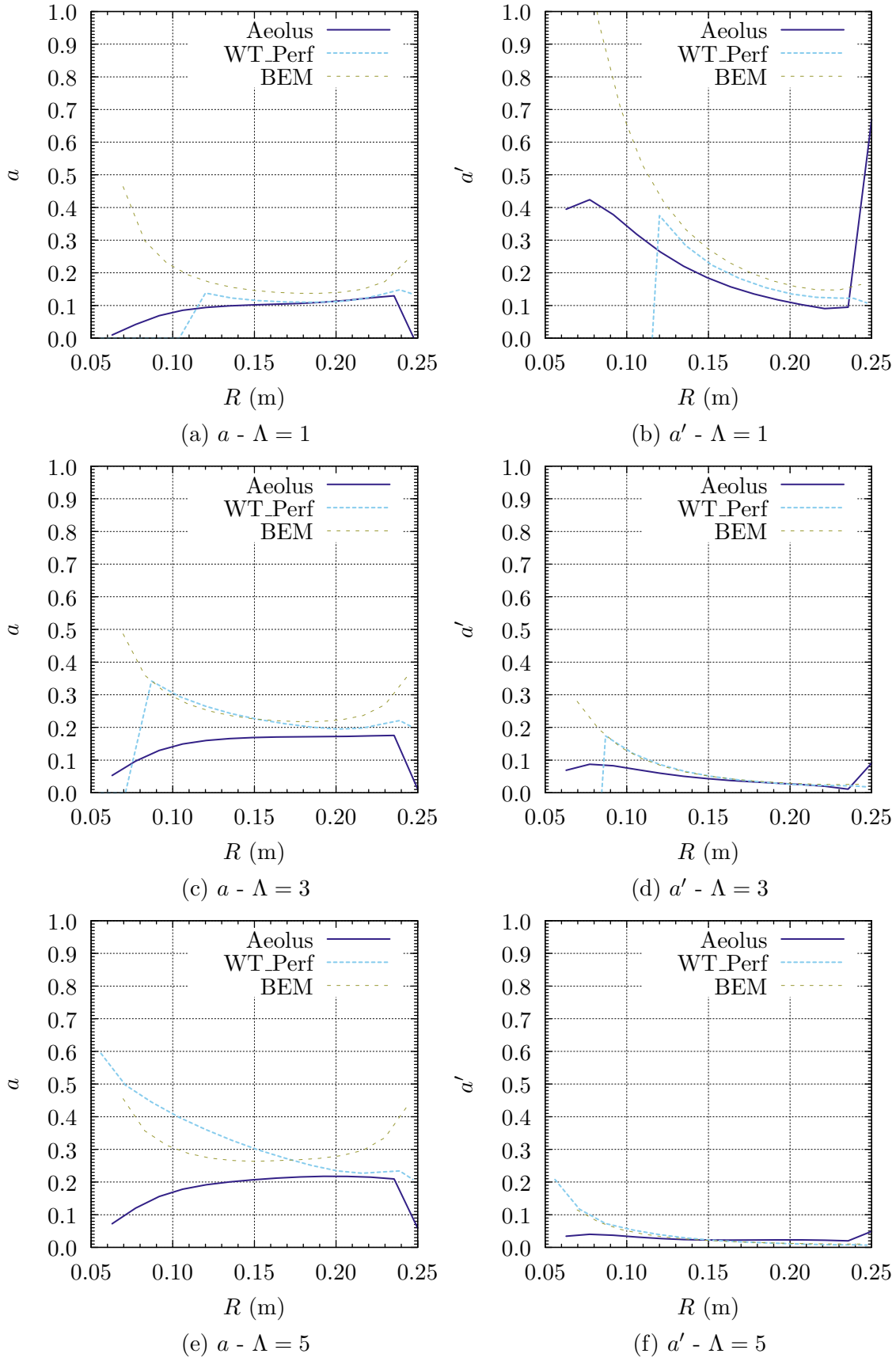
Similarly, the power coefficient is also in reasonable agreement, although WT_Perf predicts values around $20\% - 25\%$ higher for $\Lambda \leq 4$ than either the BEM or Aeolus. The agreement between the latter two is within 5% and is better at low Λ than high.

Conversely, WT_Perf gives better agreement than the BEM with Aeolus for the blade root bending moment coefficient, although the difference is still approximately 20% reduction in all cases. The BEM predicts bending moment coefficients that are $20\% - 30\%$ higher, increasing with tip speed ratio.

A comparison of the blade induction factors, shown in Figure 3.15, clarifies some of the differences between the models. The induction factors in Aeolus are evaluated at the pitch axis of the blade. The trends are generally in good agreement, with the two BEM methods matching quite closely in most cases. The principle differences are at the tip and root of the blades, corresponding to the regions where 3D effects will be most dominant. The values from Aeolus are of the similar order over much of the span, generally agreeing reasonably well with WT_Perf in the region just prior to the tip.

The BEM axial induction factor at the root of the blade is significantly higher than the Aeolus values. As a result the equivalent load point of the thrust will shift towards the tip of the blade, giving the increased bending moments seen in Figure 3.14c. Conversely, the WT_Perf code appears to have problems converging the induction factors at the root for the lower Λ, resulting in higher loading towards the root and hence reduced bending moment. Given the increased swirl induction at low Λ, this discrepancy also accounts for the difference in power.

Overall, the agreement is found to be acceptable, notwithstanding the identified issues with the BEM models.



(a) a - $\Lambda = 1$ (b) a' - $\Lambda = 1$

(c) a - $\Lambda = 3$ (d) a' - $\Lambda = 3$

(e) a - $\Lambda = 5$ (f) a' - $\Lambda = 5$

Figure 3.15: Comparison of time averaged induction factors from Aeolus and Blade Element Momentum (BEM) theory.

3.10 Summary

An unsteady implementation of the vortex lattice method has been presented, including details of the approach to desingularisation of the induced velocities, calculation of the aerodynamic loads and modelling of a spatially varying wind field.

The model was found to agree well with existing models of the turbine rotor and flat plate wing, as well as analytical solutions for the latter. Before the developed model can be used to make predictions it must also be validated against actual measurements of the loading on a turbine.

4 Generating a validation database: Wind tunnel measurements

As discussed in the literature review, Section 2.4, Adaramola and Krogstad (2011) identified a shortage of sufficiently detailed experimental data for validation of numerical modelling of turbines operating under the influence of an upstream rotor wake. Therefore, a series of experiments have been conducted with the objectives of generating a validation database for the numerical model presented in Chapter 3 and identifying the effects of ambient turbulence and wake impact on the downstream rotor. These subdivide into two main categories: a characterisation of the wake profile, discussed in Section 4.2, and time histories of the rotor loading (thrust and blade root bending moment), discussed in Section 4.3. Preceding the presentation of these results, a description of the experimental setup is provided.

4.1 Experimental setup

The experiments were performed in the closed circuit Honda wind tunnel at Imperial College London. The working section has a 3.05×1.524 m^2 cross section and is 9.0 m long. The flow is driven by twin axial fans and has an empty tunnel range of $0 - 40$ m s^{-1} with turbulent intensity of less than 0.25% and a flow uniformity of $\pm 1\%$ (Imperial College London, 2012).

For all test cases, a mean free stream velocity of 12 m s^{-1} was maintained using a Proportional-Integral-Derivative (PID) controller acting on the tunnel voltage. The tunnel velocity was measured using a pitot-static tube, connected to FCO510 Micromanometer with a sampling rate of 5 Hz, located at the inlet to the working section. The fractal turbulence grid, used to generate ambient turbulence (Section 4.1.3), interfered with the pitot-static measurements. Therefore, pressure tappings in the wind tunnel contraction walls were used as an alternative to calculate the flow velocity, again via the FCO510 Micromanometer, in the presence of the grid. The tappings are located at the start and end of the contraction, with the latter

0.863 m upstream of the grid position. The velocities were calibrated according to the method described in Appendix A.3 to give a reference velocity of $U_\infty = 12$ m s^{-1} at the centre of the rotor plane.

The instrumented turbine and upstream rotor wake generator used in the wind tunnel test were based on the Exemplar 5MW turbine, as discussed in Section 1.3. Two 1 : 250 scale model turbines ($D = 0.5$ m) were manufactured in-house for the experiments. The blades were manufactured using an Objet Connex 3D Printer and Digital ABS material and reinforced with an aluminium rod along the pitch axis, which also provided a means of connecting the blades to the hub.

A schematic of the tunnel layout is shown in Figure 4.1. The instrumented turbine has a 0.1 m hub that houses the wireless radio telemetry used to transmit the signal from a strain gauge located at the root of one of the blades. It was manufactured using machinable plastic to ensure transparency to the radio signal. As only one channel was available on the wireless telemetry, the flapwise moment was chosen as Frandsen (1996) indicates that this gives the best representation of the turbine loading under different load cases. The instrumented turbine is mounted onto a shaft protruding from a streamlined nacelle, which is connected to a ZF EBU 250/1 hysteresis brake and Hengstler RI 38 encoder for position and velocity measurements. Hysteresis brakes are capable of infinitely adjustable torque that is largely independent of rotation velocity making them ideal for controlling a model turbine. The instrumented turbine was positioned such that the hub centre was coincident with the tunnel centre line at approximately 6 m downstream of the inlet to the working section. This corresponds to a height of 0.77 m above the section floor and 1.5 m from the side walls. It was mounted on a steel strut of circular cross-section, fixed to the tunnel frame through a hole in the tunnel floor.

The upstream rotor wake generator was mounted on a 0.04 m hub made from aluminium. Similar to the instrumented turbine, this was mounted onto a shaft connected to a Magtrol HB-140M-2 hysteresis brake and US Digital EM1 encoder enclosed in a streamlined nacelle. The upstream rotor was located $6.5D$ ahead of the instrumented rotor at the same hub height. It was mounted on a rectangular

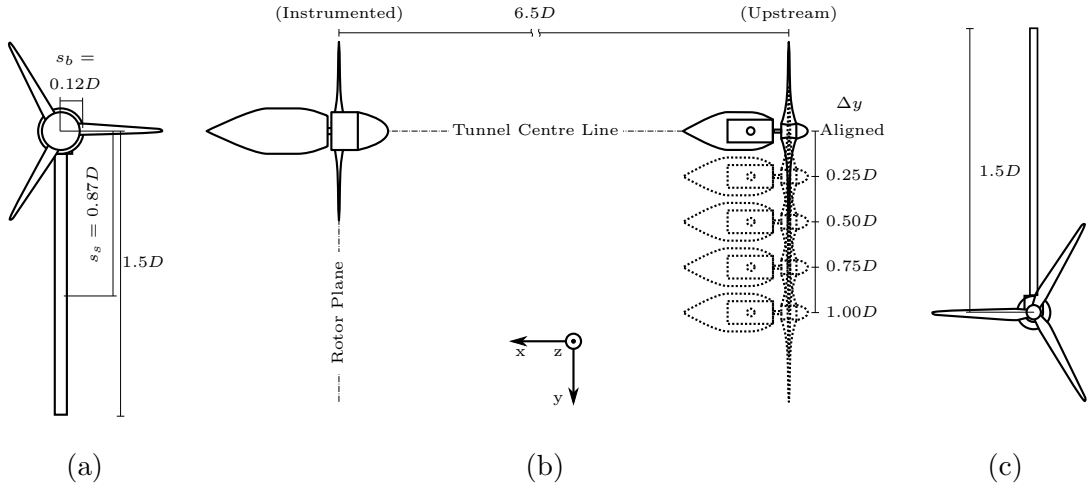


Figure 4.1: Schematic of experimental setup: a) Instrumented turbine, where s_b and s_s denote the position of blade and strut strain gauges, respectively; b) Top down view of tunnel layout, flow direction is in positive x; c) Upstream rotor wake generator. $D = 0.5$ m for both rotors.

strut supported through the tunnel roof, bolted to a steel plate with holes drilled at lateral offsets of $\Delta y = 0.0 - 1.0D$ from the tunnel centreline in $0.25D$ steps.

When both turbines were installed in the tunnel, they were operated at the same tip speed ratio, relative to the free stream velocity, i.e. with the same rotational velocity. The rotational velocity was measured using the digital encoders and matched and maintained via PID control applied to the hysteresis brakes installed in each turbine.

4.1.1 Scaling

As previously discussed, the wind tunnel experiments were conducted at a physical scale of 1:250. In order for the results of the experiments to be physically consistent, in addition to the rotor geometry the following dimensionless quantities need to be matched with the full scale flow (Vries, 1983; Adaramola and Krogstad, 2011):

1. Tip speed ratio, Λ;
2. Tip Mach number, M_t;
3. Reynolds number, based on blade chord c, Re_c.

Of these parameters, the first is both the easiest to match and most important in terms of turbine performance characteristics. It is therefore assumed that $\Lambda = \Lambda_m = \Lambda_f$, where subscripts m and f denote the model and full scales, respectively.

The tip Mach number, based on the local velocity at the tip, is given by

$$M_t = \frac{\sqrt{\Omega^2 R^2 + U_\infty^2}}{a_\infty} = \frac{U_\infty \sqrt{\Lambda^2 + 1}}{a_\infty}$$

where a_∞ is the speed of sound in the standard atmosphere. Noting the previous equality, it follows that $U_\infty = U_{\infty,m} = U_{\infty,f}$. As most current turbines operate at wind speeds between $4 - 26$ m s^{-1} (Kjaer et al., 2009) this condition is also straightforward to apply in the Honda wind tunnel. However, whilst applied in the experiments, matching of the tip Mach number is only relevant in terms of incompressibility, in a practical sense requiring $M_t < 0.3$, and is otherwise unimportant.

The blade chord Reynolds Number is given by

$$\mathrm{Re}_c = \frac{\rho_\infty c \sqrt{\Omega^2 R^2 + U_\infty^2}}{\mu_\infty} = \frac{\rho_\infty c U_\infty \sqrt{\Lambda^2 + 1}}{\mu_\infty}$$

where ρ_∞ is the density of air and μ_∞ the dynamic viscosity of air. Again noting the tip speed ratio equality, it follows that

$$U_{\infty,m} = \frac{c_f}{c_m} U_{\infty,f}$$

which violates the tip Mach number equality except at full scale. Increasing the size of the rotor is not practical due to the increased blockage that would result. Therefore, it is not possible to match the Reynolds number even approximately.

Vries (1983), among others, notes that it is not possible to match all parameters, but concludes that it is not necessary to obtain the full scale Re_c as long as a certain minimum is achieved. The suggested value is $\mathrm{Re}_c > 3 \times 10^5$, although this is inconsistent with the value given by Sørensen et al. (1998) based on the rotor radius, discussed previously. Given that $\mathrm{Re}_c = \left(\text{Æ}/\sqrt{\Lambda^2 + 1}\right) \mathrm{Re}_R$ where Æ is the aspect ratio, the value given by Sørensen et al. (1998) is approximately equivalent to $\mathrm{Re}_c > 2 \times 10^4$. The blade chord Reynolds number in the following experiments was $O(2 - 6 \times 10^4)$ depending upon tip speed ratio and radial position along the

blade. Consequently, the drag will be increased, the blades will stall earlier giving a reduced maximum lift and the lift curve slope will be reduced relative to the full scale turbine.

However, as noted by several authors (Grant et al., 2000; Vermeer et al., 2003; Adaramola and Krogstad, 2011), for the purpose of validation of numerical modelling these considerations are of limited significance as the simulations can be matched to the model scale. The vortex lattice method implicitly assumes $Re_c = \infty$ (Whale et al., 2000) due to the inviscid and irrotational approximations. Whale et al. (2000) find that for blade chord Reynolds numbers $O(10^3)$ smaller than the full scale $O(10^6)$, experimental results still share the same fundamental characteristics in the near wake. Furthermore, the authors hypothesise that a rotating wing generating circulatory lift and shedding vorticity may give rise to an inviscid wake. Therefore, assuming the inviscid and irrotational assumptions hold, the Reynolds number scaling will be neglected in the experimental setup.

4.1.2 Blockage

Another important consideration for wind tunnel simulation is the degree of blockage of the test model, and the corresponding effects on the tunnel flow. Blockage is defined as the ratio of the swept area of the model to the cross-sectional area of the test section. The turbine used in the experiments has a rotor blockage ratio of 0.042. Chen and Liou (2011) investigated the impact of different rotor blockage ratios and the necessary blockage corrections and found, in agreement with other experiments in the literature, that for a rotor blockage ratio below 0.10 no correction is required. Furthermore, Adaramola and Krogstad (2011) argue that the effect of blockage can be neglected as long as the turbine wake is allowed to expand freely. As will be seen in Section 4.2, this is the case in the following experiments.

4.1.3 Fractal grid turbulence

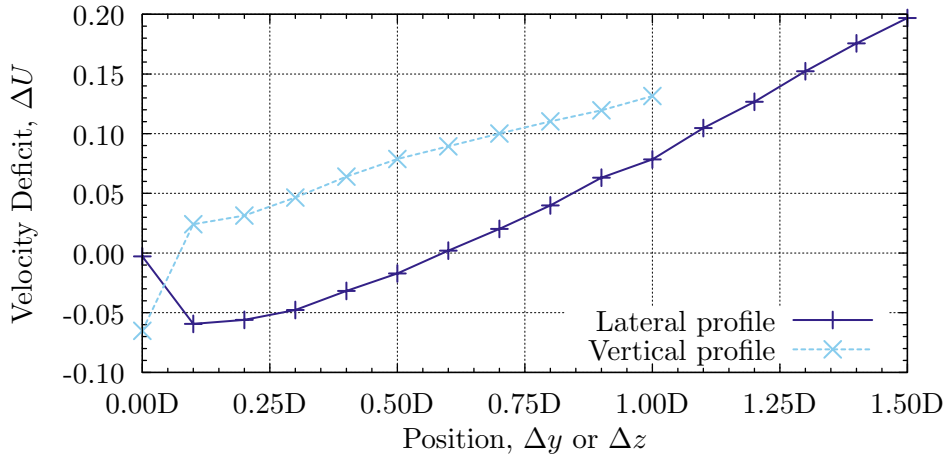
A multi-scale turbulence fractal grid designed by K. Gouder at Imperial College London, based on the work of Hurst and Vassilicos (2007), was used to simulate turbulence in atmospheric conditions. The advantage of this type of grid over more classical designs is multiple scales of turbulence with a larger integral lengthscale and closer agreement with the von Kármán (1948) spectrum. Each iteration of the fractal pattern is a factor 0.342 of the previous, with 4 levels of the pattern realised. The grid was positioned at the inlet to the working section, $12D$ upstream of the instrumented turbine, such that the turbulence profiles should be relatively homogeneous in the rotor plane (Gouder (2014), priv. comm.).

In order to characterise the turbulence in the rotor plane, measurements were carried out using hot-wires, according to the method presented in Section 4.2. Figure 4.2 shows the turbulence profiles at the downstream (instrumented) rotor position with $\Delta y = \Delta z = 0$ corresponding to the tunnel centreline. The lateral profile, along the y ordinate, was taken at hub height and the vertical profile, along the z ordinate, aligned with the rotor position. A clear jet can be seen in the velocity deficit,

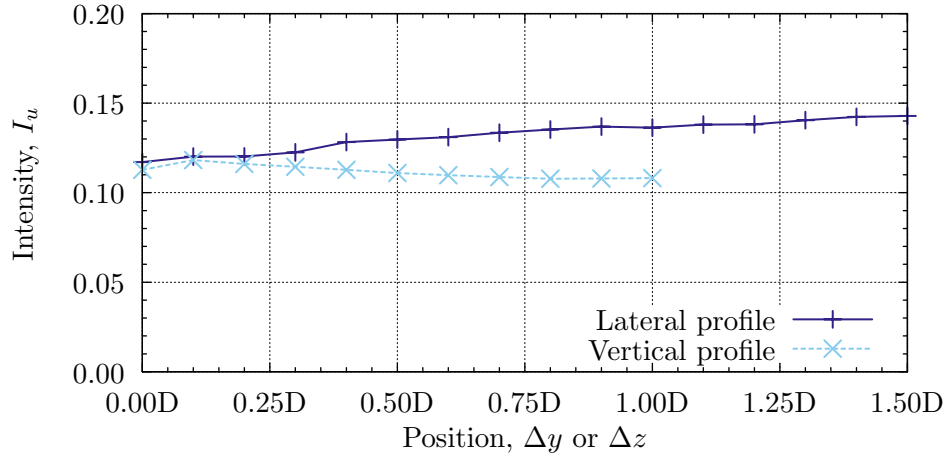
$$\Delta U = \frac{U_\infty - U}{U_\infty} \tag{4.1}$$

which is normalised by the mean incident velocity defined as the reference velocity $U_\infty = 12$ m s^{-1}. This is due to the low degree of blockage in the centre of the grid and wide uprights positioned roughly $\Delta y = 1.00D$ from the centreline. However, the lateral profile remains within 6% of the desired free stream, whilst the vertical profile drops off more rapidly with distance, reaching 8% deficit by $\Delta z = 0.50D$.

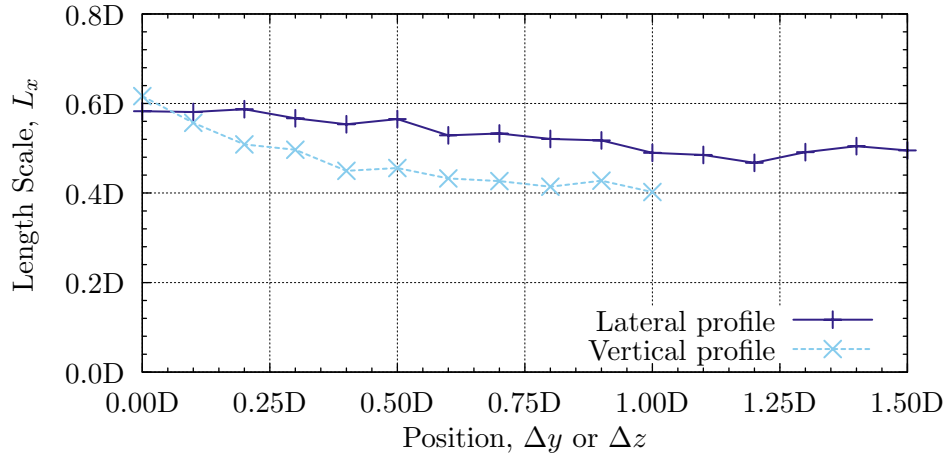
Both the turbulence intensity, I_u, and length scale, L_x, calculated by fitting the von Kármán (1948) spectrum and normalised by the rotor diameter, are approximately constant within the swept area of the rotor, although the length scale decreases quite sharply in the vertical profile. The turbulence intensity is $12 - 13\%$ and the length scale is $0.55 - 0.59D = 0.28 - 0.3$ m, decreasing linearly to $0.45D$ at the blade tip, and $0.4D$ at the extreme of Δz, in the vertical profile. Whilst the turbulence intensity increases with Δy beyond the rotor swept area, the length scale decreases



(a) Mean velocity deficit



(b) Turbulence intensity



(c) Normalised length scale

Figure 4.2: Fractal grid generated turbulence profiles at the downstream rotor position.

to approximately $0.5D$ at the extreme of the recorded measurements. Finally, the turbulence intensity in the vertical profile is reasonable constant even beyond the rotor swept area.

The Power Spectral Density (PSD) at each of the positions in the swept area of the rotor is presented in Figure 4.3. Using an average of the measured turbulence intensity, $I_u = 0.13$, and the reference velocity, $U_\infty = 12$ m s^{-1}, the von Kármán spectrum was fitted to the results using a least squares type method. The resulting fit yields a length scale of $L_x = 0.29$ m and shows good agreement with the measured values. As such, the aforementioned parameters will be used for numerical simulation of the ambient turbulence.

The lateral and vertical coherences, relative to the centreline, in the rotor plane are shown in Figure 4.4. The measurements were taken with one hot-wire fixed at the tunnel centreline and the other offset by either Δy or Δz within the rotor plane. The measurements are compared with the coherence of the von Kármán spectrum, given by Equation 2.4 in Section 2.1.1. At $f = 1$ Hz the measured coherence is noticeably lower than that predicted coherence. However at higher frequencies the agreement is shown to be acceptable. Therefore, the von Kármán coherence model will be used to model ambient turbulence in the numerical simulation, congruent

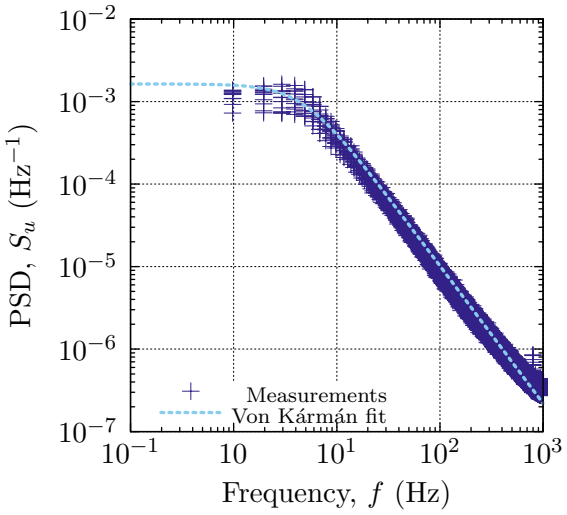
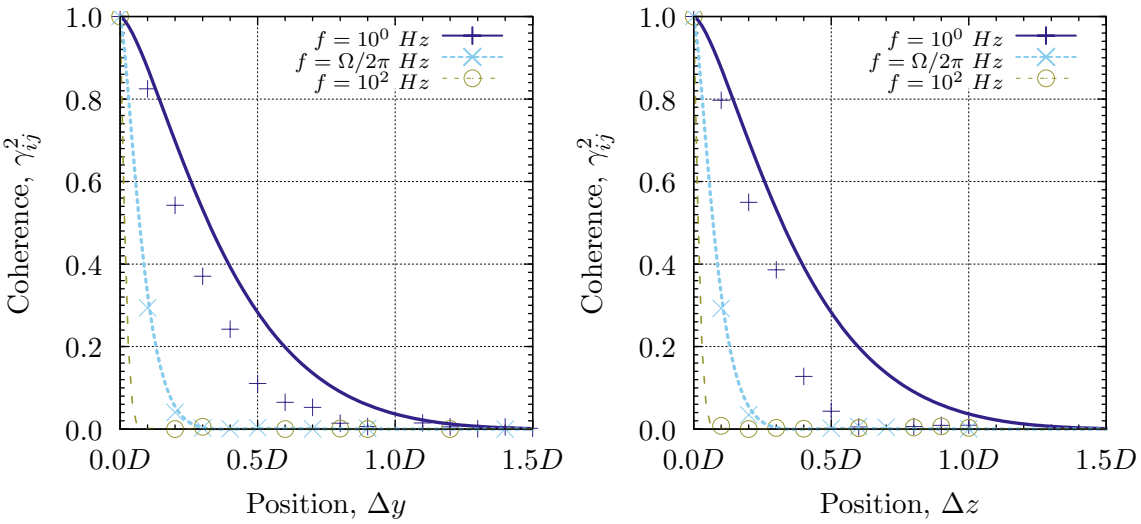


Figure 4.3: Spectra within the swept area of the rotor behind fractal turbulence grid compared with von Kármán spectrum ($U = 12$ m s^{-1}, $I_u = 0.13$ and $L_x = 0.29$ m).



(a) Lateral coherence

(b) Vertical coherence

Figure 4.4: Comparison between measured (symbols) and von Kármán (lines) coherence behind fractal turbulence grid.

with the model for the spectra.

4.2 Wake measurements

In order to model the upstream rotor wake accurately, it is necessary to characterise the mean and fluctuating velocity and turbulent length scale profiles. The upstream rotor wake structure and turbulence characteristics were investigated using two point hot-wire measurements in the downstream rotor plane. A fixed single-sensor Dantec Dynamics 55P16 probe was mounted in the rotor plane at hub height on the tunnel centreline. A secondary matching probe was then mounted in a traversing mechanism and positioned between $\Delta y = 0.1D - 1.5D$ along the y ordinate or $\Delta z = 0.1D - 1.0D$ along the z ordinate in $0.1D$ increments. In the following text the latter probe will be referred to as the non-fixed probe.

The hot-wire voltage signals were acquired via a Dantec Dynamics 54T42 MiniCTA. Measurements were recorded for both the axially aligned and $\Delta y = 1D$ positions of the upstream rotor. The sampling rate was chosen as $f_s = 2$ kHz and the sample length $N = 2048$ to give a spectral resolution of just under 0.5 Hz. The statistical

accuracy of the measured spectra, i.e. how accurate the estimate is to the true spectrum, is given by Bruun (1995) as

$$\%\epsilon = \frac{z_\alpha}{\sqrt{n_d}} \tag{4.2}$$

where n_d is the number of sub-samples and $z_\alpha = 1.96$ for 95% confidence. Therefore, $n_d = 385$ sub-samples were recorded for each position to give a statistical accuracy of $\pm 10\%$ with 95% confidence.

The hot-wires were calibrated before and after each run according to the method set out in Appendix A.2, where each of the individual calibration curves (polynomial fit) can also be found. The data was corrected for temperature variation according to (Jørgensen, 2002):

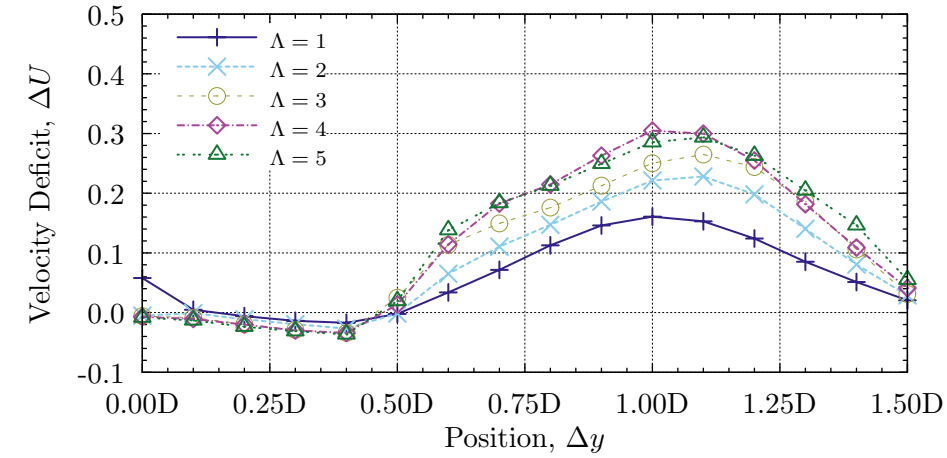
$$V_c = \sqrt{\frac{\Theta_w - \Theta_0}{\Theta_w - \Theta}} V \tag{4.3}$$

where $\Theta_w = 160°$ is the overheat temperature, $\Theta_0 = 30°$ is the reference temperature and Θ and V are the acquisition temperature and voltage, respectively.

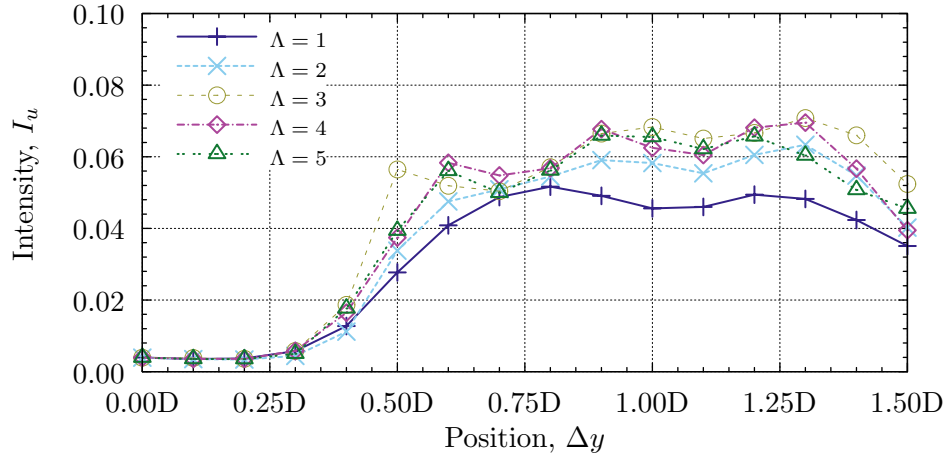
4.2.1 Wake profiles

The centreline velocity deficit, turbulence intensity and normalised length scale profiles for tip speed ratio $\Lambda = 1 - 5$ in uniform flow are shown in Figure 4.5. The profiles consist of lateral measurements starting from the tunnel centreline in the rotor plane, corresponding to $6.5D$ downstream, at hub height behind an upstream turbine mounted in the $\Delta y = 1D$ position.

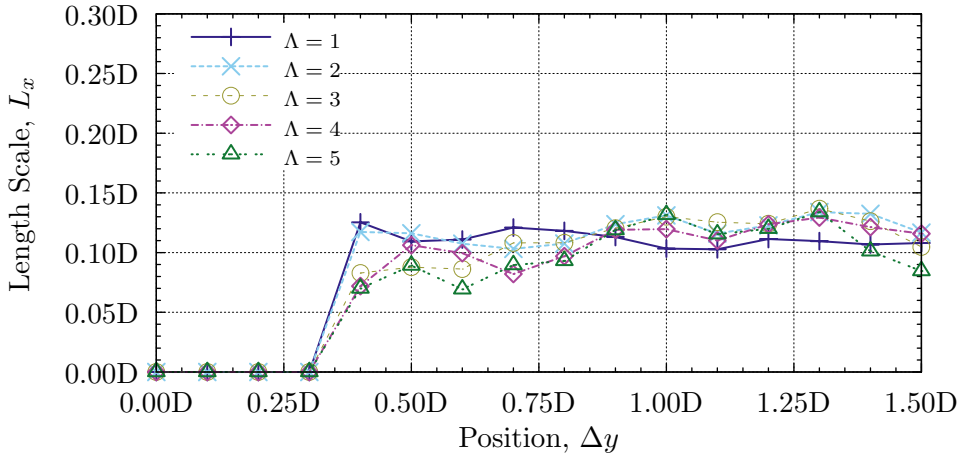
The velocity deficit increases from approximately 15% at $\Lambda = 1$ to approximately 30% at $\Lambda = 4 - 5$, with corresponding turbulence intensities of approximately 5% and 7% and normalised length scales, calculated by fitting the von Kármán (1948) spectrum, of approximately $0.10 - 0.13$. At $\Lambda = 1$ the deficit profile is approximately Gaussian with a singe peak at the wake centreline. At higher tip speed ratios, the wake profile exhibits a small degree of skew indicated by the central peak shifting $0.1D$ to the higher Δy. Given the downstream distance of $6.5D$, this would correspond to 0.9° skew in the wake trajectory. This could be explained as a twisting of



(a) Mean velocity deficit



(b) Turbulence intensity



(c) Normalised length scale

Figure 4.5: Comparison of lateral wake profiles with the upstream rotor positioned at $\Delta y = 1.00D$ in uniform flow at varying tip speed ratio, Λ.

the support plate as the turbine loading increases. When the turbine is mounted in the $\Delta y = 1D$ position the mounting points in the steel plate are beyond the position at which the plate is bolted to the tunnel frame. The free end of the steel plate is clamped via a spacer to the frame. Therefore, it is conceivable that the plate could twist slightly about this pivot point.

The turbulence intensity at $\Lambda = 1$ exhibits a double peak separated by a small dip. However, at higher tip speed ratios the turbulence intensity increases and becomes more constant across the wake width. Once again, the profile exhibits a small degree of skew, with higher intensities at higher Δy. Likewise, the normalised length scales exhibit similar behaviour, roughly constant at approximately 0.1 for all tip speed ratios.

The velocity deficit profile shows little expansion of the wake. However, both the turbulence intensity and length scale exhibit wake effects out to $\Delta y = 1.0D - 0.4D = 0.6D$ indicating approximately 20% expansion of the wake. This would imply that the diffusion of the turbulence is more rapid than that of the mean velocity deficit.

A comparison of the lateral and vertical profiles at the mid-range value of $\Lambda = 3$, chosen as the turbine should be operating below stall, is shown in Figure 4.6. Profiles for both an axially aligned and $\Delta y = 1.00D$ upstream rotor positions, relative to the tunnel centreline, are included in the figure. The $\Delta y = 1.00D$ profiles have been shifted so that $\Delta y = \Delta z = 0.0D$ corresponds to the centre of the wake in order to simplify the comparison.

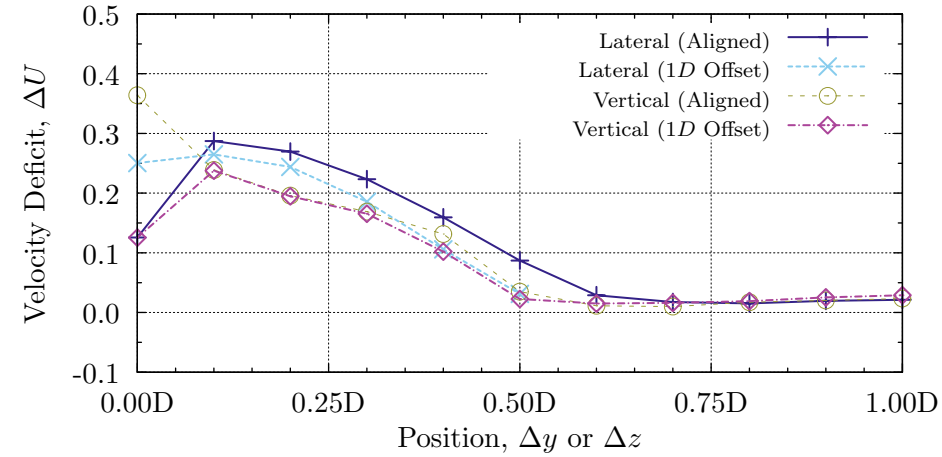
There are several anomalous readings in both figures, primarily corresponding to the fixed hot-wire measurements. One possible explanation for this is an error in the calibration of the probe, most likely caused by a local increase in the velocity of the flow due to blockage associated with the traverse. Assuming this is indeed the case, then when the non-fixed probe is repositioned the blockage would be removed modifying the readings. Figure 4.7 shows the deficit at the fixed hot-wire probe for increasing lateral separation of the non-fixed probe. Whilst the minimum deficit is only -5%, indicating an acceleration of the flow, there is a clear increasing trend

with Δy until the free stream value is recovered. It is noted that the non-fixed probe will still experience the same flow field and therefore its calibration will be accurate. In addition, the cross correlations are a measure of the frequency content rather than the amplitude and will be unaffected by any error in the calibration. It is also noted that the lateral profile with the upstream rotor in the $\Delta y = 1.0D$ position will be unaffected by this issue as the fixed hot-wire is positioned outside the wake profile. Therefore, the anomalous centreline readings will be discounted in the following discussion.

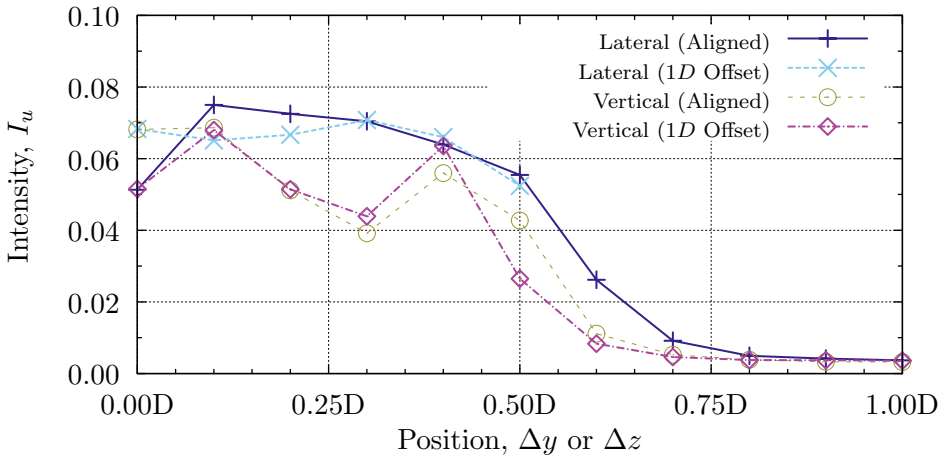
Perhaps the most significant observation is the level of agreement between both the lateral and vertical measurements, neglecting the few anomalous data points, supporting the assumption of an axisymmetric wake for the purposes of modelling. It is worth noting that the axially aligned profiles do not appear to exhibit the skew of the $1D$ profiles and indicate an increased expansion of 20% in the velocity deficit and 40% in the turbulent characteristics. In addition, the vertical profile for the $\Delta y = 1.0D$ upstream rotor position, and to some extent the axially aligned position, has a peak at the limit of the wake. This is also evident in the lateral profile of the axially aligned case, but is beyond the limit of the $\Delta y = 1.0D$ profile, and perhaps indicates the presence of the tip vortex.

A comparison of the centreline and blade tip wake turbulence spectrum with the von Kármán spectrum is presented in Figure 4.8. Using the local values of the measured turbulence intensity, $I_u = 0.05$ and the corresponding velocity yield a good agreement with the theoretical spectrum for a length scale of $L_x = 0.06$ m. This neglects the peaks at harmonics of the rotational frequency observed in the tip spectrum, which are assumed to indicate the passage of the tip vortex. As such it will be assumed in the modelling that the von Kármán spectrum may be used to simulate turbulence within the wake using the local velocity and turbulence parameters.

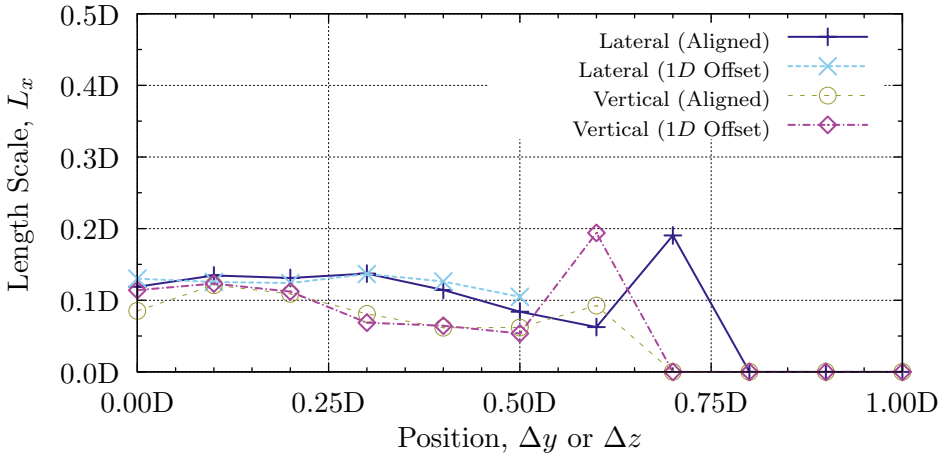
Given the choice of turbulence spectrum, the lateral and vertical coherences, relative to the centreline, are compared with the corresponding coherence of the von Kármán spectrum, shown in Figure 4.9. The agreement is generally quite reasonable, as is



(a) Mean velocity deficit



(b) Turbulence intensity



(c) Normalised length scale

Figure 4.6: Comparison of lateral and vertical wake profiles for an axially aligned and $\Delta y = 1.00D$ lateral offset upstream rotor, relative to the tunnel centreline, in uniform flow at $\Lambda = 3$.

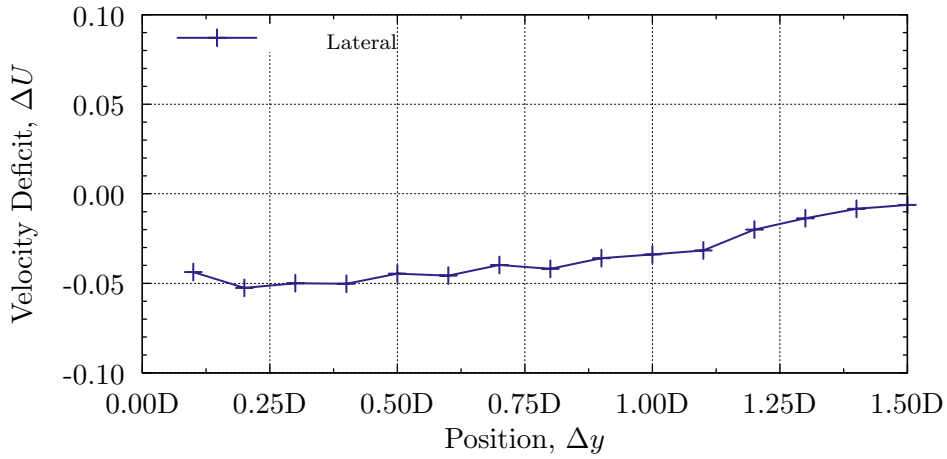
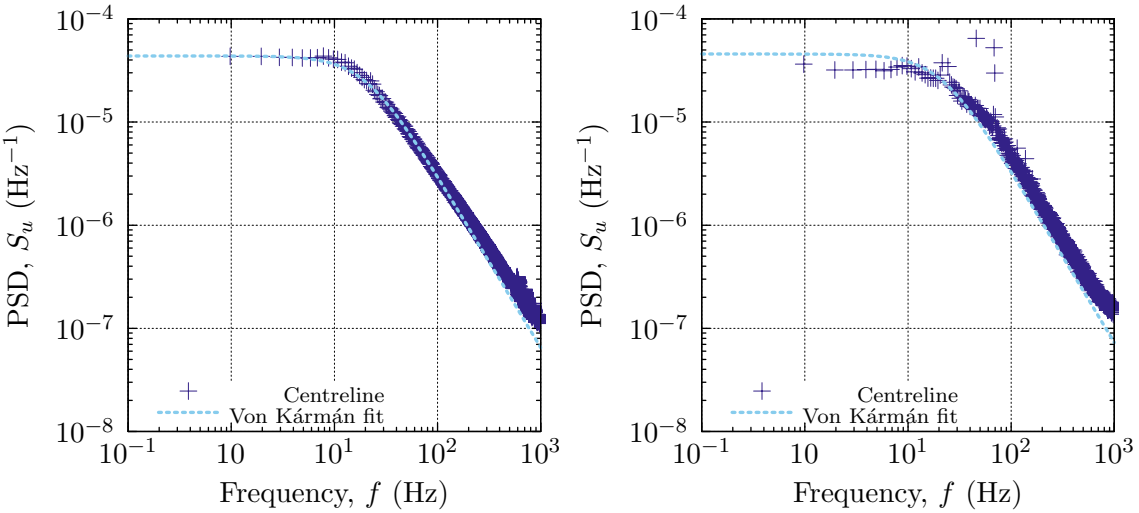


Figure 4.7: Velocity deficit measured by fixed hot-wire for each separation distance.

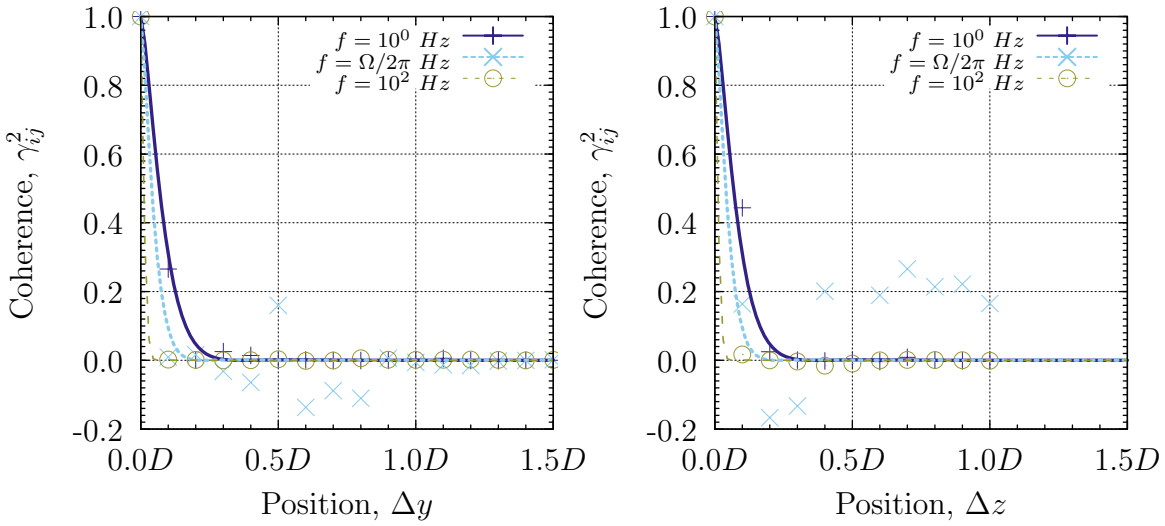
expected given the agreement in the spectra. However, there is a significant variation in the lateral coherence for $f = \Omega/2\pi$ Hz, the rotation frequency, at a position corresponding to the edge of the wake, also evident in the vertical coherence. Given the separation in the lateral coherence, and the frequency at which the peak occurs, it is assumed that this variation in coherence also corresponds to the passage of the tip vortex. Chu and Chiang (2014) also observe a similar peak in the velocity spectra and conclude that this indicates that the wake flow is strongly influenced by the tip vortex.



(a) Centreline spectrum: $U = 10.5$ m s^{-1}.

(b) Rotor tip spectrum: $U = 11.0$ m s^{-1}.

Figure 4.8: Centreline spectrum behind an aligned upstream rotor at $\Lambda = 3$ compared with von Kármán spectrum using the local velocity, $I_u = 0.05$ and $L_x = 0.06$ m.



(a) Lateral coherence

(b) Vertical coherence

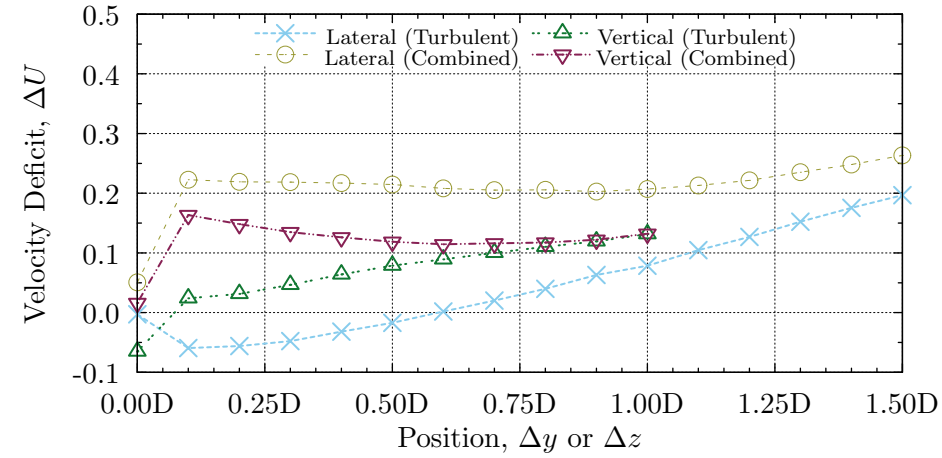
Figure 4.9: Comparison between measured (symbols) and von Kármán (lines) coherence of the upstream rotor wake at $\Lambda = 3$.

4.2.2 Combined inflow

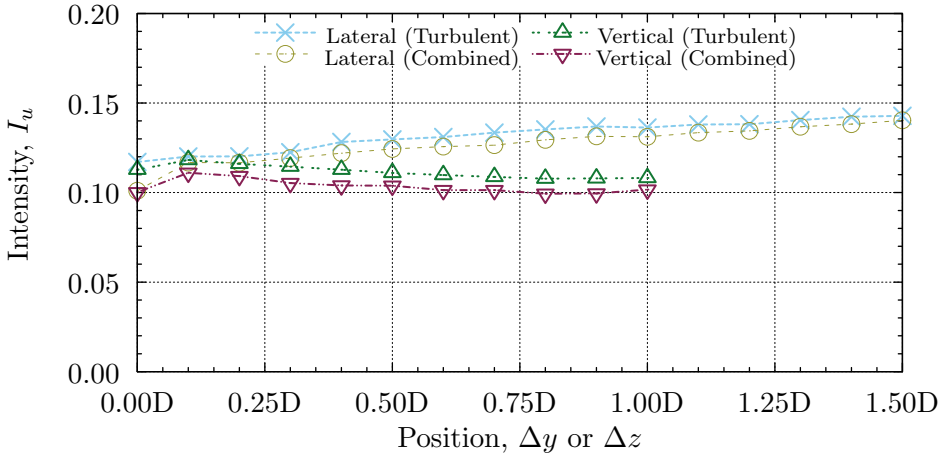
A similar set of measurements were taken for flow behind the upstream turbine, aligned with the tunnel centreline, operating in a turbulent inflow, generated by the fractal grid described in Section 4.1.3. The profiles at $\Lambda = 3$ are compared with the background turbulence profiles in Figure 4.10.

Due to the geometry of the fractal grid, only the axially aligned upstream rotor wake case is considered: lateral offset of the upstream rotor would position it behind the vertical struts of the grid where the flow conditions are uncertain.

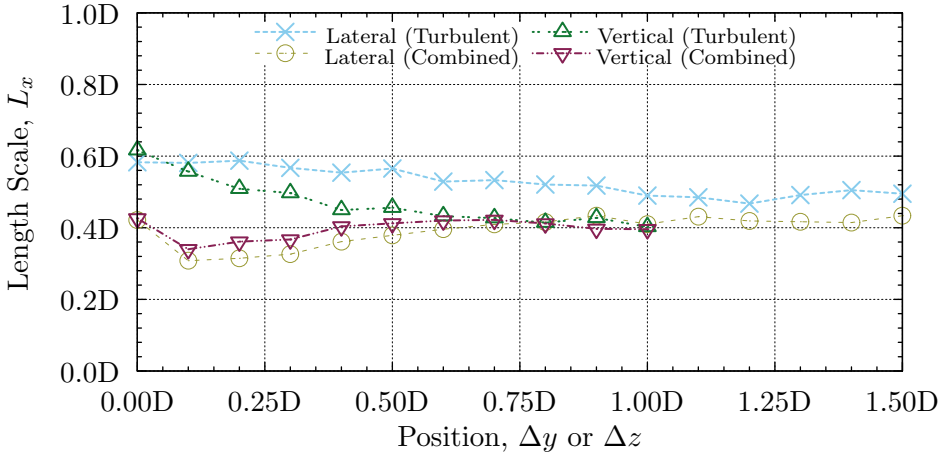
Both the lateral and vertical velocity deficit exhibit an increase associated with the momentum deficit in the wake. Whilst the vertical profile reduces to background levels by approximately $0.7D$, corresponding to a slight expansion of the wake over the uniform flow case, the lateral profile shows a distinct increase in the velocity deficit across the entire span of the measurements. The position of the upstream rotor wake generator is within the development region of the fractal grid turbulence. It is possible that, as a result of this positioning, the upstream rotor has modified the development of the turbulence profiles in the tunnel.



(a) Mean velocity deficit



(b) Turbulence intensity



(c) Normalised length scale

Figure 4.10: Comparison of combined flow upstream rotor wake profiles in turbulent inflow at $\Lambda = 3$ with the turbulence profiles.

Conversely, the length scales show a reduction in the wake region. Although, once again the vertical profile recovers the background value outside the wake, whilst the lateral profile remains lower across the span of the measurements.

The turbulence intensity profiles show a slight reduction in the upstream rotor case, which is approximately constant at all positions for both the lateral and vertical profiles. This would suggest that there is increased mixing of the upstream wakes, both from the turbine and the grid, resulting in a slight reduction in the intensity at the downstream rotor plane. This is congruous with the increased homogeneity of the velocity profile.

The above comparison indicates that the impact of a combined turbulent flow and upstream rotor wake is not a simple case of superposition of one effect with the other. However, it is noted that, given the general decrease in velocity across the tunnel, the presence of the upstream turbine appears to have modified the development of the turbulent profile, making a true comparison difficult to achieve.

4.2.3 Meandering

A simple experiment was devised in order to determine if wake meandering was a feature of the wake profile. The two single wire probes were positioned such that they were aligned with the maximum gradient of the velocity deficit on either side of the wake at hub height. A highly negative cross-correlation coefficient derived from the resulting signals would indicate a meandering process: As the wake moves away from one probe, decreasing the deficit, it will move into the other, increasing the deficit.

The maximum gradient of the velocity deficit was identified as $0.5D$ from the wake centreline. As such, the upstream turbine was mounted at the $\Delta y = 0.5D$ position, with the hot-wires mounted on the tunnel centreline and at $\Delta y = 1D$ lateral offset in the downstream rotor plane. Measurements were recorded in both uniform and turbulent inflow.

Figure 4.11 shows the cross-correlation coefficient of the fluctuating velocity com-

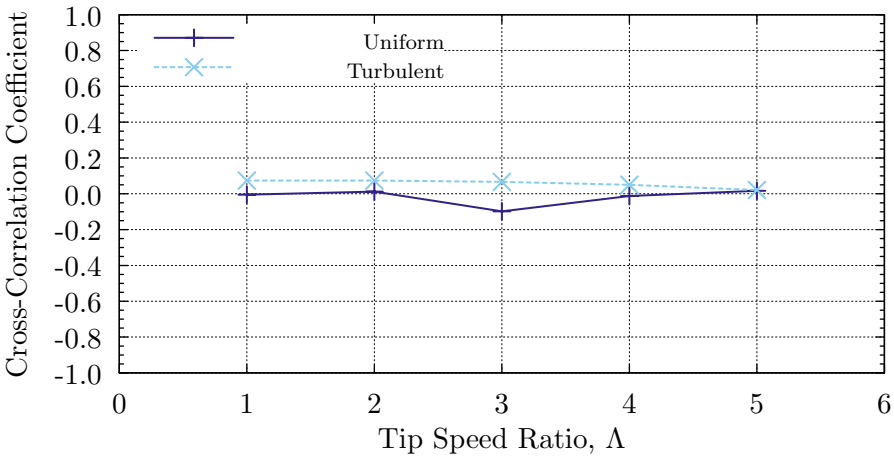


Figure 4.11: Cross-correlation of meandering wake velocities.

ponent for both uniform and turbulent inflow at each of the tip speed ratios investigated. Whilst there is a slight negative correlation at $\Lambda = 3$, the two signals are essentially uncorrelated across the board. Therefore, it is concluded that meandering of the wake is not present in the wind tunnel simulations investigated in this thesis.

A similar, but unrelated, phenomena is steady transverse displacement of the wake. This can be modelled as the effect of a mirror image wake about the floor and ceiling planes. The turbine is positioned on the tunnel centreline and hence the two image wakes should cancel resulting in zero transverse displacement. As previously indicated, although a minor degree of skew was present when the upstream rotor was positioned at $\Delta y = 1D$, there was no significant displacement present in the experiments.

4.3 Turbine experiments

The principal set of experiments define a validation database of rotor blade root bending moments and rotor thrust loads under different inflow conditions for comparison with the numerical model. The flow conditions investigated were:

1. Uniform inflow;
2. Turbulent inflow;

3. Upstream rotor wake impact.

In addition, a combined flow case for both turbulent inflow and upstream rotor wake impact was also investigated.

The out-of-plane blade root bending moment was measured using a full bridge strain gauge consisting of two Micro Measurements 125PC strain gauges positioned either side of the blade beam at $r = 0.056$ m, corresponding to the root of the blade at the connection between blade and hub. The strain gauge signal was transmitted via a Mantracourt T24-SA wireless strain gauge amplifier to a receiver module connected to the acquisition computer. The maximum sampling rate of the T24-SA is 200 Hz, chosen as the sampling rate, with a sample length of $N = 1024$ to give a spectral resolution of just under 0.2 Hz. As in the wake measurements, $n_d = 385$ sub-samples were acquired to give a statistical accuracy of $\pm 10\%$ with 95% confidence for the measured spectrum.

The rotor thrust was also measured using a full bridge strain gauge located 0.04345 m from the hub centre. However in this case, two Tokyo Sokki Kenkyujo Co. Ltd. FLA-10-11 strain gauges were used as the space constraint was removed meaning a larger gauge could be selected to simplify the application process. The thrust strain gauge signal was acquired using a Fylde FE-379-TA strain gauge amplifier. As all data was acquired simultaneously, the thrust signal was acquired at the same rates as the blade root bending moment.

Both strain gauges were calibrated according to the methods described in Appendices A.1.1 and A.1.2, for the blade root bending moment and thrust respectively, where the calibration curves can also be found.

Measurements in both 12 m s^{-1} uniform and turbulent flow, generated by the fractal grid described in Section 4.1.3, are presented in Figures 4.12-4.17 and discussed in Sections 4.3.1 and 4.3.2, respectively. The results for upstream rotor wake impacting are presented in Section 4.3.3 and the combined flow case is discussed in Section 4.3.4.

4.3.1 Uniform flow

The baseline case is a uniform inflow of 12 m s^{-1} with only the instrumented turbine mounted in the tunnel. Two sets of data were taken in order to confirm the consistency and repeatability of the results. As such, for each of the tip speed ratios presented in the following figures there are two points plotted.

In order to account for the drag on the nacelle a measurement of the thrust and bending moment was recorded in the 12 m s^{-1} flow with the turbine held stationary. The bending moment was subtracted from the thrust, assuming the force was acting at the centre of area of the blades, to give an estimate of the tare drag minus the drag of the blades, which will be operating in the rotational flow. The tare drag is then subtracted from the thrust measurements. It is noted that whilst this should give a relatively accurate estimate of the drag, when the turbine is in operation the nacelle will experience a momentum deficit and hence the drag should decrease meaning that the thrust may be sightly underestimated.

The mean thrust coefficient, C_T, presented in Figure 4.12, exhibits a linear increase between $\Lambda = 1 - 3$, but begins to diverge from this trend as the tip speed ratio increases above this range. The maximum value, at $\Lambda = 5$, is $C_T = 0.40$. The variance in the data points is less than 2%, except for $\Lambda = 1$ where there is 6% difference, indicating a high level of repeatability between the two runs. The increased variance at $\Lambda = 1$ is indicative of the blade stalling, as well as a consequence of the low thrust at this speed.

The thrust Root-Mean-Squared (RMS) intensity, normalised by the mean, is presented in Figure 4.13. The intensity decreases with increasing tip speed ratio, from an average peak value of 0.62 at $\Lambda = 1$ to a minimum of less than 0.18 between $\Lambda = 3 - 5$, a result of rotational stiffening of the blade along with attached flow conditions. Congruently, the variance in the RMS is highest for $\Lambda = 1 - 2$, with an increase in intensity of approximately 70% at $\Lambda = 2$, and lower at the higher tips speeds. The blade passing frequency at the lower tip speeds fall either side of the strut resonant frequency $f_s = 9.6$ Hz at $f_1 = 7.6$ Hz and $f_2 = 15.3$ Hz. Damping of

the strut resonance will increase the bandwidth of the resonant response, and may explain some of the increased intensity and variance between runs, in combination with stall of the blades at low tip speed ratios.

The mean blade root bending moment coefficient, shown in Figure 4.14, follows a similar trend to the mean thrust coefficient. The maximum value is $C_{M_b} = 0.052$ at $\Lambda = 5$. Yang et al. (2011) attribute the behaviour at low Λ to stall and at high Λ to small angles of attack and corresponding reduction in lift. There is also a much higher degree of variance between the two runs, $10 - 20\%$, across all tip speed ratios. The bending moment RMS intensity is presented in Figure 4.15. Again, the trends are similar to the thrust loading, although the amplitude is around one fifth.

The disparity between runs for the bending moment coefficient is most likely due to a difference in the incident velocity seen by the turbine. However, given the agreement between the thrust loads, it is unlikely that this is a consequence of a global change in the free stream velocity. Rather, a small degree of yaw in the initial run could be responsible for reducing the local velocity such that the mean velocity is reduced. The alignment of the turbine was checked between runs allowing for correction of any yaw offset before the second set. Another theory, which is not entirely unlikely, is that the blade profile suffered some degree of torsional creep due to a slight thermal instability in the Digital ABS material. Given the geometry of the blade, this is most likely to have increased the local incidence and hence loading on the blade. Whilst an attempt was made to confirm that no deformation had occurred, it is not possible to be entirely certain due to the complex geometry.

The thrust and blade root bending moment PSD spectra are presented in Figures 4.16 and 4.17, respectively. For clarity, only the results from the second run are plotted, but it is noted that the peaks occur for the same frequencies in both sets of data with some differences in magnitude. Most notably the baseline level is slightly higher in the second set of runs. This is most likely due to deterioration of the blades between runs; this was particularly evident in the form of fraying of the trailing edge although still relatively minor. Deterioration of the blades would lead to greater noise and an increase in the baseline level of the spectrum. The strut,

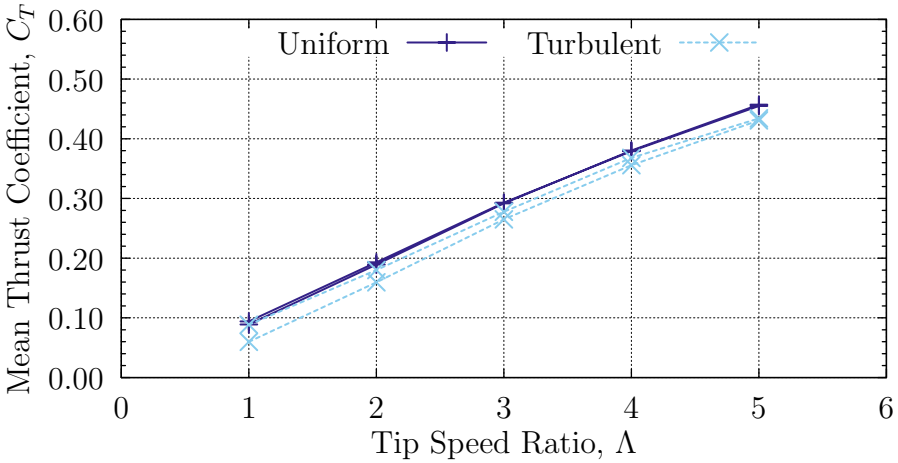


Figure 4.12: Comparison between turbulent and uniform flow thrust coefficients.

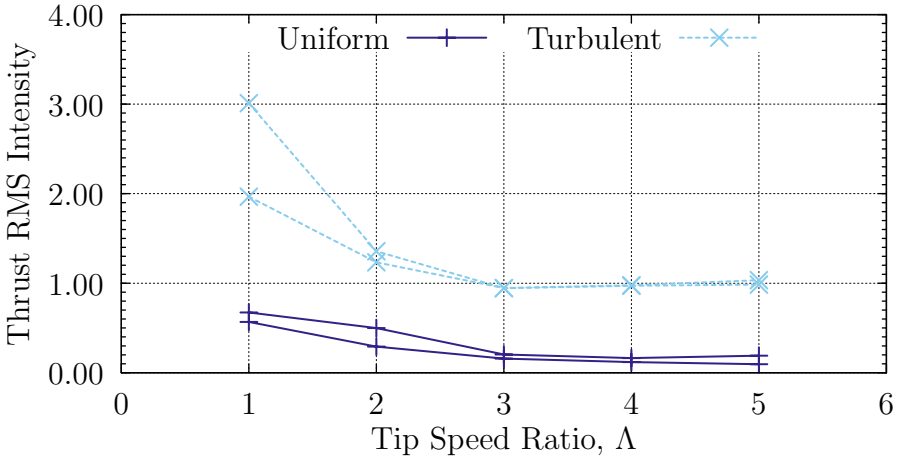


Figure 4.13: Comparison between turbulent and uniform flow thrust moment RMS intensity.

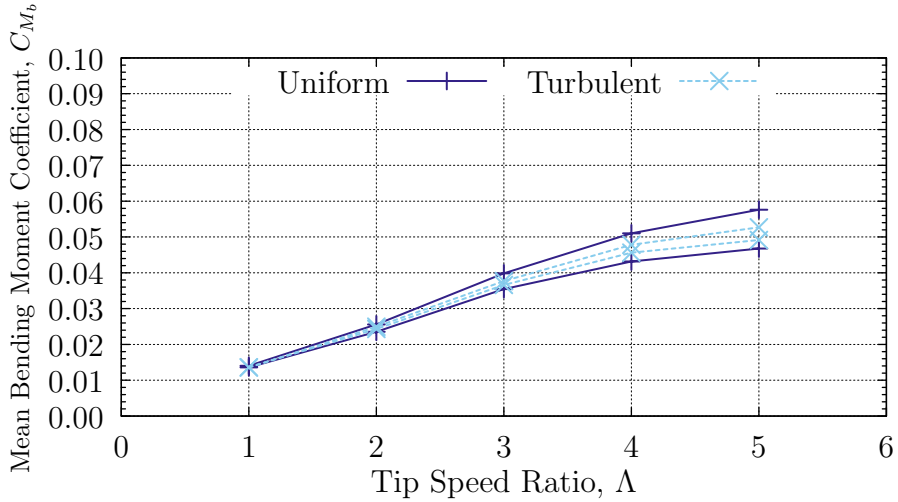


Figure 4.14: Comparison between turbulent and uniform flow blade root bending moment coefficients.

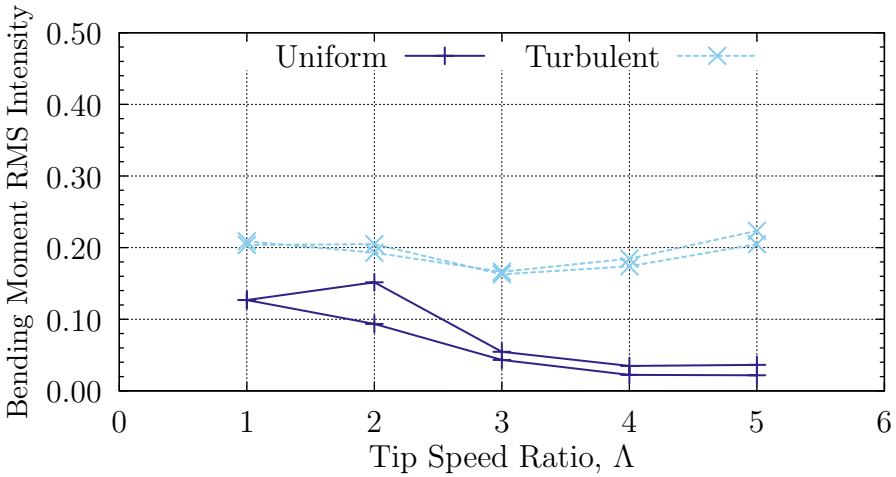


Figure 4.15: Comparison between turbulent and uniform flow blade root bending moment RMS intensity.

$f_s = 9.6$ Hz, and blade, $f_b = 85.4$ Hz, resonant frequencies are also indicated in both figures, as well as the grid frequency, $f_g = 50.0$ Hz, in the thrust spectra.

The background (12 m s^{-1} flow with the rotor held stationary) thrust loading spectrum is flat with peaks at each of the aforementioned frequencies, dominated by the peak at the strut resonance, which is several orders of magnitude higher. Similarly, the bending moment background spectrum also exhibits peaks at the two resonant frequencies, but not the grid frequency. The latter spectrum also tails off at high frequency, congruent with the lower noise to signal ratio when compared with the thrust loading. Finally, the bending moment background spectrum is dominated by a peak at approximately 56 Hz, also present in the spectrum at 0 m s^{-1} with the rotor stationary but vanishes when the tunnel is switched off, indicating that this is a result of background noise in the wind tunnel environment, which is being picked up by the antenna of the wireless telemetry system, and can be discounted in the following discussion.

The rotational spectra are dominated by harmonics of the rotational frequency, an observation also made by Yang et al. (2011) in their wind tunnel experiments, and as such have been plotted against frequency normalised by the rotor frequency to simplify identification of the peaks. Whilst both the grid and strut resonant frequencies are present in all the thrust spectra, the blade resonant frequency only appears in the odd numbered tip speed ratios and is particularly significant at $\Lambda = 5$.

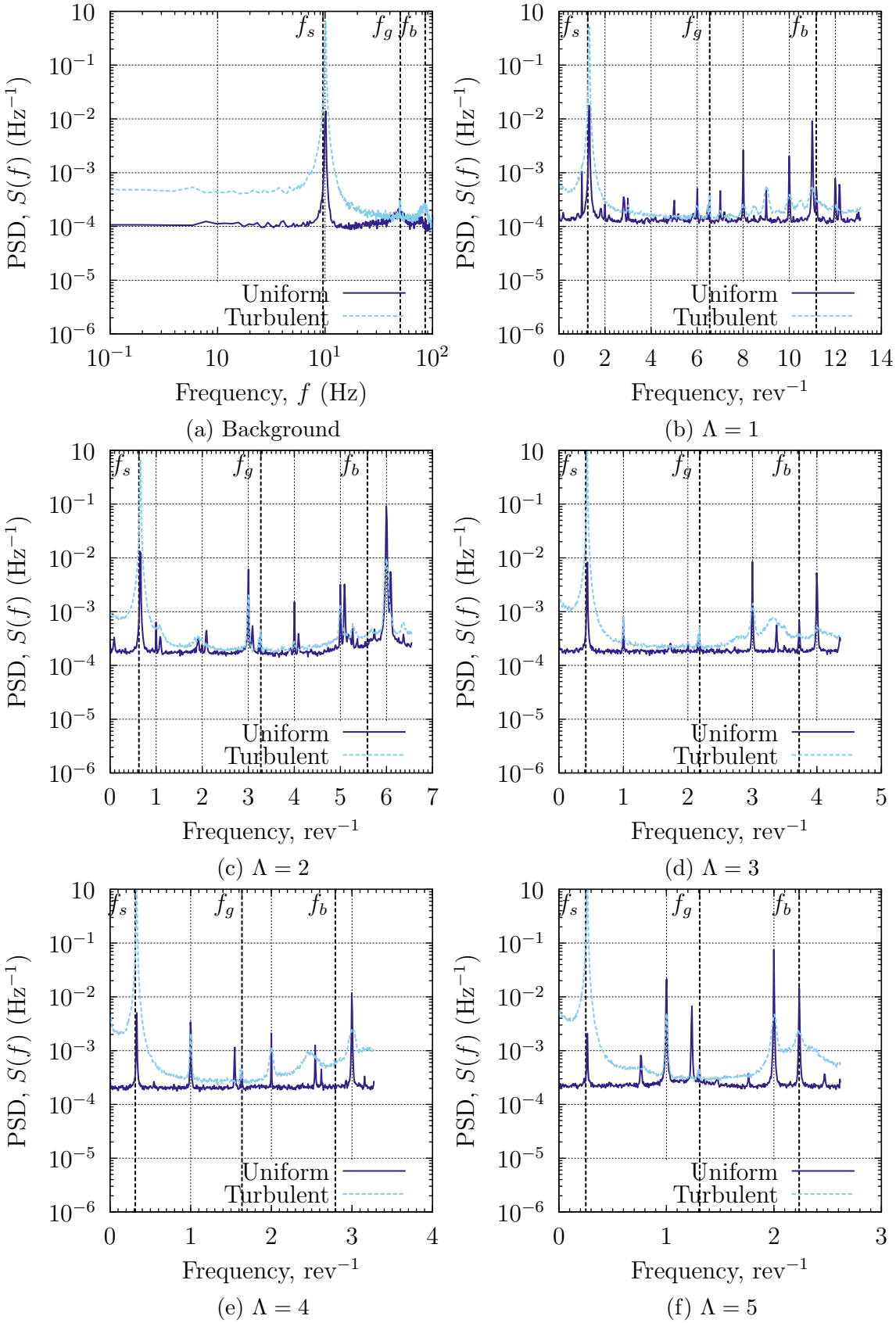


Figure 4.16: Comparison between turbulent and uniform flow spectra from the thrust loading. Spectra are plotted in multiples of the rotational frequency, with the exception of the background, which is plotted in Hz. Strut, f_s, and blade, f_b, resonance and grid, f_g, frequencies are marked by vertical strokes.

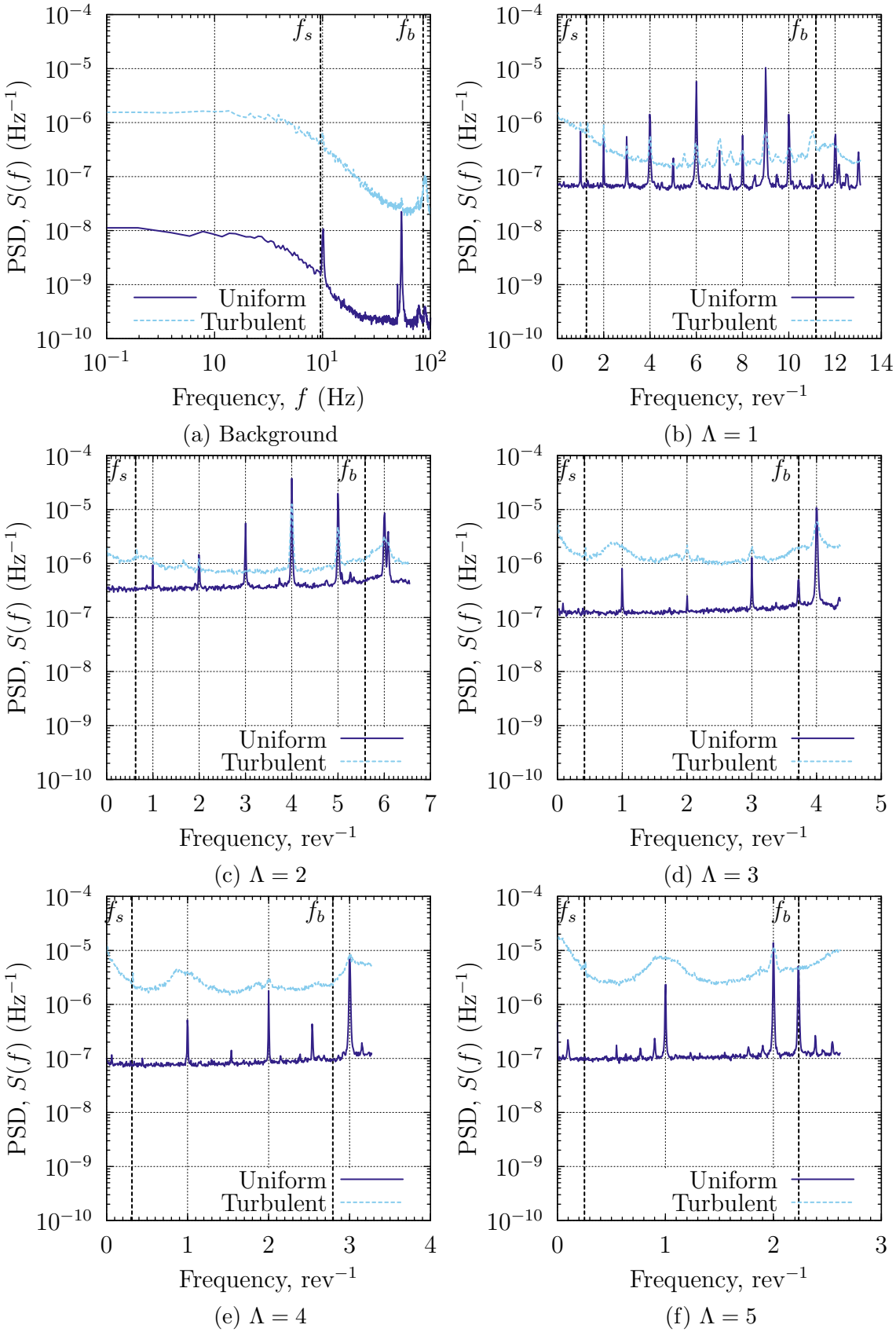


Figure 4.17: Comparison between turbulent and uniform flow spectra from the blade root bending moment. Spectra are plotted in multiples of the rotational frequency, with the exception of the background, which is plotted in Hz. Strut, f_s, and blade, f_b, resonant frequencies are marked by vertical strokes.

Furthermore, the blade resonant frequency is only present at $\Lambda = 3$ and 5 in the bending moment spectra. Conversely, the strut resonant frequency is not present in any of the bending moment spectra. As already mentioned, the angle of attack of the blade, and consequently the aerodynamic damping, will be significantly reduced at higher Λ hence the vibration is increased, although the effect may be offset by rotational stiffening. The harmonics of the rotation frequency can be explained in several ways. Passage of the blade through the tower shadow would produce a peak at $3P$ in the thrust spectra and $1P$ in the bending moment spectra. Higher harmonics are also present due to the non-sinusoidal nature of the tower shadow response. Similarly, imbalances in the rotor disc, slight variations in the weight or geometry due to manufacturing defects, or slight variations in the incident velocity across the rotor will also produce the $1P$ peak and higher harmonics.

Excluding the per revolution, resonant and grid frequencies, the remaining peaks of significance in the thrust spectra are located at approximately 30 Hz ($0.77P$ in Fig. 4.16f), 46 Hz ($1.23P$ in Fig. 4.16f & $1.5P$ in Fig. 4.16e), and 78 Hz ($2.55P$ in Fig. 4.16e & $3.4P$ in Fig. 4.16d). Of these, only the latter is visible in bending moment spectra with no additional significant peaks. Therefore, it seems reasonable to assume that the 78 Hz peak is related to the blade response, whilst the other two are strut frequencies. Of these, the first, at 30 Hz, corresponds to approximately three times the strut resonance and hence could be associated with $3P$ excitation of the strut resonance. The cause of the remaining two peaks has not been identified. However, it is noted that in all cases, these peaks are at least an order of magnitude lower than the dominant peaks in the spectrum and are therefore likely to have a minimal effect.

4.3.2 Turbulent flow

The uniform flow results discussed in the previous section have been compared with similar measurements in turbulent flow, generated using the fractal grid described in Section 4.1.3.

The mean thrust and bending moment coefficients in turbulent inflow follow the same trends as the uniform case with similar magnitudes, shown in Figures 4.12 and 4.14, respectively. This is expected as the mean velocities are similar in both cases. The thrust coefficient results show a slight reduction in the thrust and increased variance with decreasing tip speed ratio. Conversely, the bending moment coefficient results have reduced variance and fall between the uniform flow results for the two runs, possibly supporting the yawed inflow theory for the disparity in the uniform flow results: the spatial variance of turbulent inflow could reduce the deviation of velocity around the azimuth and hence the difference in loading.

The key difference between the two flow cases is indicated by the RMS intensity plots in Figures 4.13 and 4.15 for the thrust and bending moment, respectively. Both exhibit an increased intensity at all tip speed ratios, although the trends for the incident turbulence case are similar to the uniform case and exhibit a degree of scaling of the RMS intensity with the background levels of turbulence. The implication of this being that the increased RMS intensity is largely due to the increased turbulence intensity, in agreement with the observations of Hassan et al. (1988).

The difference between the uniform and turbulent spectra, Figures 4.16 for the thrust and 4.17 for the bending moment, can be characterised by two distinct observations: spreading and attenuation of the majority of the peaks and increased baseline level. The former is due to the nature of turbulence: the azimuthal position of eddies which excite the per revolution frequencies will vary with time resulting in a spread of the excitation frequency and reduction in the peak power. The latter obscures a large number of the peaks identified in the uniform flow case, although notably the strut resonance peak is several orders of magnitude higher in the thrust spectra. The turbulence intensity will result in greater excitation of the strut resonance and corresponding increase of the power in the spectrum. Consequently, the strut resonance is also likely to dominate the RMS response of the thrust in the turbulent flow case. Consistently with the observations of the RMS intensity, the baseline level appears to be scaled up from the uniform flow case across all frequencies. Finally,

there are no additional peaks in any of the spectra with the exception of the strut resonance in the bending moment spectra, although the magnitude of the peak is relatively minor.

4.3.3 Upstream rotor wake

The uniform flow results were also compared with measurements in the wake of an upstream rotor with uniform inflow. The upstream rotor wake generator was positioned either axially aligned with the instrumented rotor or laterally offset by $\Delta y = 0.25 - 1.00D$ in $0.25D$ increments. Both rotors were set to the same rotational velocity giving a nominal tip speed ratio as normalised against the freestream or reference velocity.

The mean thrust coefficient, Figure 4.18, shows a clear impact of the upstream rotor wake, collapsing together as the tip speed ratio decreases. The most significant reduction in thrust is around 50% for the axially aligned case, which is caused by the reduced inflow velocity, but by $\Delta y = 0.75D$ offset of the upstream rotor the uniform flow response is mostly recovered. The other two cases fall between the two extremes, moving towards the uniform flow case with increased lateral offset as the mean flow velocity is recovered. The bending moment coefficient, Figure 4.19, exhibits a similar response, although the reduction in bending moments are more uniformly spaced.

The thrust and bending moment RMS intensities are plotted in Figures 4.20 and 4.21, respectively. The thrust RMS intensities under wake impact are relatively similar for all lateral offsets, with the exception of the peak at $\Lambda = 1$. In the latter case, the peak is a maximum for the $\Delta y = 0.25D$ offset case, decreasing with increased lateral offset, and the aligned case exhibits the minimum increase over the uniform flow case. The thrust represents an integrated loading over the entire rotor disc; therefore, the variation in RMS with lateral offset is likely to be reduced since part of the rotor will be operating in the undisturbed free flow. Conversely, in the aligned configuration, there is a general increase in turbulence intensity, which

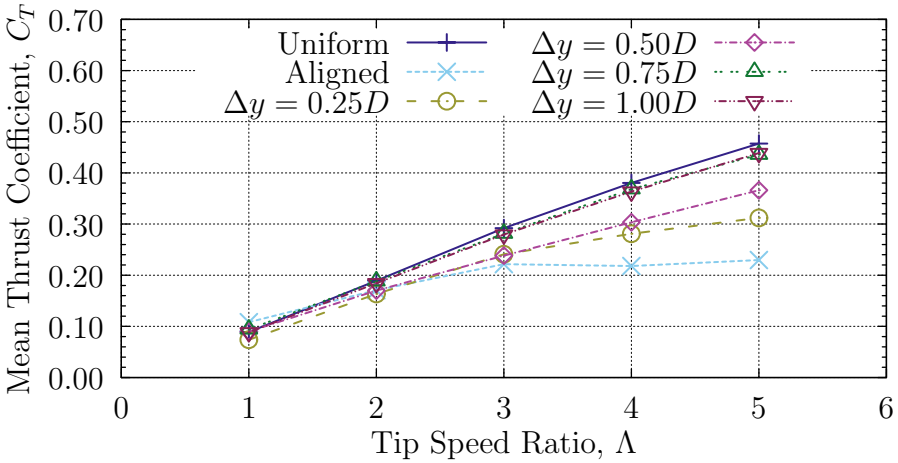


Figure 4.18: Comparison between thrust coefficients for different upstream rotor lateral offsets.

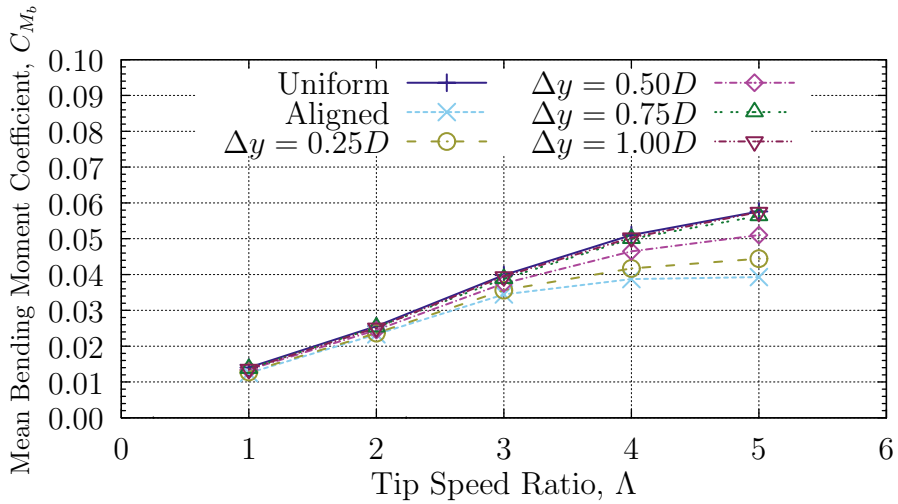


Figure 4.19: Comparison between blade root bending moment coefficients for different upstream rotor lateral offsets.

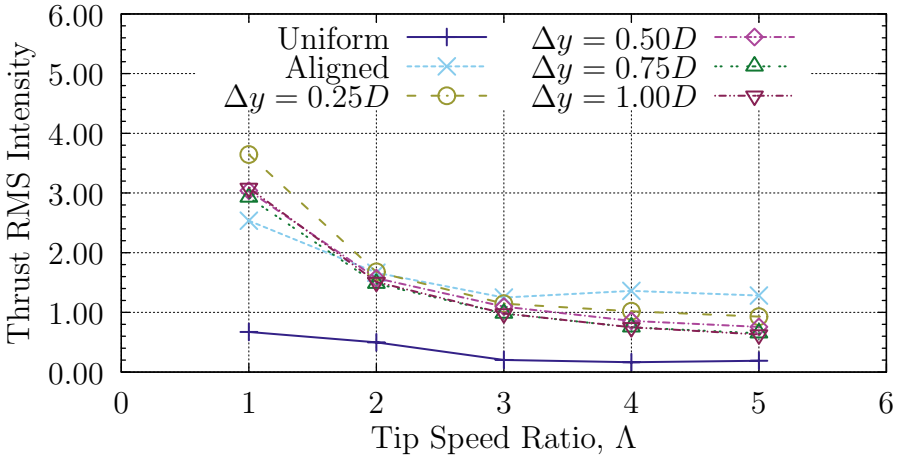


Figure 4.20: Comparison between thrust moment RMS intensity for different upstream rotor lateral offsets.

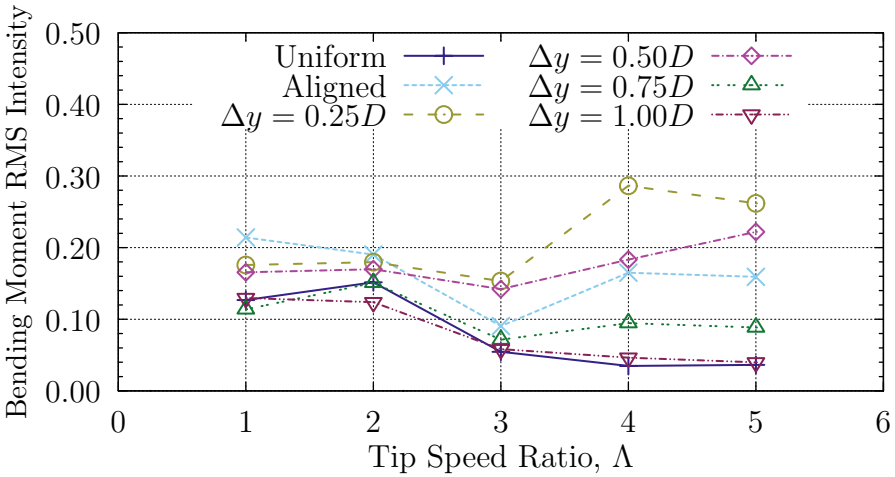


Figure 4.21: Comparison between blade root bending moment RMS intensity for different upstream rotor lateral offsets.

explains the slightly higher intensities in this case.

The bending moment intensities exhibit a greater influence from the upstream rotor wake lateral offset, which is consistent with observations of the mean bending moment coefficient. Once again the $\Delta y = 0.25D$ lateral offset exhibits the highest intensities, with the exception of $\Lambda = 1$ where the aligned case has the highest peak. As the lateral offset is increased the intensity reduces towards the uniform flow case, which is mostly recovered by $\Delta y = 0.75D$ lateral offset and fully recovered by $\Delta y = 1.00D$ lateral offset. This trend is a result of the combination of the wake turbulence and mean velocity deficit. In the aligned case, the RMS intensity is governed by the wake turbulence alone, as the mean velocity deficit is approximately axisymmetric. When the rotor is offset the mean velocity deficit adds to the RMS intensity, but the influence of both effects decreases with increased lateral offset.

The normalised thrust and bending moment PSD spectra are plotted in Figures 4.22 and 4.23, respectively. Much like the turbulent flow case, the spectra for the upstream rotor wake impacting exhibit no new peaks and the majority are suppressed as the baseline level increases. Similarly, the baseline level appears to be scaled from the uniform flow case, indicating that the increased intensity may be the dominating factor. Unlike the ambient turbulence, the peaks do not appear to be more spread out. This may be a result of the reduced length scale of the wake turbulence, less than half the ambient length scale, meaning that the reduced correlation of the

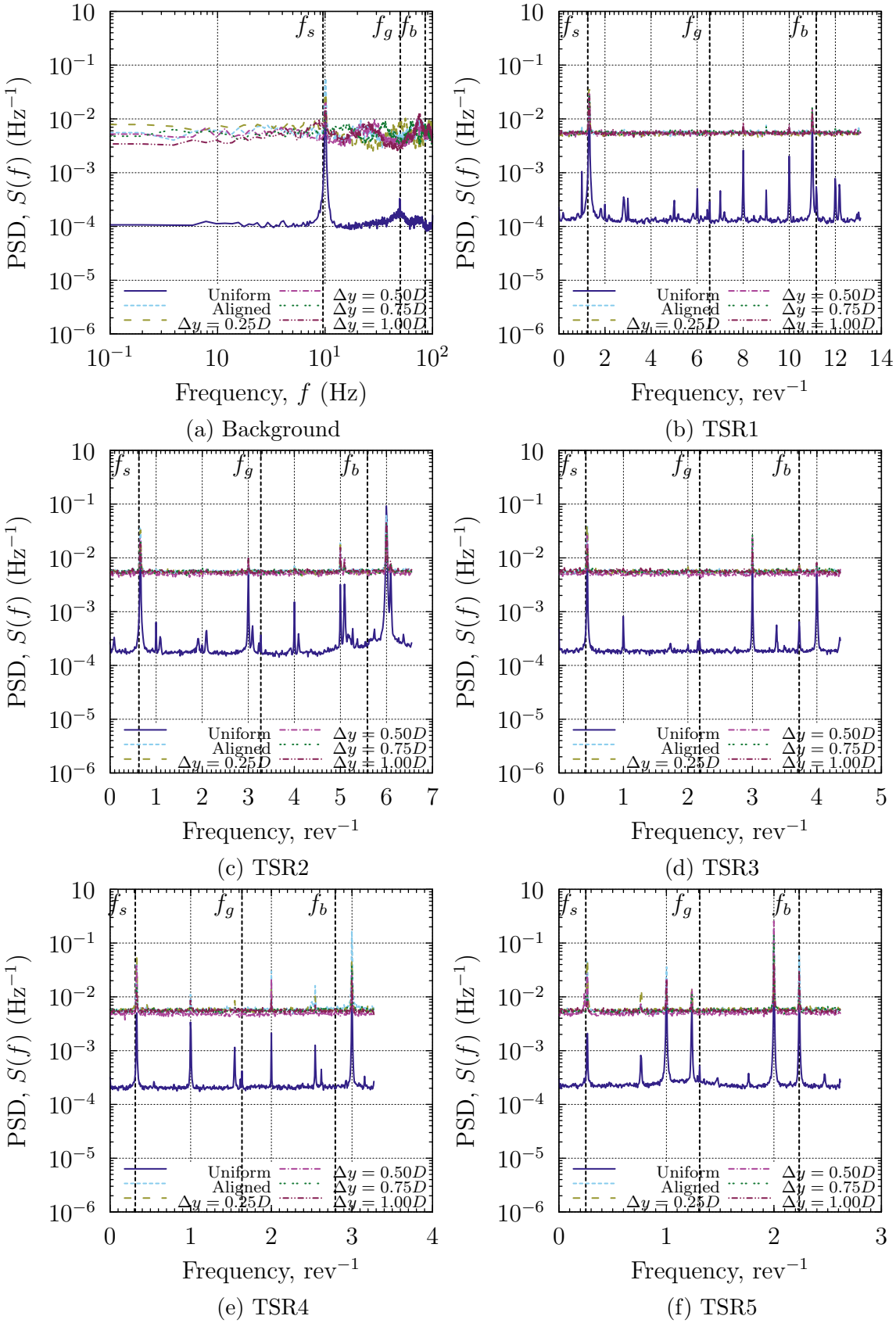


Figure 4.22: Comparison between spectra for different upstream rotor lateral offsets from the thrust loading. Spectra are plotted in multiples of the rotational frequency, with the exception of the background, which is plotted in Hz. Strut, f_s, and blade, f_b, resonance and grid, f_g, frequencies are marked by vertical strokes.

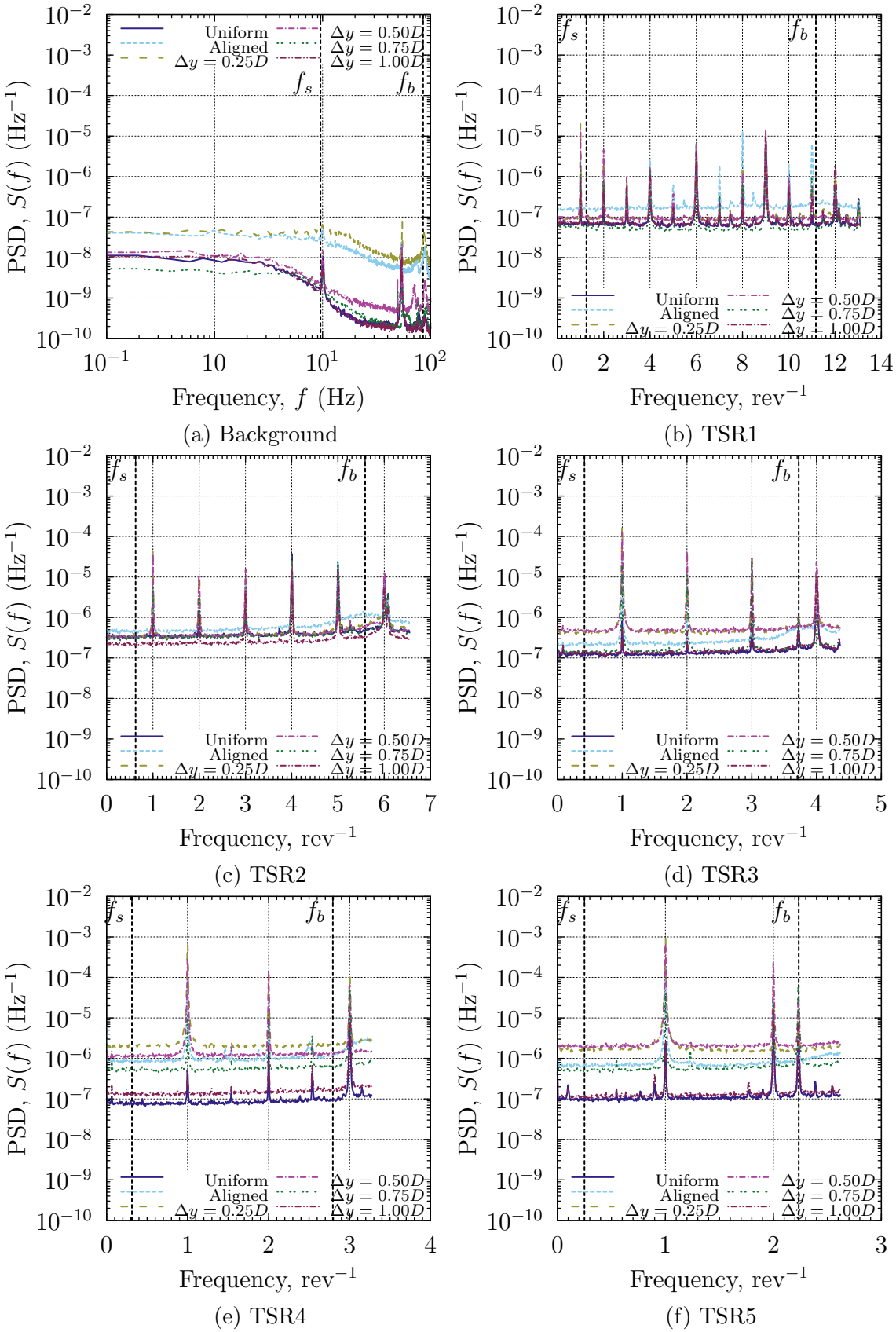


Figure 4.23: Comparison between spectra for different upstream rotor lateral offsets from the blade root bending moment. Spectra are plotted in multiples of the rotational frequency, with the exception of the background, which is plotted in Hz. Strut, f_s, and blade, f_b, resonant frequencies are marked by vertical strokes.

turbulence over the rotor plane reduces the response.

The thrust spectra exhibit the same increase in the baseline level for all lateral offsets, with little difference between the peaks in each case. Contrarily, the bending moment spectra exhibit differing baseline levels. Both comparisons are congruent with the observations of the RMS intensity. The $\Delta y = 1.00D$ lateral offset and instrumented spectra are both similar, as well as the $\Delta y = 0.75D$ lateral offset case for $\Lambda \leq 3$. Similarly, the $\Delta y = 0.25D$ and $0.50D$ lateral offset spectra show good agreement, and also exhibit the highest baseline level for $\Lambda \geq 3$. At lower tip speeds, the aligned case exhibits the highest baseline level and at higher tip speed ratios the $0.75D$ case is most similar to the aligned with both falling between the other spectra.

4.3.4 Combined

Finally, the two turbulent flow cases, ambient and upstream rotor wake turbulence, are compared with measurements taken in a combined flow. As discussed previously, only the axially aligned upstream rotor wake case is considered due to the geometry of the fractal grid. It is also noted that the upstream rotor will experience significantly different incident turbulence to the instrumented rotor: the wakes of the fractal grid elements are likely still to be mixing giving a highly inhomogeneous flow with significantly increased intensity and reduced length scale.

Figure 4.24 shows a comparison of the combined aligned upstream rotor wake and turbulent flow case with the individual flow cases results for the thrust and bending moment coefficients, intensities and spectra at a tip speed ratio of $\Lambda = 3$.

The mean thrust coefficient does not indicate any clear trend; the combined case appears as a combination of the individual responses, showing some dominance of the ambient turbulence at low tip speeds. Conversely, the mean bending moment coefficient is clearly dominated by the wake impact, with only a slight increase due to the turbulent response.

The RMS intensity doesn't appear to offer much additional insight, with the excep-

tion of a non-linear increase in the combined case over the two individual cases. The spectra clearly indicate that the higher energy case dominates the combined flow. For the thrust spectra this results in an near identical spectrum to the wake case with increased response at the strut resonant frequency and slight attenuation of the other peaks. Conversely, for the bending moment the combined case spectrum is closest to the turbulent case, with a slight reduction in the baseline level, and the $1P$ peak of the wake case showing through.

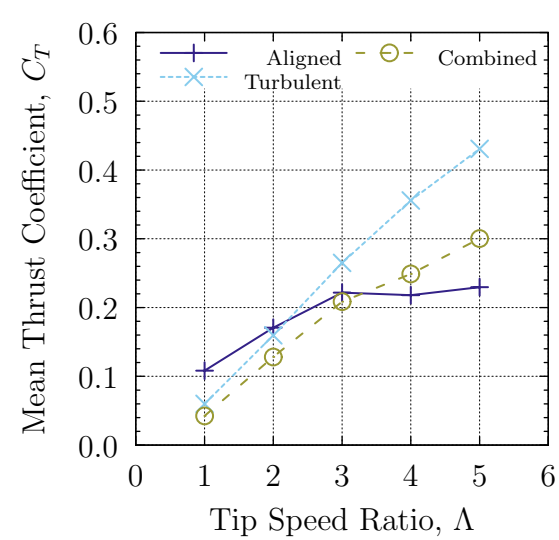
In conclusion, whilst the combined thrust coefficient response is unclear, possibly dominated by the wake flow, the mean bending moment is clearly dominated by the wake, whilst the dynamic response is dominated by the ambient flow. It should be noted that as this case corresponds to the axially aligned upstream rotor, the picture may be different for the laterally offset cases due to stronger $1P$ excitation.

4.4 Summary

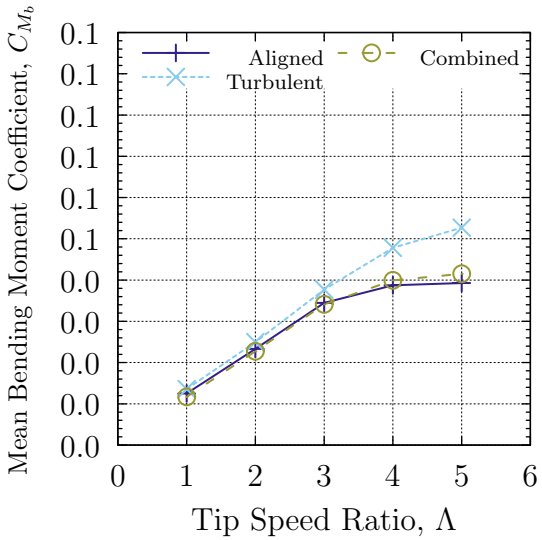
Both measurements of the upstream rotor wake profiles and downstream turbine loads have been presented. The upstream rotor wake can be approximated by a Gaussian profile with increasing centreline deficit with tip speed ratio. The turbulence intensity and length scale are approximately constant across the wake width, and do not vary greatly with tip speed ratio. Finally, the wake demonstrates expansion of $20 - 40\%$, which is also independent of tip speed ratio.

The effect of this wake on the downstream rotor loads is to increase the baseline level of the spectra and RMS intensities, but reduce the mean loading. Similarly, ambient turbulence is also found to increase the spectral baseline and RMS intensities, but does not effect the mean loads. In addition, peaks unobscured by the increase in the baseline level of the spectra are attenuated and spread by the turbulence.

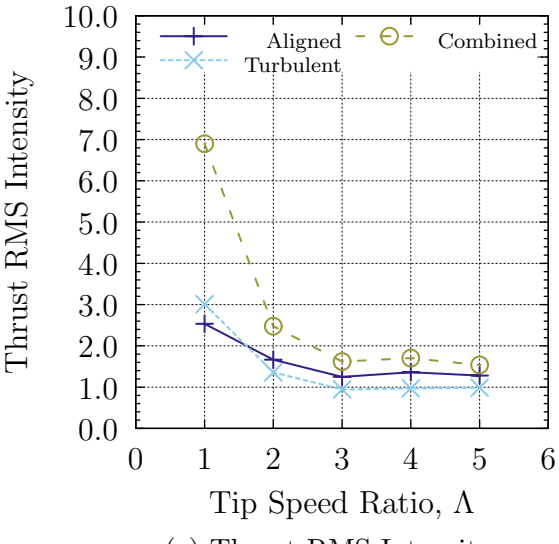
Issues with the turbulence grid geometry prevent an accurate assessment of the combined effect, but appear to indicate that the dynamic response is dominated by the highest energy in the spectrum. The impact on the mean loading is less clear.



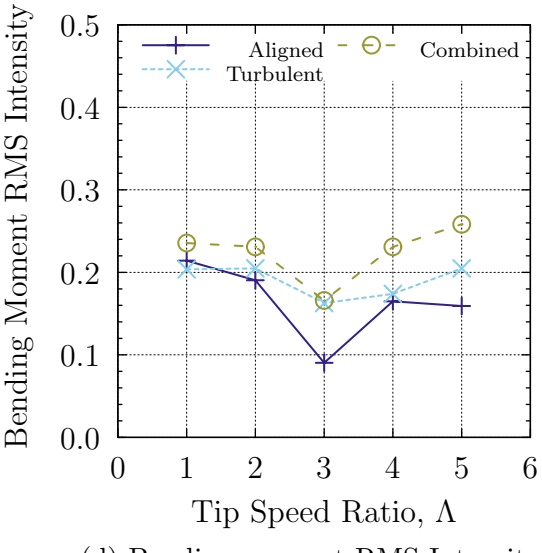
(a) Thrust coefficient.



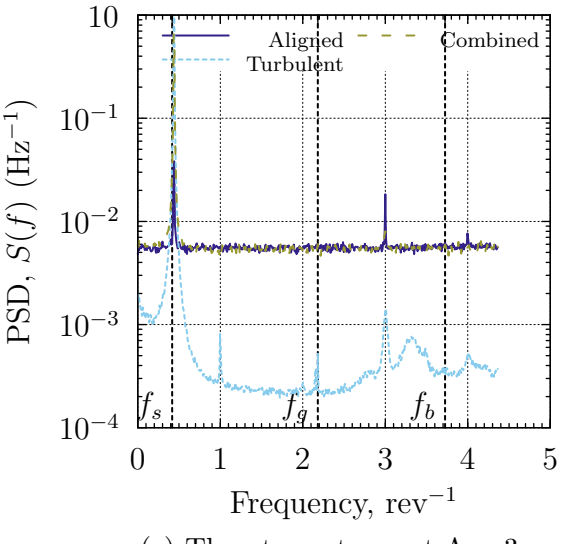
(b) Bending moment coefficient.



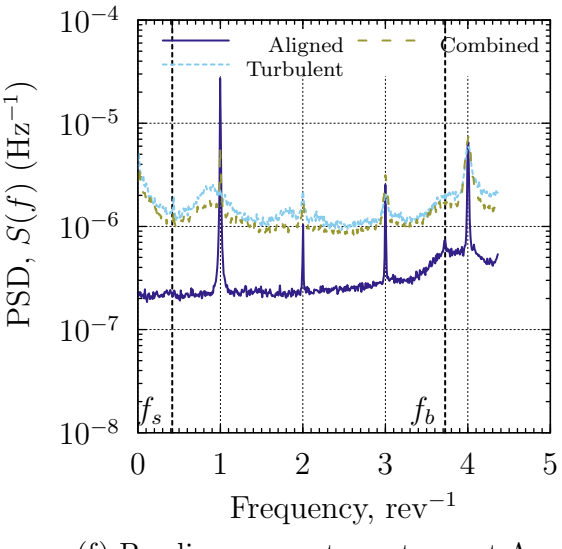
(c) Thrust RMS Intensity.



(d) Bending moment RMS Intensity.



(e) Thrust spectrum at $\Lambda = 3$.



(f) Bending moment spectrum at $\Lambda = 3$.

Figure 4.24: Comparison of combined ambient and wake turbulence with individual cases.

5 Ambient turbulence and wake impact: Modelling and discussion

The two main types of stochastic loading pertinent to wind turbines in large offshore arrays are ambient turbulence and upstream rotor wake impact. The effects of these loads are important in terms of the fatigue loading on the rotor and may impact on rotor life and maintenance costs. Upstream rotor wake impact consists of two components: a deterministic loading due to the blades passing into and out of the upstream rotor wake and a stochastic loading due to the added turbulence associated with the upstream rotor wake. In this chapter the developed model is validated against the experimental measurements and used to investigate the effects of these two types of loading: the effects of ambient turbulence are discussed in Section 5.2 and upstream rotor wake impact in Section 5.3. The discussion is preceded by validation of the developed model using the simplest case of uniform inflow, presented in Section 5.1.

The blade in the numerical simulations is discretised by $n_x = n_y = 10$ giving 9×9 panels, as recommended by the convergence studies in Section 3.8. In order to compare with the experimental measurements a maximum time step of 0.005 s is required, corresponding to a sampling rate of 200 Hz. However, due to the small geometric scale of the experiments, and associated high angular velocities in order to maintain the tip speed ratios, Λ, this is insufficient to resolve the wake geometry at high Λ properly. Therefore, the simulations are oversampled at a time step of 0.0025 s, corresponding to a sampling rate of 400 Hz, giving a non-dimensionalised time step of $0.019 - 0.095$ across the range of tip speed ratios. Finally, the simulations are run for $t = 600$ increments, corresponding to $\tau = 11.5 - 57$ blade revolutions, and giving a $\Delta f = 1$ Hz resolution for the presented spectra. Both time step parameters are also in agreement with the recommendations of the convergence studies.

5.1 Uniform flow

Further to the verifications of both the wing and rotor cases in Section 3.9, in order to validate the developed vortex lattice method code, Aeolus, in the rotor case the mean loading is compared with the experimental measurements for a simple uniform inflow. Comparisons of both the mean thrust and bending moment coefficients are shown in Figures 5.1 and 5.2, respectively. The trends of both sets of data are in reasonable agreement. However, there is a mean offset between the numerical predictions and experimental measurements: $165\% - 34\%$ for the thrust coefficient and $114\% - 60\%$ for the bending moment coefficient, inversely proportional to the tip speed ratio.

Notable omissions from the numerical modelling include: the effects of viscosity, such as profile drag, stall and reduction in lift; structural loads, such as gravitational or centripetal forces; tower shadow; 3D features associated with the hub, which is not modelled in Aeolus. Of these the most significant is likely to be the first, viscous effects, and in particular the loss of lift associated with a reduced Reynolds number, but the centripetal loading may also be appreciable. The rotor plane is 0.105 m upstream of the support strut, which has a diameter of 0.034 m, meaning that the influence of the 'tower' should be negligible. Similarly, the effect of the hub is also assumed negligible as it will be most significant at the root of the blade, which the thrust and bending moment are least sensitive to.

The centripetal force, F_c, corresponds to the planar component of the tension, F_t, in the blade. Therefore it can be used to calculate the tension in the blade and hence the effect of the blade mass on both the thrust and blade root bending moment. The centripetal force is given by Newton's second law of motion as

$$F_c = m\Omega \times (\Omega \times \mathbf{r})$$

where $m = 0.029$ kg is the blade mass and $\mathbf{r} = [0.53 \times 10^{-3},\ 0.11,\ 0.22 \times 10^{-3}]$ m is the distance to the centre of gravity of the blade, determined from the 3D CAD model. The resulting tension in the blade is given by $\mathbf{F}_t = F_c \left(\cos\theta\right)^{-1}$ and acts along the vector from the centre of gravity to the pivot point of the blade. The

result is that the measured thrust is reduced by $0.1\% - 1.2\%$ and the blade root bending moment increased by $0.1\% - 0.4\%$, increasing with the tip speed ratio.

As the thrust loading on the rotor increases the blade will start to cone downstream. Idealising the blade as a cantilever beam with sectional properties derived from the aluminium reinforcement rod along the blade pitch axis and applying the thrust force at the free end, corresponding to $0.7R$, gives a maximum of 1° deflection about the point of the blade at $\Lambda = 5$. Modifying the centre of gravity to account for the deflection increases the reduction in thrust to $0.9\% - 7.1\%$ and the increase in bending moment to $0.4\% - 2\%$. Although, the reduction in the measured thrust is appreciable, it is not large enough to account for the difference between the predicted and measured values. Therefore, the reduction of lift at low Reynolds number must be significant if the predictions are to match the measurements.

In order to correct for low Reynolds number effects, the associated reduction in the lift curve slope needs to be taken into account. The time averaged sectional thrust is proportional to the sectional lift, neglecting drag. Referring to Figure 3.5 in Section 3.7:

$$C_t \approx \frac{C_l \lambda}{\sqrt{1+\lambda^2}}$$

where $\lambda = \Lambda r/R$ is the local speed ratio. Therefore, an approximate correction for the change in the lift curve slope at low Reynolds number can be applied by multiplying the predicted sectional thrust by the ratio of the correct lift curve slope to the thin aerofoil slope, which is taken as 2π. In order to apply such a correction suitable aerofoil data must first be identified.

To the knowledge of this author, there is no published data on any of the Delft University aerofoil sections used at Reynolds numbers in the range of the experiments ($\mathrm{Re} \approx 2$ to 6×10^4). However, Packard (2012) presents measurements of the lift of a NACA 643618 aerofoil for incidences of $\theta = -1^\circ$ to 20° at $\mathrm{Re} = 6.4 \times 10^4$, shown in Figure 5.3 (reproduced from Packard (2012), Figure 13(a)). These results are consistent with similar measurements by Mack et al. (2008) on a slightly modified NACA 643618 aerofoil at $\mathrm{Re} = 6.42 \times 10^4$, also shown in Figure 5.3 (reproduced from Mack et al. (2008), Figure 14). Both sets of data identify a region of laminar

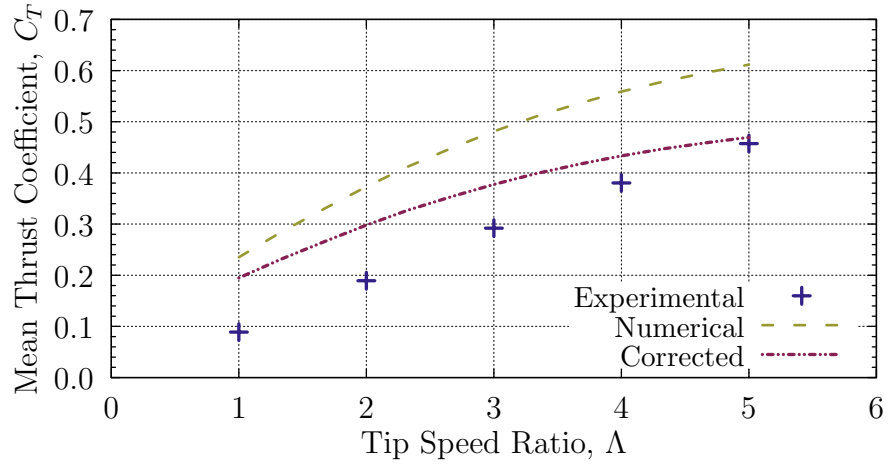


Figure 5.1: Comparison between simulation and experimental thrust coefficient.

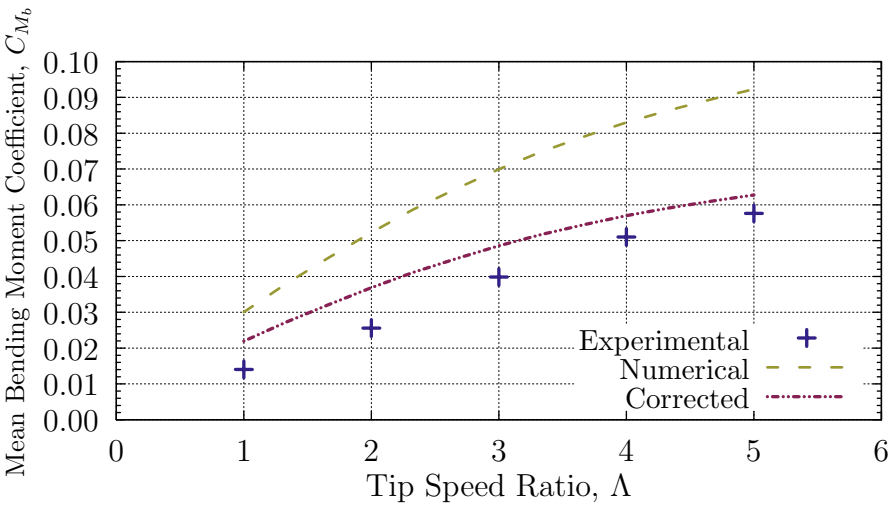


Figure 5.2: Comparison between simulation and experimental blade root bending moment coefficient.

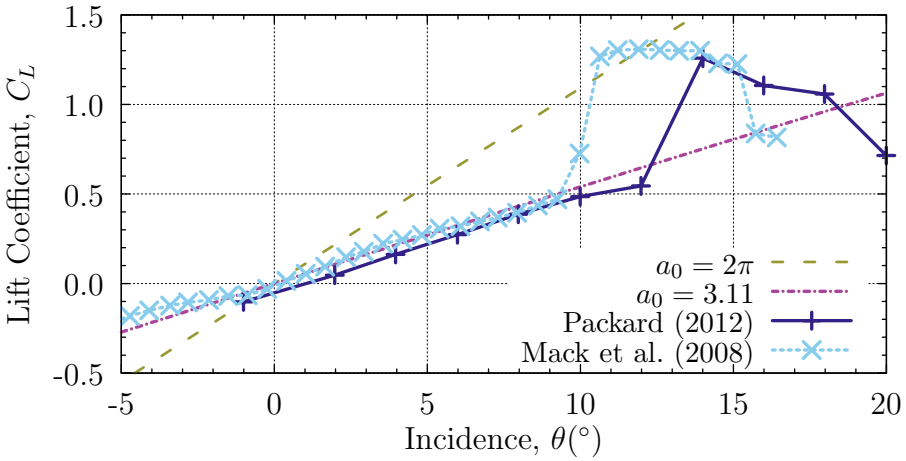


Figure 5.3: NACA 643618 Lift curve reproduced from Packard (2012) and Mack et al. (2008) with thin aerofoil theory and modified lift curve slope results. ($\mathrm{Re} = 6.4 \times 10^4$).

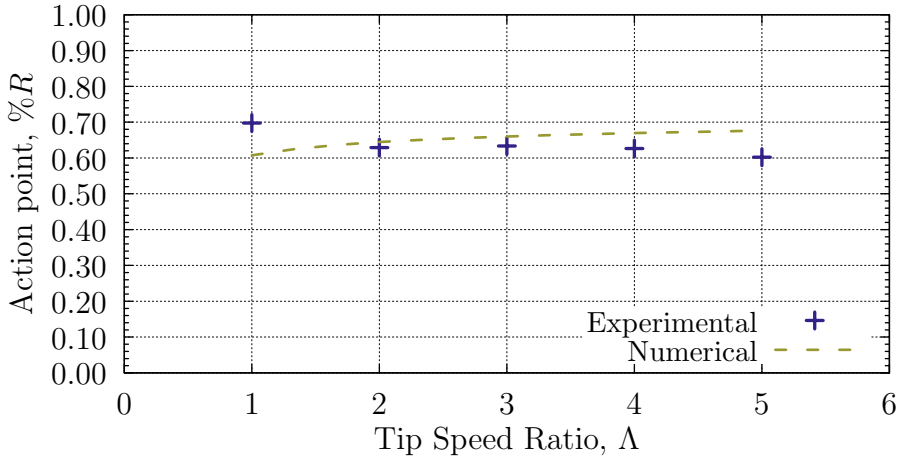


Figure 5.4: Comparison between simulation and experimental location of equivalent load point.

separation at small incidences with a lift curve slope of approximately $a_0 = 3.11$ rad^{-1}, almost half the thin aerofoil value, but identify slightly different incidences for reattachment and stall of the aerofoil section.

The NACA 643618 aerofoil constitutes the outer third of the blade and will therefore have the most significant influence on both the thrust and bending moment: The equivalent load point of the thrust

$$\frac{r_{M_b}}{R} = \frac{n_b C_{M_b}}{C_T} + \frac{r_{hub}}{R}$$

is shown in Figure 5.4 and is between $0.6R$ and $0.7R$ in most cases. The numerical model predicts a similar position for the load point, but the opposite trend: a slight outboard shift with increasing tip speed ratio as opposed to the inboard shift seen in the measurements. The trend in the measurements is a result of decreased stall for increased tip speeds: as the incidence of the root sections decreases the sections recover from stall to attached flow and increase the loading generated inboard. As a stall has not been incorporated into the present model this behaviour is not reproduced, but the variation in position is not significant.

The lift curve slope of Packard (2012) has been used to correct the predicted loads in Aeolus: as the loads are integrated over the blade the panels corresponding to the NACA 643618 aerofoil are scaled according to $a_0/2\pi$. The corrected results, also presented in Figures 5.1 and 5.2, show significantly improved agreement with

the experimental measurements at high tip speed ratios, although there is still a noticeable discrepancy at low tip speed ratios. The overestimation of the thrust is reduced to $119\% - 3\%$ and the bending moment to $56\% - 9\%$. The best agreement is at $\Lambda = 5$, corresponding to a Reynolds number of $Re = 6.1 \times 10^4$, which is within 5% of the aerofoil data value. The Reynolds number decreases with the tip speed ratio, which may further reduce the lift at lower values. It should also be noted that losses due to the root sections have not been included and should also improve the agreement.

Strictly speaking the suggested scaling is only valid for sections with an incidence lower than 13°, corresponding to region of laminar stall. This corresponds to tip speed ratios greater than $\Lambda = 3$. However, by $\Lambda = 2$ the incidence has increased sufficiently for most of the outboard sections to be operating in stall, which would result in greater loss of lift than modelled by the proposed correction. Packard (2012) identified the stall angle of the NACA 643618 aerofoil as 19°. Furthermore, the root sections will be at higher incidence and are likely to operate in stall up to higher tip speeds, contributing further to losses in the thrust and bending moments.

Two key discrepancies have been identified between the numerical simulation and experimental measurements. This discussion serves to indicate that the majority of the mean offset between the experimental and numerical results can be attributed to the loss of lift at low Reynolds numbers, although there is also likely to be some effect due to centripetal loading. It is also noted that the blade will operate partially in stall for most cases, which is currently not accounted for in the model. With this in mind, the following discussion on ambient turbulence and wake impact effects will focus on the comparison of the trends, which have been shown to be in reasonable agreement, and relative differences, neglecting the difference in mean amplitude. Implicit in this treatment is the assumption that the unsteady response conforms to the thin aerofoil lift curve slope. As will be seen, this assumption gives good agreement with the experiments, but it is noted that further investigation would be required to fully justify this approach.

5.2 Ambient turbulence

The impact of ambient turbulence on rotor loading is of interest in the design of wind turbines. In the following discussion, ambient turbulence refers to the higher frequency fluctuations corresponding to turbulence generated by the friction of the Earths surface, i.e the atmospheric boundary layer, rather than the lower frequency changes associated with solar heating and cooling and the corresponding pressure systems, which act to define the mean about which the former fluctuate (Harris, 1970). Whilst ambient turbulence is lower offshore, it is still significant and likely to contribute to a reduction in the fatigue life of turbine blades.

In order to investigate the effects of ambient turbulence the wind simulation of Veers (1988), discussed in Section 3.7, is used to simulate the inflow conditions from the experimental setup. A comparison between the two sets of results is used to further validate the numerical response and the numerical model is then used to gain further insight into the effects of ambient turbulence.

In the first instance, the incident flow is treated as a spatially correlated, meaning that all nodes within a plane are given the same velocity, time varying wind field with a von Kármán spectrum given by $U = 12$ m s^{-1}, $L_x = 0.29$ m and $I_u = 0.13$, as measured using hot-wire anemometry and discussed in Section 4.1.3. A random uniformly distributed Gaussian phase is applied to each frequency component and the inverse Fourier transform is taken to give a time history. Each grid plane perpendicular to the flow direction is assigned a uniform velocity corresponding to the time at which it propagates across the rotor, assuming Taylor's frozen turbulence hypothesis.

This model is a simplification of the full, spatially varying, turbulent wind model of Veers (1988). Without the spatial variation across the rotor disc the numerical model will not be capable of predicting the per revolution frequencies excited by the imbalance across the rotor disc. Therefore, the full model is also implemented to give the spatial variation, referred to as the uncorrelated model in the following discussion, which requires a coherence function to be defined.

Based upon the observations in Section 4.1.3 the von Kármán spectrum was used for the turbulence and hence the corresponding coherence, as derived by Harris (1970), is implemented. The result is a fully spatially and time varying turbulent wind field with characteristics of the longitudinal von Kármán spectrum matched to the experimental measurements. Whilst the correlated wind has an intensity of 13% as intended, the uncorrelated wind inputs vary between 10% and 15% intensity giving an average of 12.6% over the rotor plane.

As discussed by Veers (1988) there is a loss in variance associated with averaging between grid nodes. The wind in the simulation was generated at a sampling rate of 216 Hz, the closest integer value for the grid nodes to 200 Hz, but the simulation was run at 400 Hz in order to resolve the wake shape. Re-sampling the wind history at 400 Hz reduces the RMS of the wind by approximately 0.5%. Whilst there is no loss of variance due to spacial averaging for the correlated turbulence, this must also be taken in to account in the uncorrelated case. Linearly interpolating the wind series to the midpoint of each cell in the plane gives a range of variance of $8 - 12\%$ (mean value of 10.4%), corresponding to a mean reduction over the rotor plane of 2.2%. Extending this analysis to three dimensions gives a combined loss of variance for both spatial and time averaging of 2.3% for a 21×21 grid sampled at 216 Hz. The loss of variance due to spatial averaging is linked with the sharp reduction in coherence for increasing distance at all but the lowest frequencies. Increasing the spatial resolution to 41×41 increases the coherence between nodes and hence reduces the combined loss of variance to 1.5%, but requires a substantial increase in the storage requirements to generate the wind field.

Due to the stochastic nature of turbulence, a similar approach to the experiments is taken to reduce the statistical error in the predicted spectra: $n_d = 16$ realisations of the turbulent wind field are simulated for each tip speed ratio using batch processing on the Imperial College High Performance Computing Service[1]. Whilst this still gives a relatively high statistical error, $\pm 40\%$ with a confidence of 90%, the number

[1] `http://www.imperial.ac.uk/ict/services/teachingandresearchservices/highperformancecomputing`

of simulations was limited by the computational resources available. However, the statistical error in the RMS values is given by (Bruun, 1995):

$$\%\epsilon = \frac{z_\alpha}{\sqrt{N}} \tag{5.1}$$

where $N = 256 \times 16 = 4096$ giving an error of $\pm 4\%$ with a confidence of 99%.

A comparison of the predicted and measured mean thrust and blade root bending moment coefficients in turbulent and uniform inflow are shown in Figures 5.5 and 5.6, respectively. In agreement with the experimental results the mean values are similar to the uniform flow results. Both the correlated and uncorrelated results are within $\pm 1\%$ of the uniform flow values. Given that the wind time histories are generated with the same mean value as the uniform flow this is perhaps unsurprising, but one important consequence of this is that it implies the effects of turbulence are small enough to be treated linearly. This also confirms that the number of samples are sufficient for recovering the mean statistics.

As discussed in Section 4.3, the fluctuating component of the thrust loading from the experiments is dominated by the structural resonance of the support strut. As the structural response is not included in the present model, a useful comparison of the transient thrust loading is not possible: there is an order of magnitude difference in the RMS response, shown in Figure 5.7. Conversely, the bending moment measurements are largely unaffected by the strut resonance and hence a comparison is reasonable. Therefore, the fluctuating component of the thrust loading will be neglected in favour of the bending moment in the following discussion of the model. However, it is worth comparing the two numerical cases for the thrust coefficient. The correlated turbulence results in an RMS of the order of the turbulence intensity, whereas the uncorrelated turbulence only gives around half this value.

As discussed previously, there is a loss of variance associated with linear interpolation from the grid, which is more significant in the uncorrelated case. In addition, the admittance, the ratio of the wind input spectrum to the thrust output spectrum, is significantly reduced in the uncorrelated case, shown in Figure 5.8 for $\Lambda = 3$. This reduction will result in a reduced RMS for the thrust loading in this case. The

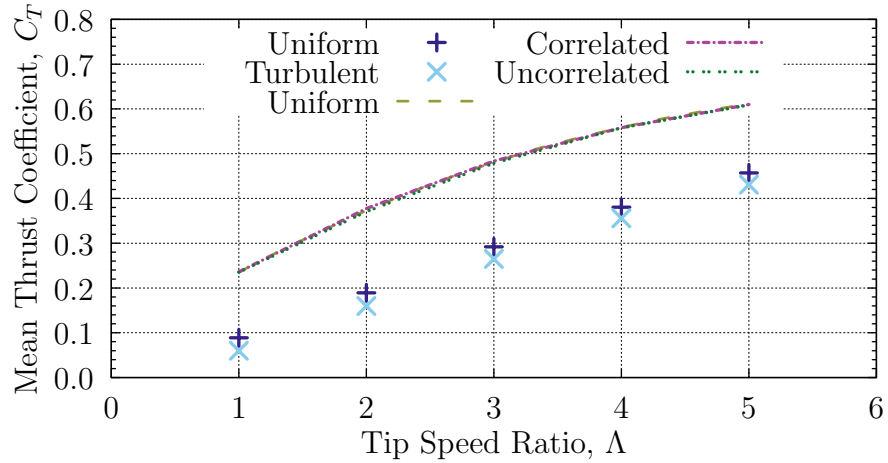


Figure 5.5: Comparison between simulation (lines) and experimental (symbols) thrust coefficient in turbulent flow.

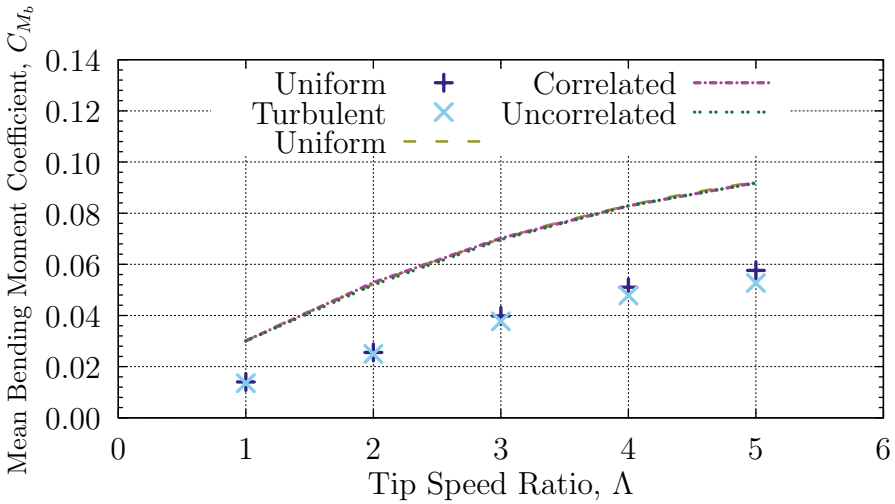


Figure 5.6: Comparison between simulation (lines) and experimental (symbols) blade root bending moment coefficient in turbulent flow.

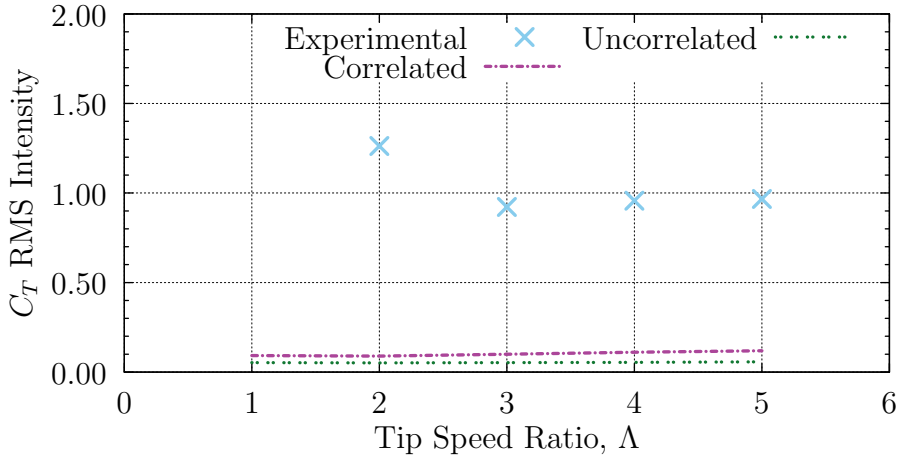


Figure 5.7: Comparison between simulation (lines) and experimental (symbols) thrust coefficient RMS in turbulent flow.

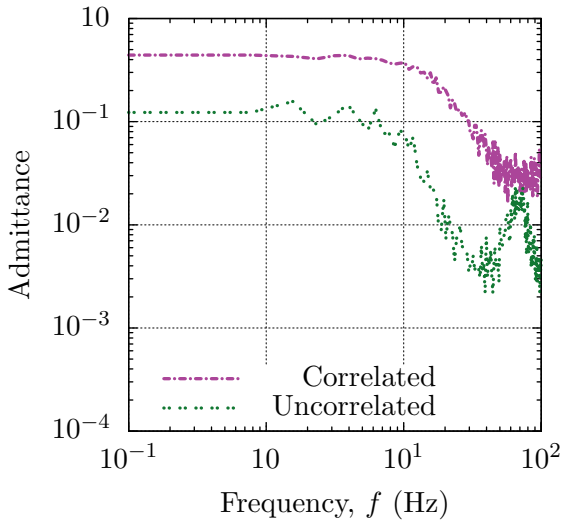


Figure 5.8: Comparison of simulation thrust coefficient admittance in correlated and uncorrelated turbulence at $\Lambda = 3$.

increase in admittance of the uncorrelated case at high frequency is attributed to the 3 per revolution excitation resulting from the blades passing through the largest eddies in the turbulent flow.

The bending moment RMS intensity is shown in Figure 5.9. The correlated model of the turbulent wind reproduces the trends well, but only predicts $40\% - 50\%$ of the amplitude. Congruent with the thrust loads, the uncorrelated model predicts even lower RMS intensity, and is nearly constant with tip speed ratio. Once again, the difference between the two numerical cases is attributed to a loss of variance and reduced admittance.

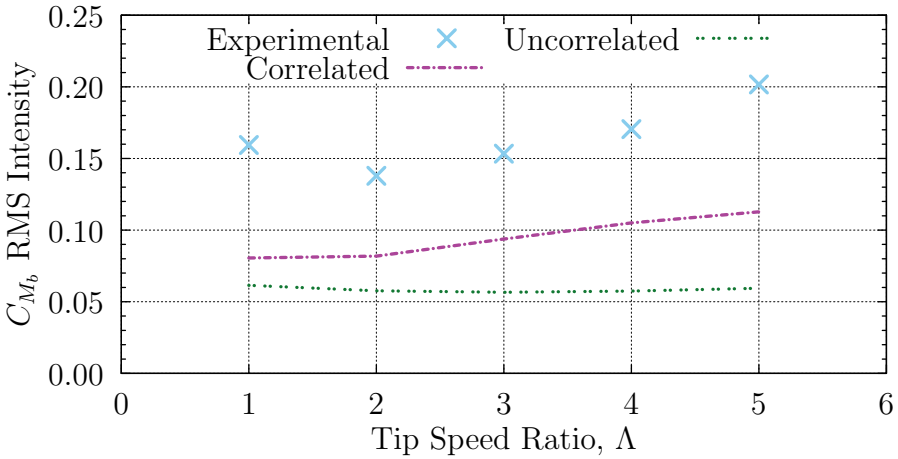


Figure 5.9: Comparison between simulation (lines) and experimental (symbols) blade root bending moment coefficient RMS in turbulent flow.

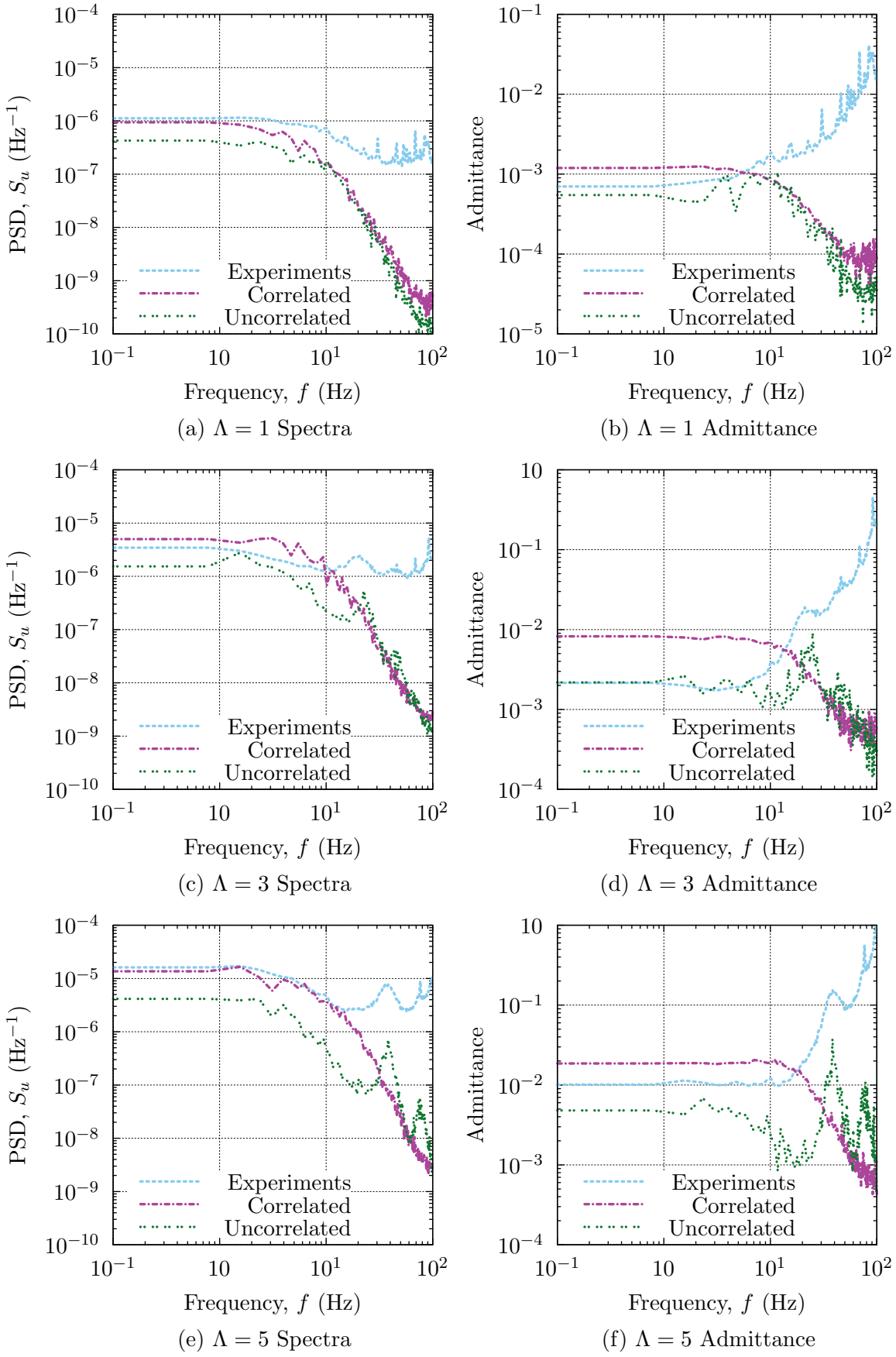
The admittance and spectra of the blade root bending moment are compared with the measured values, shown in Figure 5.10, for a range of tip speed ratios. Table 5.1 lists the harmonics of the rotational freuencies for each tip speed ratio, based on a reference velocity of 12 m s^{-1}. The uncorrelated turbulence has a lower admittance than the correlated case, with the exception of the higher frequencies where harmonics of the per revolution frequencies start to appear. The agreement between the two models is better at lower tip speeds than high, congruent with the increased discrepancy in RMS.

In terms of the comparison with the measurements, the admittance of the uncorrelated case gives better agreement than the correlated case, with better agreement at lower tip speeds. The low frequency admittance is well matched up to ≈ 10 Hz, except for $\Lambda = 5$ where it is approximately half the measured level. The increase in admittance at the per revolution frequencies is captured, but the amplitude is under-predicted. The correlated model over-predicts the admittance at low frequency, and under-predicts the value at high frequency, crossing over at around 15 Hz. The low frequency behaviour is clearly explained by considering the corresponding inputs to the model. In the correlated case, the entire blade will observe the same fluctuations in the velocity increasing the admittance. Conversely, both in the measurements and uncorrelated model, the velocities observed at each station along the blade will be different due to the passage of varying sizes of eddies through the rotor.

The underestimation of the admittance, and correspondingly the spectra, at high frequencies is in part responsible for the reduction in the RMS observed in the numerical simulations, compared with that observed in the measurements. Another

Λ	1	2	3	4	5
$1P$	7.6	15.3	22.9	30.6	38.2
$2P$	15.3	30.6	45.8	61.1	76.4
$3P$	22.9	45.8	68.8	91.7	114.6

Table 5.1: Rotor harmonic frequencies for a range of tip speed ratios, in Hz.



(a) $\Lambda = 1$ Spectra

(b) $\Lambda = 1$ Admittance

(c) $\Lambda = 3$ Spectra

(d) $\Lambda = 3$ Admittance

(e) $\Lambda = 5$ Spectra

(f) $\Lambda = 5$ Admittance

Figure 5.10: Comparison between experimental and numerical spectra and admittance of the bending moment coefficient in turbulent flow.

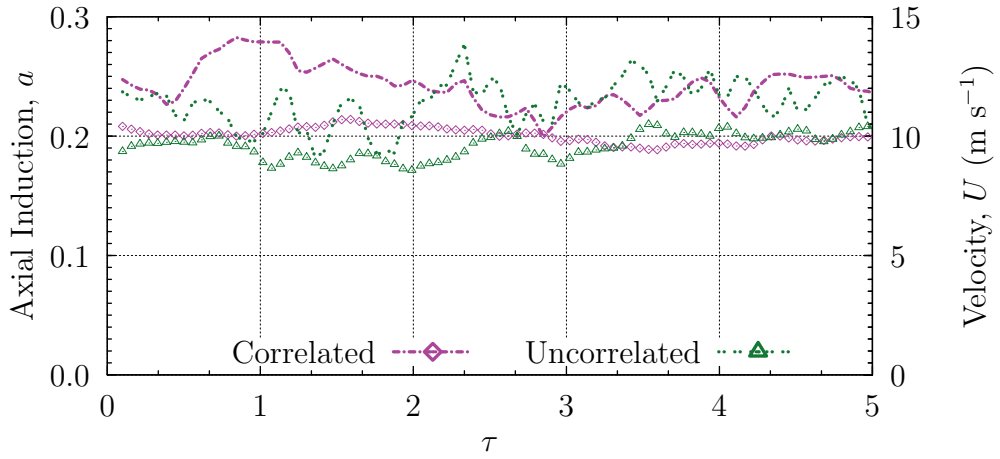


Figure 5.11: Variation of wake induction (symbols) at $\Lambda = 3$ in turbulent flow compared with local velocity (lines).

possible discrepancy derives from the neglected structural response. In comparing the RMS the experimental results are presented as the difference between the uniform and turbulent inflow measurements in order to distinguish the increase due to turbulence. Whilst this will account for some of the structural response, the result will still include some structural components due to excitation by the turbulence.

The blade root bending moment coefficient spectra are also shown in Figure 5.10. The power at low frequency is well reproduced by the correlated turbulence model, including the initial slope of the spectra. The agreement improves with increased tip speed ratio, but falls away at higher frequencies in all cases: the measured spectra exhibit per revolution frequencies, which are not captured by the correlated turbulence model. Whilst the uncorrelated turbulence under-predicts the amplitude, due to the loss of variance, at higher tip speed ratios it reproduces the per revolution frequencies. These peaks correspond to the $1P$, $2P$ and $3P$ peaks and exhibit a similar spread across frequencies. As noted previously, these frequencies occur due to the passage of the blade through the largest eddies in the simulation, which result in a significant imbalance across the rotor. The spread in the peak is caused by the stochastic nature of the excitation; the azimuth at which the eddies are encountered will vary between revolution resulting in a varying period in the excitation.

In order to investigate the unsteady response of the wake and wake induced velocities at the rotor, known as dynamic inflow, the induction on the blade at the

$0.66R$ position for $\Lambda = 3$ is shown in Figure 5.11 along with the local wind velocity. Maximum variation in the induction in the correlated wind is approximately $\pm 12.5\%$, corresponding to the turbulence intensity, and is marginally lower for the uncorrelated case at approximately 10%. Whilst the higher frequency components appear to be largely filtered out, the fluctuations of the velocities in the correlated and uncorrelated turbulence models can be seen in their respective inductions with a phase lag.

In the correlated case the phase lag appears to be approximately one or two thirds of a revolution, coinciding with the points in the wake corresponding to the same input at the two other blades. The response to velocity variations at the blade is a combination of two interlinked processes: the gradual change in circulation of the blade, described by Wagner's Function, and the build-up of vorticity in the wake. McNae (2013) observed that for a step change in velocity, the passage of the corresponding starting vortex and higher strength trailing wake from each blade resulted in step changes in the response at the blade. In the case of stochastic flow, where changes in velocity are gradual and not maintained long enough for the change in circulation of the blade to settle, there is still a corresponding 'starting vortex', or change in vorticity of the wake. Therefore the response to a change in velocity at the blade is governed by the vorticity shed into the wake at that time. For correlated turbulence, this will be the same for all three blades. Therefore, the response to a change in velocity will coincide with the passage of the wake from each blade past the observed blade.

This phase lag is not so apparent in the uncorrelated case, where the change in velocity is not the same for each blade, although there is some evidence: the peak in velocity at $\tau = 2.3$ is followed by a peak in induction one third of a revolution later. This indicates that the induction in the uncorrelated case is mainly effected by structures large enough to give high correlation over several blades, or indeed over the entire rotor disc.

One consequence of increased turbulence intensity has been identified as an increase in fatigue on the blades. Cycle counts of the measured blade root bending moment

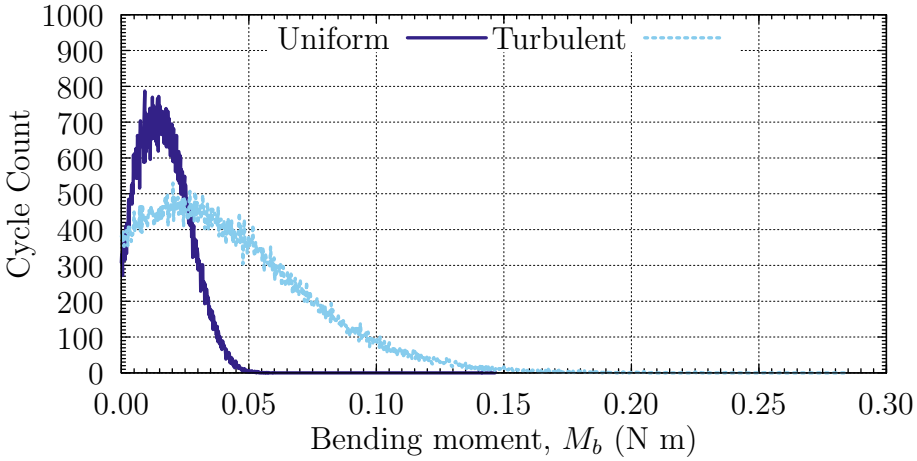


Figure 5.12: Comparison of uniform and turbulent fatigue load histograms for $\Lambda = 3$.

for uniform and turbulent flow are shown in Figure 5.12. There is a shift to higher load cycles, which will correspond to increased fatigue of the blade. This confirms the observation of several authors that increased turbulence corresponds to reduced fatigue life. In order to predict the cycle counts using the numerical model significantly longer time histories are required. However this would require approximately a hundred times the number of simulations in order to produce the same time history length as the measurements. Alternatively, the method proposed by Sutherland and Osgood (1992) might produce reasonable results, assuming a suitable distribution of synthetic time histories could be established.

5.3 Upstream rotor wake impact

The effects of upstream rotor wake impact are becoming increasingly important as wind farms move offshore into large, closely packed regular arrays. In this section the developed model is used to investigate these effects. The layout investigated is the same as that used in the experiments, shown in Figure 4.1 of Section 4.1, and assumes that both rotors have the same geometry and are at the same height. In order to model this in the vortex lattice method, an explicit wake model, based on the work of Ainslie (1988) and fitted to the experimental measurements, is proposed.

As discussed in Section 2.3, a Gaussian profile is preferred for the explicit modelling

of the upstream rotor wake. The Gaussian profile takes the form

$$\frac{U_\infty - U}{U_\infty} = Ae^{-\frac{1}{2}\left(\frac{f(r)}{C}\right)^2} \tag{5.2}$$

where $f(r) = \left((y-\Delta y)^2 + z^2\right)^{\frac{1}{2}}$ is a function of the local radial position and upstream rotor wake lateral centreline offset Δy, and $A = \Delta U$ and C are coefficients prescribing the centreline velocity deficit and wake width, respectively. The origin is assumed to be at the centre of the hub. In order to determine the values of the two coefficients, a least squares fit of Equation 5.2 to the measured profiles discussed in Section 4.2 was determined using a commercial software package (MATLAB (R2013b), 2013).

Initially both coefficients were included in the fit expression, giving a range with respect to tip speed ratio of $0.16 - 0.22$ for the wake width. As observed in Figure 4.5 of Section 4.2.1 the wake width is constant with tip speed ratio. Therefore, to retain this characteristic, a value of $C = 0.2$ was chosen, corresponding to a wake width of approximately $1.4D$ and the mean value of the identified range.

Modification of the fit expression to employ the chosen value of the wake width yielded the centreline velocity deficit, ΔU, as a function of tip speed ratio, shown in Figure 5.13. A quadratic equation is fitted to the data:

$$\Delta U = C_2\Lambda^2 + C_1\Lambda + C_0$$

where the coefficients are $C_0 = 1.37347 \times 10^{-2}$, $C_1 = 1.50476 \times 10^{-1}$ and $C_2 = -1.60873 \times 10^{-2}$ for the measured profiles. It is noted that whilst these values represent a good fit to the measured data presented here, further parameterisation of the expressions for A and C would be necessary to yield a more general equation; including the effects of downstream distance and perhaps turbulence intensity.

Using the suggested values for the centreline velocity deficit and wake width yields the fit shown in Figure 5.14. The agreement is acceptable, although the slight acceleration of the flow outside the wake region is not modelled. It is also noted that the measurements made at $\Lambda = 5$ appear to indicate a slightly flatter wake shape than given by the Gaussian model, but the fit is still considered acceptable.

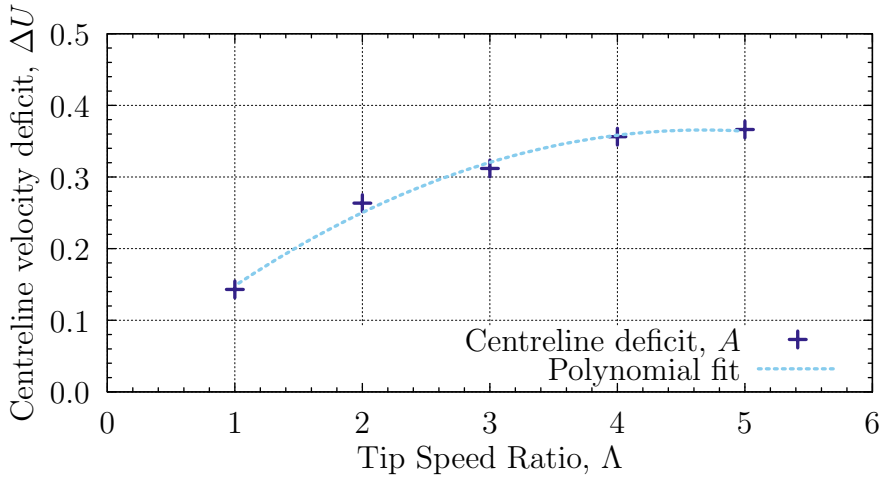


Figure 5.13: Wake centreline deficit quadratic fit.

As a first approximation, this mean velocity deficit profile is applied to the Cartesian grid and propagated across the rotor with the mean free stream velocity. The mean thrust and blade root bending moment coefficients are shown in Figures 5.15 and 5.16, respectively. The result of the wake impacting is qualitatively similar: the greatest deficit is for the aligned case and as the upstream rotor is laterally offset the loading recovers to the undisturbed flow value, such that with the upstream wake laterally offset by $1D$ the uniform flow case is recovered. The spread in the mean bending moment at each tip speed is approximately the same, however there appears to be a slightly steeper gradient. Conversely, the thrust exhibits the same gradients, but a reduced deficit with increasing tip speed ratio, most notably in the aligned case.

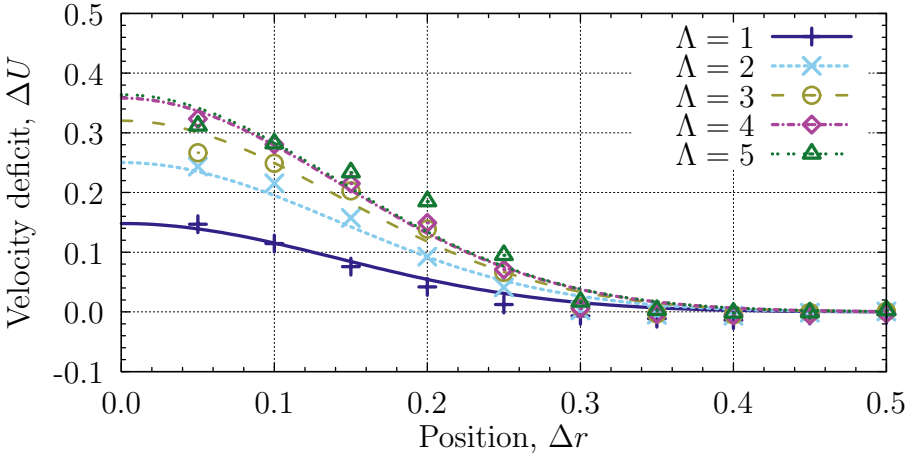


Figure 5.14: Comparison of measurements (symbols) with wake velocity deficit model (lines).

One explanation for the reduced deficit with increasing tip speed ratio for the aligned rotor is reduced drag of the nacelle in the wake velocity deficit: the drag is corrected for in the zeroing of the thrust loads, but is measured for the case of uniform inflow and will decrease with the inflow velocity. This will be most significant in the aligned case, where the core of the upstream wake will pass directly over the nacelle.

Time histories of the fluctuating component of the blade root bending moment for $\Lambda = 3$ are shown in Figure 5.17. The experimental data has been passed through a low pass FIR filter to remove frequency content higher than the revolution frequency. For the aligned case, the mean velocity deficit wake model does not result in any azimuthal variation and as such the fluctuating component is zero. For upstream rotor wake centreline offsets between $\Delta y = 0.25D$ and $0.75D$, both the amplitude and frequency of the fluctuating loads is in reasonable agreement. Whilst the numerical results maintain a constant amplitude, the measurements vary, indicating lower frequency components in the loading. Finally, with the upstream rotor wake centreline laterally offset by $\Delta y = 1.00D$ the numerical model is not capable of predicting the amplitude of the oscillations, but still shows some azimuthal variation with the correct frequency.

Azimuthally averaging of the filtered fluctuating component of the blade root bending moment, shown in Figure 5.18 for $\Lambda = 3$, removes some of the variation due to the low frequency components. The agreement of the $\Delta y = 1.00D$ laterally offset wake is improved, although the scatter of the measured data obscures the trend making a true comparison difficult. Conversely, the aligned case shows no difference. The agreement for the $\Delta y = 0.25D$ case is particularly good. In this configuration the variation of the deficit over the azimuth will most closely resemble a sinusoidal signal, meaning that most of the variation is captured by the per revolution frequency. At the two intermediate offsets, the agreement is not as good, although the general trend is still preserved. In these cases the rotor will experience regions of undisturbed flow and the resulting deficit will no longer follow a sinusoid. Therefore, the higher harmonics of the revolution frequency, which have been filtered out of the measurements, are required to reproduce the shape. To illustrate this, the measure-

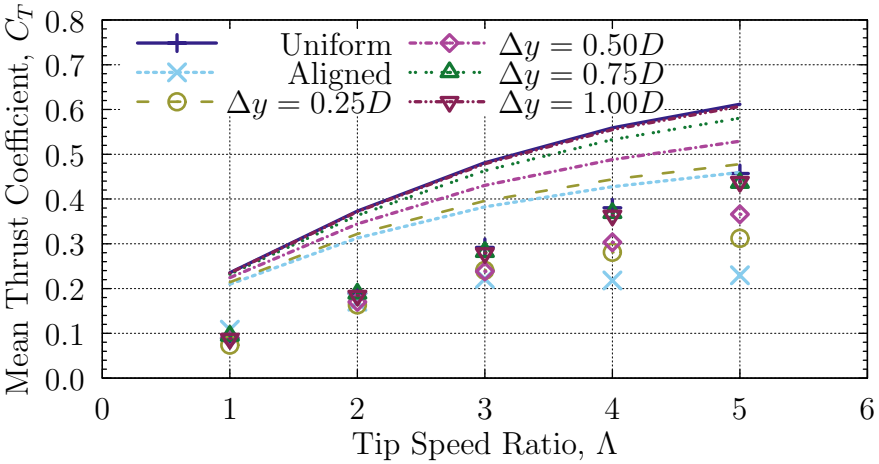


Figure 5.15: Comparison between simulation (lines) and experimental (symbols) thrust coefficient in an upstream rotor wake.

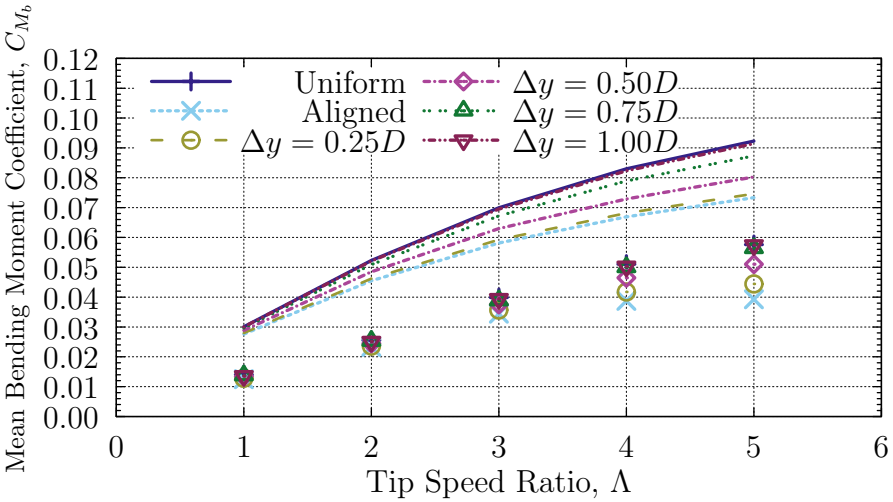
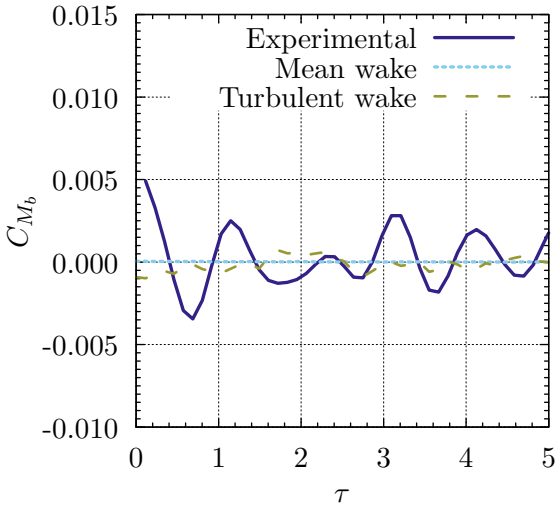
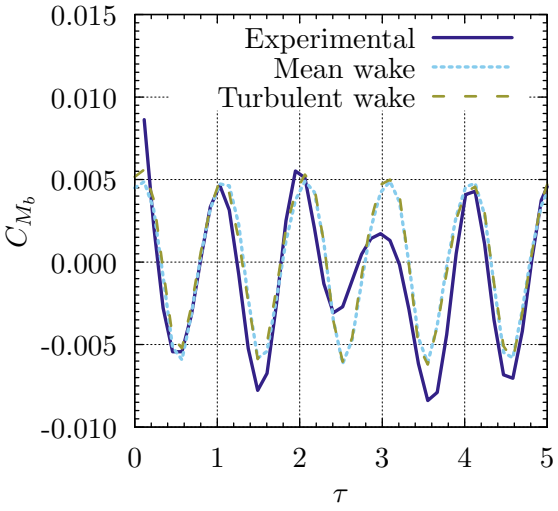


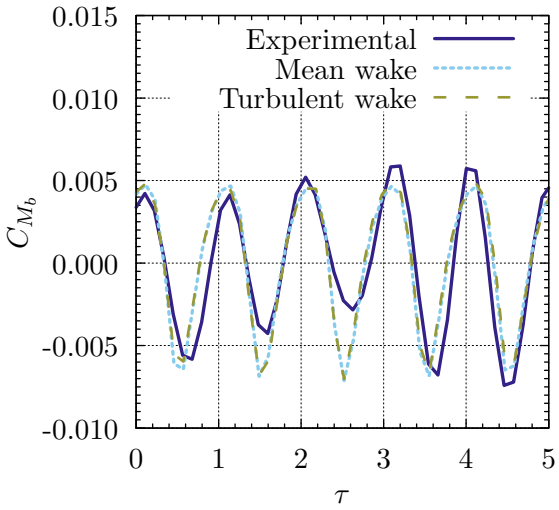
Figure 5.16: Comparison between simulation (lines) and experimental (symbols) blade root bending moment coefficient in an upstream rotor wake.



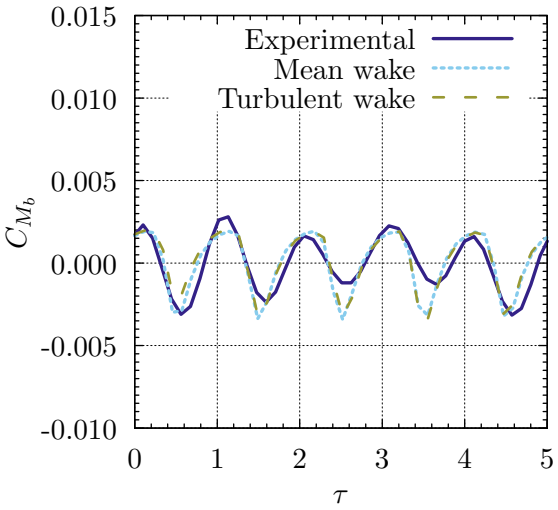
(a) Aligned



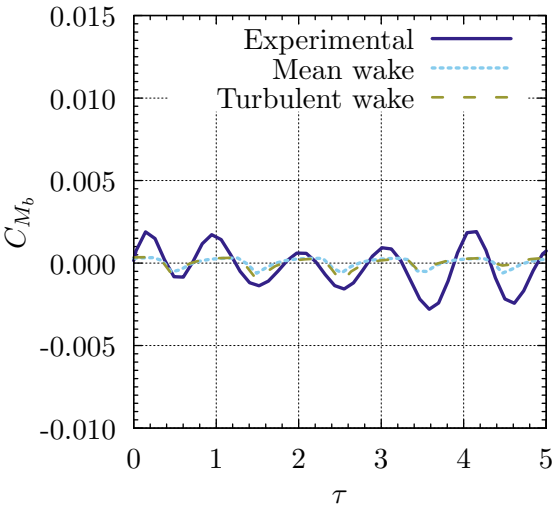
(b) $\Delta y = 0.25D$ lateral offset.



(c) $\Delta y = 0.50D$ lateral offset.



(d) $\Delta y = 0.75D$ lateral offset.



(e) $\Delta y = 1.00D$ lateral offset.

Figure 5.17: Comparison between measurements and simulation of upstream rotor wake impact load time histories for increasing lateral offset at $\Lambda = 3$.

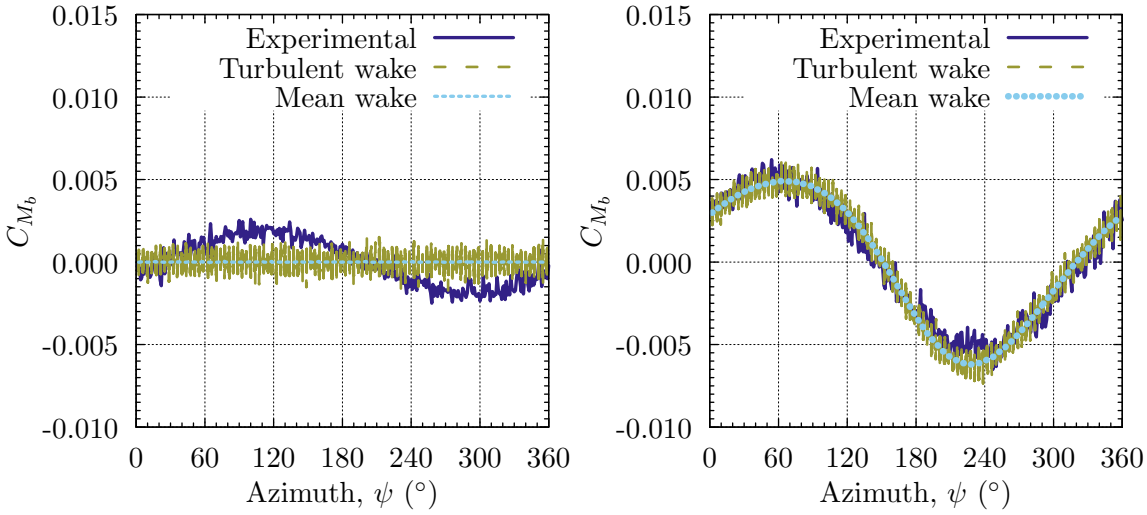
ments for $\Delta y = 0.50D$ are re-filtered to include the second harmonic of the rotation frequency and the results included in Figure 5.18c. The agreement is significantly improved, although there is still some disparity.

The reasonable agreement for the intermediate offsets supports the assumption of the thin aerofoil result for the lift curve slope, $a_0 = 2\pi$, of the unsteady loads. However, as already noted, further investigation is required in order to formally justify this effect.

In order to improve the agreement for the aligned and $\Delta y = 1.00D$ laterally offset cases it was deemed necessary to model the added turbulence of the wake. The wake turbulence was modelled using the same method as the ambient turbulence with parameters corresponding to the measured wake turbulence, identified in Section 4.2.1. The turbulence is assumed uncorrelated, scaled with the local mean velocity with intensity $I_u = 0.05$ and length scale $L_x = 0.06$ m, in agreement with the observations of the measurements, and is limited to the wake region with a width of $1.4D$.

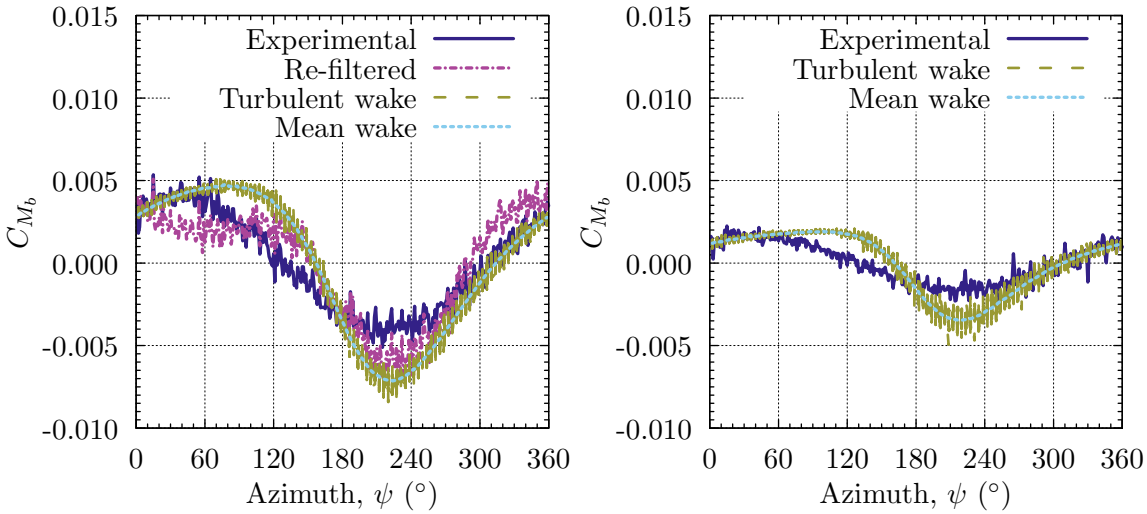
Modelling of the wake turbulence results in some improvement in the agreement of the time histories. However, whilst the aligned case now exhibits some variation, it is still significantly less than the measurements and doesn't appear to correlate particularly well with the frequency of oscillation. For the $\Delta y = 1.00D$ offset case, the difference is less obvious, although some of the oscillations peak at slightly higher values. For lateral offsets between the previous two, the effect of the turbulence is minimal with the turbulent wake model showing much the same response. This suggests that the mean velocity deficit is the dominant factor in determining the unsteady response, but could also indicate issues with the wake turbulence model.

Two possible issues with the wake turbulence model have been identified. The first is the loss of variance due to interpolation discussed in the previous section with respect to uncorrelated turbulence. Given both the low intensity and coherence of the wake turbulence, any reduction will have a significant impact on the resulting turbulence profile. The second, and possibly more significant, is that coherent



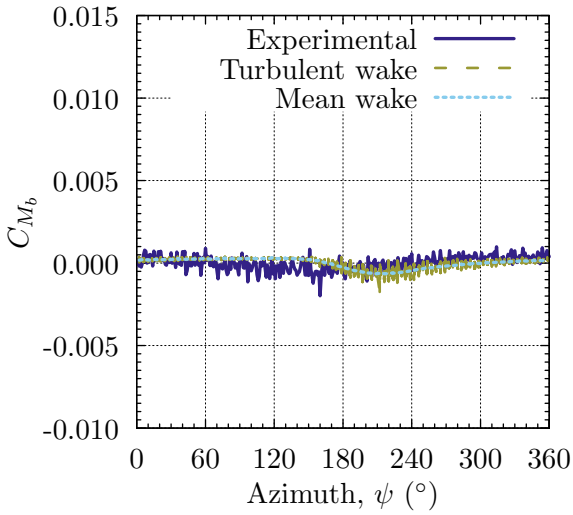
(a) Aligned

(b) $\Delta y = 0.25D$ lateral offset.



(c) $\Delta y = 0.50D$ lateral offset.

(d) $\Delta y = 0.75D$ lateral offset.



(e) $\Delta y = 1.00D$ lateral offset.

Figure 5.18: Comparison between measurements and simulation of upstream rotor wake impact azimuthally binned loads for increasing lateral offset at $\Lambda = 3$.

structures related to the tip vortex have been neglected. This is in part due to the implementation of the von Kármán spectrum and coherence. Whilst this model agrees with the measurements at most frequencies, it neglects the increased power and coherence at the per revolution frequencies attributed to the passage of the tip vortex. Consequently, the fluctuating loads and RMS will be reduced.

Furthermore, the von Kármán coherence model assumes homogeneity of the turbulence. However, the wake coherence model was based on the measured coherence with the centreline. In the case of ambient turbulence, where the profile is reasonably homogeneous, this will give an accurate measure of the coherence. Conversely, given the mean velocity deficit profile, the flow in the turbine wake is non-homogeneous and hence the measured coherences are unlikely to accurately represent the wake. Therefore, the von Kármán coherence model may not be the most appropriate. A modified form of the Davenport exponential coherence function, proposed by Solari (1987), was also investigated, but was found to give poor agreement with the measured values.

Finally, whilst the length scale was matched to the experiments, the identified value is significantly lower than the rotor diameter which is suggested in the literature to dominate the turbulence in the wake. These length scales may correspond to eddies associated with the tip vortex. It is also highly likely that the downstream rotor will influence the upstream rotor wake, possibly distorting the turbulence and causing expansion of the wake. This is neglected in the current model, but may also have a significant impact. Consequently, it is suggested that the model of the wake turbulence requires further investigation, including more detailed measurements of the coherence, possible interaction between the upstream rotor wake and downstream rotor and representation of coherent structures such as the tip vortex.

One possible solution would be to utilise the vortex wake modelled in the simulation, which explicitly models the tip vortex roll-up in the wake and the influence of the downstream rotor on the upstream rotor wake. However, this approach would give rise to a number of issues: in order to accurately model the wake expansion, the neglected components of the free stream turbulence would need to be incorporated

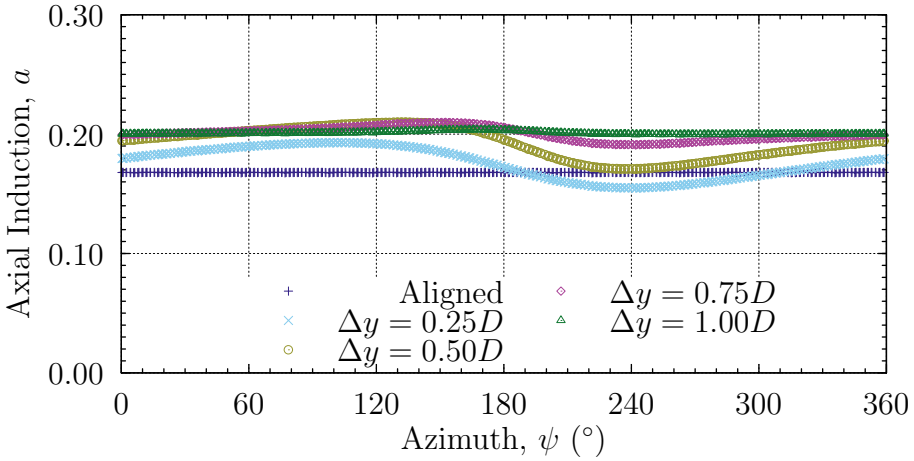


Figure 5.19: Azimuthal variation of wake induction at $\Lambda = 3$ for different laterally offsets.

into the model adding additional complexity and computational expense; the addition of a second vortex wake would double the crucial computation cost associated with computation of the induced velocities; as discussed in Section 3.3, there exists a numerical instability in the computation of local velocities from vortex filaments. In the latter case, it is noted that application of the vortex core to the bound vorticity is not desirable as it will strongly influence the calculation of the blade circulation. As such, the simulation would be prone to strong instabilities in the upstream wake, making this approach unsuitable.

In order to investigate the dynamic inflow effects associated with wake impacting, the axial induction of the wake on the blade is investigated using the numerical model. The induction factor, a, is defined as the ratio of the wake induced velocity to the undisturbed flow, $U_\infty = 12$ m s^{-1}, at the blade pitch axis. Figure 5.19 shows the variation of the induction factor at different lateral offsets with azimuthal position at the $0.66R$ radial position of the blade for $\Lambda = 3$. The centre of the wake impact is at 180°.

The axial induction with the upstream rotor laterally offset by $\Delta y = 1.00D$ is reasonably constant with azimuth, coinciding with the uniform flow value of $a = 0.2$. Similarly, for the axially aligned upstream rotor the induction is also constant, but as a result of the velocity deficit in the wake and the reduced loading of the blade, the corresponding strength of the wake vorticity and resulting axial induction is

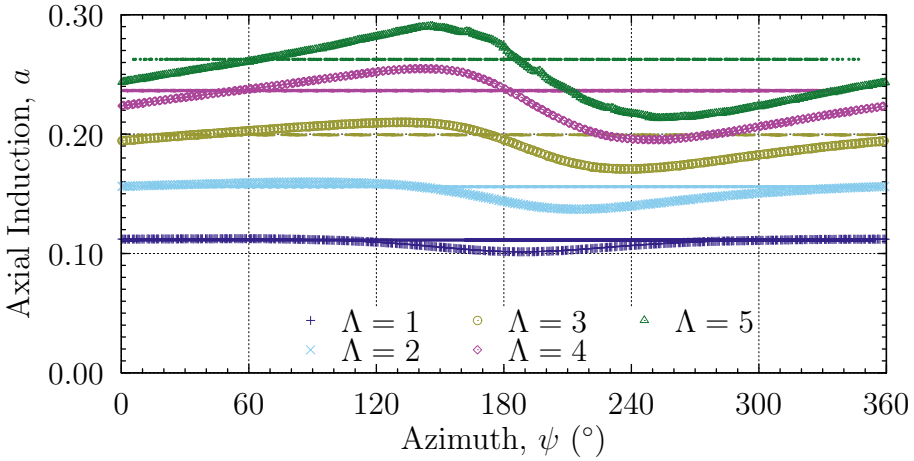


Figure 5.20: Azimuthal variation of wake induction for a $\Delta y = 0.50D$ laterally offset wake for $\Lambda = 1 - 5$. Horizontal lines indicate the uniform flow induction factor.

reduced, in the latter case by 15%. For the intermediary lateral offsets an azimuthal variation in induction becomes apparent: a slight increase just prior to the blade entering the upstream rotor wake, followed by a decrease to a minimum as the blade exits the wake and eventual recovery of the initial induction. For $\Delta y \geq 0.5D$, the induction factor at $\psi = 0°$ or 360° is unaffected by the wake impact. The deficit in the induction decreases as the upstream rotor is laterally offset. This is due to the reduced velocity deficit and corresponding wake vorticity.

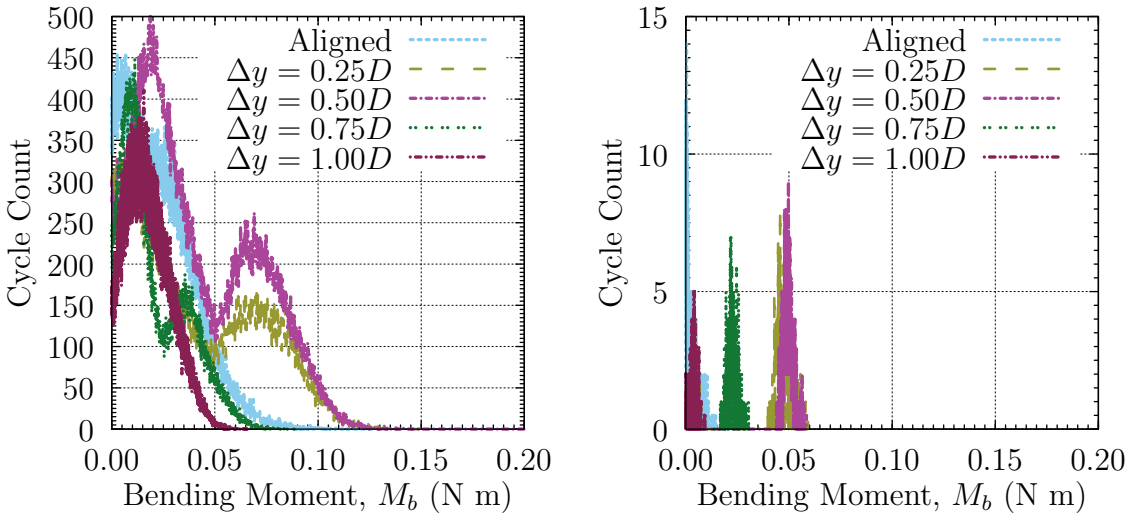
Conversely, the variation in axial induction increases with the tip speed ratio of the upstream turbine, shown in Figure 5.20 for a $\Delta y = 0.50D$ laterally offset wake. As the tip speed ratio increases, so too does the velocity deficit in the wake. Therefore, whilst for a given lateral offset of the wake, the overlapping region between the wake and rotor is constant, the amplitude of the velocity variation in this region increases with tip speed ratio of the upstream turbine. As a consequence, the width of the wake disturbance appears to increase, although in reality the width is constant but the disturbance is minimal at the outer edges.

The variation of axial induction due to wake impact is explained via two processes as follows. Firstly, the strength of vorticity in the wake is considered. As the blade passes through the velocity deficit of the upstream rotor wake the circulation around the blade decreases and the strength of the shed vorticity is reduced. Outside the upstream rotor wake the circulation increases again and the strength of the shed

vorticity gradually returns to the undisturbed flow value. Therefore, the induction factor reduces in the wake impact region and increases outside of this region up to the undisturbed value as the wake induced velocity varies with the strength of the shed vorticity. Secondly, due to the velocity deficit in the upstream rotor wake, the propagation velocity of the downstream rotor wake is equivalently reduced. This results in a closer proximity between the rotor blade and shed vorticity in the downstream rotor wake. For the sake of argument it is assumed the vorticity in the wake is constant, this would then exhibit as an increase in the wake induced velocity over the wake impact region. Superimposing these two effects gives the observed variation in the axial induction: the closer proximity mitigates the reduced strength of the wake vorticity as the blade passes into the upstream rotor wake, followed by a reduction through the wake region, with a recovery towards the undisturbed values when the blade emerges into the undisturbed flow.

Finally, as discussed in Section 2.5, one effect of upstream rotor wake impact is an increase in the fatigue of turbine components. Cycle counts of the measured blade root bending moment for each of the upstream rotor wake positions are shown in Figure 5.21. Both the axially aligned and $\Delta y = 1.00D$ laterally offset wakes show single peaks in the low load range, similar to the uniform flow case discussed in the previous section. This indicates that the wake turbulence may have minimal impact on the loading and corresponding fatigue, which contradicts evidence in the literature suggesting that this is a key component of increased fatigue as a result of wake impact. However, for the intermediate lateral offsets of $\Delta y = 0.25D$ to $0.75D$ the fatigue cycle counts show a double peak, with a significant proportion of load cycles moving to a higher loading. This will result in increased fatigue as discussed in the literature, but would imply that the principal effect is the azimuthal variation resulting from the mean velocity deficit in the upstream rotor wake.

Also included in Figure 5.21 are cycle counts from the turbulent wake model. As with the ambient turbulence case, the time histories are not sufficiently long in order to accurately predict the cycle counts. However, the simulated results do show the same shift in load cycles to higher loads. This suggests that if a sufficiently long



(a) Measurements.

(b) Turbulent wake model.

Figure 5.21: Comparison of wake impact fatigue load histograms for $\Lambda = 3$.

time history could be generated using the numerical model then it may be possible to reproduce the cycle counts of the experimental models. However, as discussed in the ambient turbulence case, this would require significantly longer time histories. In order to utilise the method proposed by Sutherland and Osgood (1992), the representation of the wake turbulence would need to be improved first.

5.4 Summary

The developed model has been compared with measurements of the blade root bending moment and turbine thrust for uniform and turbulent inflow and wake impact. The disparity between the measured and predicted response to uniform inflow is attributed to a reduction in the mean lift curve slope to $a_0 = 3.11$ rad^{-1}. However, it has also been shown that the unsteady response conforms with the thin aerofoil lift curve slope of $a_0 = 2\pi$ rad^{-1}. Further discrepancies between the uniform flow results are attributed to the absence of a stall model in Aeolus.

The comparison with the measurements for ambient turbulence showed similar trends in the predicted results. Both correlated and uncorrelated models of turbulence were investigated. The former was able to better predict the low frequency end of the blade root bending moment spectra, whilst the latter better predicted

the admittance. In addition, the uncorrelated model was able to reproduce the increase at the per revolution frequencies, but suffers from a loss of variance due to interpolation. The developed model was also used to investigate the dynamic inflow response to the stochastic inflow. It is suggested that the response is governed by the shed vorticity in the wake, corresponding to eddies large enough to give sufficient correlation over the rotor disc. Cycle counts of the measured blade root bending moment indicate a shift to higher load ranges, increasing the fatigue as suggested in the literature. However, the numerical time histories were insufficient for predicting this behaviour.

Wake impact has also been investigated. Again, the trends in the mean loads are reasonably well reproduced with some discrepancies, in part due to the estimation of the tare drag of the nacelle. Furthermore, comparison of the time histories of the fluctuating loads shows good agreement for intermediate lateral offsets, $\Delta y = 0.25D - 0.75D$, of the wake. This is presented as support for the assumption of the thin aerofoil lift curve slope for unsteady loading. However, the model of wake turbulence is found to be insufficient to capture response in some cases. In particular, coherent structures related to the tip vortex are not represented, which it is suggested is in part responsible for the failure to predict the response of either the axially aligned or $\Delta y = 1.00D$ cases. The response of dynamic inflow to wake impact was investigated with the numerical model. It has been suggested that this is a combination of the proximity of the wake and the reduction in the shed vorticity with the wake impact region.

Finally, the fatigue implications of wake impact are discussed with reference to cycle counts from the measurements. These suggest that the mean velocity deficit is the more dominant fatigue load, rather than the wake turbulence as suggested in the literature. As in the ambient turbulence case, the numerical model does not provide sufficient time histories for an accurate estimation of the cycle count. However, the shift in cycle to higher bending moment is still observed in the numerical data. This suggest that if the wake turbulence model could be sufficiently improved, then the numerical model may be capable of predicting the fatigue loading.

6 Conclusions and future work

The stated aim of the project presented in this thesis was the investigation of upstream rotor wake impact on downstream horizontal axis wind turbines. Wake impact is likely to become an increasingly important factor in the design of offshore wind farms as the market strives for increased energy density and reduced installation costs.

Aeolus, an unsteady implementation of the vortex lattice method, has been developed to model a horizontal axis wind turbine rotor and wake. A Cartesian velocity grid was superimposed over the computational domain to support modelling of ambient turbulence and upstream rotor wakes. The model has been verified against existing models and analytical solutions for a flat plate wing and against results from blade element momentum theory for the rotor.

In conjunction with the aforementioned development, measurements of the turbine thrust and blade root bending moment on a turbine operating in uniform and turbulent inflow and under the influence of upstream rotor wake impact were undertaken in the Honda wind tunnel. In addition, hot-wire measurements were recorded to aid the characterisation of the ambient and wake turbulence as well as the mean velocity deficit in the wake.

The measurements and numerical model have been compared for uniform inflow, ambient turbulence, summarised in Section 6.1, and wake impact, summarised in Section 6.2, and the resulting observations discussed. Recommendations for future work are presented in Section 6.3.

Comparison of the measurements and predictions in uniform inflow identified a mean offset between the two sets of data. This has been attributed to a reduction in the lift curve slope at low Reynolds number, based on data available in the literature. The numerical predictions were corrected by scaling the predicted loads, giving significantly improved agreement. Further discrepancies at low tip speeds are identified as stall of the blade, which has not been incorporated into the current model. Finally the trends in both the mean thrust and blade root bending moment

with tip speed ratio are reproduced. Noting the difference in lift curve slope, the developed model is assumed to correctly capture the response of the rotor. Finally, the unsteady loading was assumed to match the thin aerofoil lift curve slope, which has been justified based upon the observed agreement of the fluctuating loads in the following sections.

6.1 Ambient turbulence

Ambient turbulence was modelled using the Sandia method. Based on the wind tunnel measurements a von Kármán spectrum was used. Both correlated and uncorrelated models were investigated. Whilst the former gives better agreement for the low frequency end of the blade root bending moment spectra, the latter gives better agreement with the admittance function. The uncorrelated model suffers from a loss of variance due to interpolation from the velocity grid.

The mean response to the turbulence is similar to uniform inflow, observed in both the wind tunnel measurements and numerical simulation. One consequence of this is that the effect of turbulence may be small enough to support a linear approach in modelling.

The dynamic inflow response is investigated using the numerical model. The higher frequency content in the stochastic inflow is filtered out, with the induction only exhibiting a response to larger variations. The phase lag between the inflow velocity and wake induced velocity indicates that the response may be governed by vorticity shed into the wake by eddies that are large enough to have a high correlation over the rotor disc.

Cycle counts of the measured blade root bending moment indicate a shift to higher bending moment ranges in turbulent inflow, in agreement with the literature. This would imply an increased fatigue. However, the numerical model time histories were not sufficiently long to support estimation of these effects.

6.2 Wake impact

In agreement with the literature, hot-wire measurements of the upstream rotor wake support the use of a Gaussian profile to model the mean velocity deficit. Furthermore, the measurements indicate that whilst the wake width is independent of tip speed ratio, the centreline velocity deficit can be approximated by a quadratic function of tip speed ratio.

The proposed model is found to give reasonable agreement with the measured trends in the reduction of the thrust and blade root bending moment due to wake impact. For lateral offsets of the upstream rotor wake centreline, time histories of the fluctuating loads show reasonable agreement, suggesting the mean velocity deficit is the dominant effect. The agreement suggests that the assumption of the thin aerofoil lift curve slope for the unsteady loads, as used in the model, is appropriate.

However, in the axially aligned case, and to some extent the $\Delta y = 1.00D$ offset wake, the wake turbulence is deemed to dominate the response. An attempt to model the response was made using a similar approach to the ambient turbulence. Based on the wind tunnel measurements the wake turbulence spectra was modelled as a von Kármán spectrum, scaled according to the mean velocity deficit, with constant intensity and length scale. Whilst this resulted in some improvement, the key features of the response in the axially aligned flow were not reproduced. Based on observations from the measurements it is proposed that the wake includes coherent structures related to the tip vortex, identified by harmonics of the rotation frequency in the wake spectra and increased coherence between the centreline and tip region at these frequencies, which were neglected in the current approach. It is suggested that this may account for the disparity between the measurements and predictions.

An investigation of the dynamic inflow response to the mean velocity deficit wake impact model shows that the response is a combination of two factors: proximity of the downstream rotor wake and the reduction in the shed vorticity as the blade passes through the upstream rotor wake region.

Finally, the measured time histories are used to discuss some of the fatigue implications of wake impact. Comparison of cycle counts of the blade root bending moment at different lateral offsets suggest that the mean velocity deficit is the key component in shifting cycles to higher bending moment ranges, rather than the wake turbulence. Cycle counts of the numerical time histories show similar trends in the shift to higher load cycles, but as already noted significantly longer time histories would be required in order to provide a proper prediction.

6.3 Future work

The developed model could be improved directly by addition of a model to treat both static and dynamic stall, which are likely to have a significant impact on the turbine loading at low tip speed ratios. Furthermore, given the issues resulting from low Reynolds numbers in the experiments, validation of the developed model against field data would be beneficial.

Investigation of the lift curve slope of unsteady motion at low Reynolds numbers could yield some interesting observations. The results presented in this thesis suggest that, whilst the mean flow may have a reduced lift curve slope, the fluctuating loads due to unsteady motions follow the thin aerofoil result. An experiment could be devised to confirm this observation and give further insight into the mechanisms involved.

Further investigation of the turbulence in the wake of a horizontal axis wind turbine is recommended, with particular emphasis on the modelling of coherence of the turbulent components and coherent structures related to the tip vortex. This would require more detailed measurements of the wake structure, perhaps utilising more advanced methods such as particle image velocimetry. Whilst it has been hypothesised that the mean velocity deficit dominates the response to an upstream rotor wake with a laterally offset centreline, the wake turbulence is important in the aligned case which will account for a significant proportion of wake impact scenarios.

One of the key consequences of the load scenarios investigated in this thesis is the po-

tential for increased fatigue. This has been briefly addressed with reference to cycle counts of the measured time histories. In order to predict these results, the numerical model would need to generate significantly longer time histories, presently limited by the available computational resources. Alternatively, it is suggested that the synthetic time history approach proposed by Sutherland and Osgood (1992) could be adopted with the developed model providing estimates of the power spectral density. However, this would be contingent on the previously discussed improvements to the wake turbulence model.

References

Abramovich, G. N. (1963), *The Theory of Turbulent Jets*, MIT Press, Chapter 5. ISBN: 9780262511377.

Adaramola, M. S. and Krogstad, P.-Å. (2011), 'Experimental investigation of wake effects on wind turbine performance', *Renewable Energy* **36**(8), 2078 – 2086. doi: 10.1016/j.renene.2011.01.024.

Ainslie, J. (1988), 'Calculating the flowfield in the wake of wind turbines', *Journal of Wind Engineering and Industrial Aerodynamics* **27**(13), 213 – 224. doi: 10.1016/0167-6105(88)90037-2.

Alfredsson, P.-H. and Dahlberg, J.-A. (1979), A preliminary wind tunnel study of windmill wake dispersion in various flow conditions, Technical Note AU-1499, Flygtekniska Försöksanstalten.

Aubrun, S., Devinant, P. and Espana, G. (2007), Physical modelling of the far wake from wind turbines. application to wind turbine interactions, *in* 'European Wind Energy Conference and Exhibition 2007', Vol. 2, European Wind Energy Association, pp. 1260–1267.

Bagai, A. and Leishman, J. (1993), 'Flow visualization of compressible vortex structures using density gradient techniques', *Experiments in Fluids* **15**(6), 431–442. doi: 10.1007/BF00191786.

Bareiß, R. and Wagner, S. (1993), The free wake/hybrid wake code ROVLM - a tool for aerodynamic analysis of wind turbines, *in* 'Proceedings of the European Community Wind Energy Conference', Lübeck-Travemünde, Germany, pp. 424–427.

Barthelmie, R. J., Courtney, M. S., Højstrup, J. and Larsen, S. E. (1996), 'Meteorological aspects of offshore wind energy: Observations from the vindeby wind farm', *Journal of Wind Engineering and Industrial Aerodynamics* **62**(2-3), 191–211. doi: 10.1016/S0167-6105(96)00077-3.

Barthelmie, R. J., Folkerts, L., Larsen, G. C., Rados, K., Pryor, S. C., Frandsen, S. T., Lange, B. and Schepers, G. (2006), 'Comparison of wake model simulations with offshore wind turbine wake profiles measured by sodar', *Journal of Atmospheric and Oceanic Technology* **23**(7), 888–901. doi: 10.1175/JTECH1886.1.

Barthelmie, R. J., Pryor, S. C., Frandsen, S. T., Hansen, K. S., Schepers, J. G., Rados, K., Schlez, W., Neubert, A., Jensen, L. E. and Neckelmann, S. (2010), 'Quantifying the impact of wind turbine wakes on power output at offshore wind farms', *Journal of Atmospheric and Oceanic Technology* **27**(8), 1302–1317. doi: 10.1175/2010JTECHA1398.1.

Barthelmie, R., Larsen, G., Pryor, S., Jørgensen, H., Bergström, H., Schlez, W., Rados, K., Lange, B., Vølund, P., Neckelmann, S., Mogensen, S., Schepers, G., Hegberg, G., Folkerts, L. and Magnusson, M. (2004), 'Endow (efficient development of offshore wind farms): modelling wake and boundary layer interactions', *Wind Energy* **7**(3), 225–245. doi: 10.1002/we.121.

Bruun, H. (1995), *Hot-wire anemometry: principles and signal analysis*, Oxford University Press, Oxford, UK. ISBN: 0-19-856342-6.

Burton, T., Jenkins, N., Sharpe, D. and Bossanyi, E. (2011), *Wind Energy Handbook*, Wiley, Chichester, UK. ISBN: 0470699752.

Chen, T. and Liou, L. (2011), 'Blockage corrections in wind tunnel tests of small horizontal-axis wind turbines', *Experimental Thermal and Fluid Science* **35**(3), 565 – 569. doi: 10.1016/j.expthermflusci.2010.12.005.

Chu, C.-R. and Chiang, P.-H. (2014), 'Turbulence effects on the wake flow and power production of a horizontal-axis wind turbine', *Journal of Wind Engineering and Industrial Aerodynamics* **124**(0), 82–89. doi: 10.1016/j.jweia.2013.11.001.

Connell, J. (1988), 'A primer of turbulence at the wind turbine rotor', *Solar Energy* **41**(3), 281–293. doi: 10.1016/0038-092X(88)90146-6.

Coton, F. N. and Wang, T. (1999), 'The prediction of horizontal axis wind turbine performance in yawed flow using an unsteady prescribed wake model',

Proceedings of the Institution of Mechanical Engineers **213**(1), 33–43. doi: 10.1243/0957650991537419.

Crespo, A. and Hernández, J. (1996), 'Turbulence characteristics in wind-turbine wakes', *Journal of Wind Engineering and Industrial Aerodynamics* **61**(1), 71–85. doi: 10.1016/0167-6105(95)00033-X.

Crespo, A., Hernández, J. and Frandsen, S. (1999), 'Survey of modelling methods for wind turbine wakes and wind farms', *Wind Energy* **2**(1), 1–24. doi: 10.1002/(SICI)1099-1824(199901/03)2:1¡1::AID-WE16¿3.0.CO;2-7.

Dahlberg, J., Poppen, M. and Thor, S. (1992), 'Load/fatigue effects on a wind turbine generator in a wind farm', *Journal of Wind Engineering and Industrial Aerodynamics* **39**(13), 199 – 209. doi: 10.1016/0167-6105(92)90546-M.

Department of Energy & Climate Change (2013), 'UK renewable energy roadmap: 2013 update'.

Devinant, P., Leroy, A. and Mudry, M. (1999), 'Unsteady 3d nonlinear kutta-joukovski condition for thin lifting surfaces', *Computational Mechanics* **24**(2), 138–147. doi: 10.1007/s004660050446.

Dowling, N. (1971), Fatigue failure predictions for complicated stress-strain histories, T. & A. M. Report 337, Deptartment of Theoretical and Applied Mechanics, University of Illinois, Urbana, IL, USA.

Downing, S. and Socie, D. (1982), 'Simple rainflow counting algorithms', *International Journal of Fatigue* **4**(1), 31–40. doi: 10.1016/0142-1123(82)90018-4.

Drela, M. (1999), Integrated simulation model for preliminary aerodynamic, structural, and control-law design of aircraft, *in* '40th Structures, Structural Dynamics, and Materials Conference and Exhibit', American Institute of Aeronautics and Astronautics. doi: 10.2514/6.1999-1394.

Drela, M. and Youngren, H. (2014), 'Athena vortex lattice code (version 3.35)', http://web.mit.edu/drela/Public/web/avl/. Last modified 23.02.2014; accessed 15.05.2014.

Duckworth, A. and Barthelmie, R. (2008), 'Investigation and validation of wind turbine wake models', *Wind Engineering* **32**(5), 459–475. doi: 10.1260/030952408786411912.

Dumitrescu, H. and Frunzulică, F. (2004), A free-wake aerodynamic model for helicopter rotors, *in* 'Proceedings of the Romanian Academy', Vol. 5, The Romanian Academy.

Ebert, P. and Wood, D. (1997), 'The near wake of a model horizontal-axis wind turbinei. experimental arrangements and initial results', *Renewable Energy* **12**(3), 225–243. doi: 10.1016/S0960-1481(97)00046-3.

Ebert, P. and Wood, D. (1999), 'The near wake of a model horizontal-axis wind turbineii. general features of the three-dimensional flowfield', *Renewable Energy* **18**(4), 513–534. doi: 10.1016/S0960-1481(98)00797-6.

Ebert, P. and Wood, D. (2001), 'The near wake of a model horizontal-axis wind turbine: Part 3: properties of the tip and hub vortices', *Renewable Energy* **22**(4), 461–472. doi: 10.1016/S0960-1481(00)00096-3.

Elliott, D. (1991), Status of wake and array loss research, *in* 'Presented at the 21st American Wind Energy Association Conference: Windpower 1991', Palm Springs, CA, pp. 24–27.

Elliott, D. and Barnard, J. (1990), 'Observations of wind turbine wakes and surface roughness effects on wind flow variability', *Solar Energy* **45**(5), 265–283. doi: 10.1016/0038-092X(90)90012-2.

European Parliament and Council of the European Union (2009), 'Directive 2009/28/EC'.

Fiddes, S. and Gaydon, J. (1996), 'A new vortex lattice method for calculating the flow past yacht sails', *Journal of Wind Engineering and Industrial Aerodynamics* **63**(13), 35–59. doi: 10.1016/S0167-6105(96)00068-2.

Fletcher, T. M. and Brown, R. E. (2010), 'Simulation of wind turbine wake interaction using the vorticity transport model', *Wind Energy* **13**(7), 587–602. doi: 10.1002/we.379.

Frandsen, S. (1996), Fatigue loading on offshore wind power stations, *in* A. Zervos, H. Ehmann and P. Helm, eds, '1996 European Union Wind Energy Conference', H.S. Stephens & Associates, Göteborg Sweden, pp. 990–994. ISBN: 0-9521452-9-4.

Frandsen, S., Barthelmie, R., Pryor, S., Rathmann, O., Larsen, S., Højstrup, J. and Thøgersen, M. (2006), 'Analytical modelling of wind speed deficit in large offshore wind farms', *Wind Energy* **9**(1-2), 39–53. doi: 10.1002/we.189.

Froude, R. E. (1889), 'On the part played in propulsion by differences of fluid pressure', *Transactions of the Institution of Naval Architects* **30**, 390–405.

Garrick, I. E. (1936), Propulsion of a flapping and oscillating aerofoil, Technical Report 567, National Advisory Committee for Aeronautics.

Garrick, I. E. (1938), On some reciprocal relations in the theory of nonstationary flows, Technical Report 629, National Advisory Committee for Aeronautics.

Giannakidis, G. and Graham, J. (1996), Prediction of H. A. W. T. blade stall and performance, *in* A. Zervos, H. Ehmann and P. Helm, eds, '1996 European Union Wind Energy Conference', H.S. Stephens & Associates, Göteborg Sweden, pp. 699–702. ISBN: 0-9521452-9-4.

González-Longatt, F., Wall, P. and Terzija, V. (2012), 'Wake effect in wind farm performance: Steady-state and dynamic behavior', *Renewable Energy* **39**(1), 329–338. doi: 10.1016/j.renene.2011.08.053.

Gouder, K. (2014), Private Communication.

Graham, J. (1971), 'A lifting-surface theory for the rectangular wing in nonstationary flow', *The Aeronautical Quarterly* **22**(1), 83–100.

Graham, J. (1976), 'Turbulent flow past a porous plate', *Journal of Fluid Mechanics* **73**(3), 565–591. doi: 10.1017/S002211207600150X.

Graham, J. (1983), 'The lift on an aerofoil in starting flow', *Journal of Fluid Mechanics* **133**(8), 413–425. doi: 10.1017/S0022112083001986.

Grant, I., Liu, G. H. S. A., Infield, D. and Eich, T. (1991), Particle image velocimetry measurements of the aerodynamics of a wind turbine, *in* 'International Congress on Instrumentation in Aerospace Simulation Facilities, 1991', pp. 314–320. doi: 10.1109/ICIASF.1991.186254.

Grant, I., Mo, M., Pan, X., Parkin, P., Powell, J., Reinecke, H., Shuang, K., Coton, F. and Lee, D. (2000), 'An experimental and numerical study of the vortex filaments in the wake of an operational, horizontal-axis, wind turbine', *Journal of Wind Engineering and Industrial Aerodynamics* **85**(2), 177–189. doi: 10.1016/S0167-6105(99)00139-7.

Hansen, A. and Butterfield, C. (1993), 'Aerodynamics of horizontal-axis wind turbines', *Annual Review of Fluid Mechanics* **25**(1), 115–149. doi: 10.1146/annurev.fl.25.010193.000555.

Harris, R. I. (1970), The nature of the wind, *in* 'The Modern Design of Wind-Sensitive Structures', The Institution of Civil Engineers, London, UK, pp. 29–55.

Hassan, U., Taylor, G. and Garrad, A. (1988), 'The dynamic response of wind turbines operating in a wake flow', *Journal of Wind Engineering and Industrial Aerodynamics* **27**(13), 113–126. doi: 10.1016/0167-6105(88)90028-1.

Hiester, T. R. and Pennell, W. T. (1981), The meteorological aspects of siting large wind turbines, Technical Report PNL-2522, Battelle Pacific Northwest Laboratory, Richland, WA, USA. doi: 10.2172/6657537.

Högström, U., Asimakopoulos, D., Kambezidis, H., Helmis, C. and Smedman, A. (1988), 'A field study of the wake behind a 2 MW wind turbine', *Atmospheric Environment (1967)* **22**(4), 803–820. doi: 10.1016/0004-6981(88)90020-0.

Højstrup, J. (1999), 'Spectral coherence in wind turbine wakes', *Journal of Wind Engineering and Industrial Aerodynamics* **80**(12), 137–146. doi: 10.1016/S0167-6105(98)00198-6.

Hurst, D. and Vassilicos, J. C. (2007), 'Scalings and decay of fractal-generated turbulence', *Physics of Fluids (1994-present)* **19**(3), 035103. doi: 10.1063/1.2676448.

Imperial College London (2012), 'Honda wind tunnnel specification', http://www3.imperial.ac.uk/hondawindtunnel/aboutthetunnel/specification. Accessed 09.03.2012.

Infield, D. G., Grant, I., Smith, G. and Wang, X. (1994), Further development of particle image velocimetry (piv) for flow measurements around operational wind turbine rotors, *in* 'Proceedings of the European Community Wind Energy Conference', Thesaloniki, Greece, pp. 262–267.

Infield, D. G., Smith, G. H. and Grant, I. (1993), The measurement of flow around an operational wind turbine using particle image velocimetry, *in* 'Proceedings of the European Community Wind Energy Conference', Lübeck-Travemünde, Germany, pp. 367–370.

Jørgensen, F. E. (2002), How to measure turbulence with hot-wire anemometers - a practical guide, Technical Report 9040U6151, Dantec Dynamcs.

Kaimal, J. C., Wyngaard, J. C., Izumi, Y. and Coté, O. R. (1972), 'Spectral characteristics of surface-layer turbulence', *Quarterly Journal of the Royal Meteorological Society* **98**(417), 563–589. doi: 10.1002/qj.49709841707.

Katic, I., Hjstrup, J. and Jensen, N. (1987), A simple model for cluster efficiency, *in* W. Palz and E. Sesto, eds, 'EWEC'86. Proceedings.', Vol. 1, A. Raguzzi, Rome, pp. 407–410.

Katz, J. and Plotkin, A. (2001), *Low-Speed Aerodynamics*, Second edn, Cambridge University Press, New York, USA. ISBN: 978-0-521-66552-0.

Kiranoudis, C. and Maroulis, Z. (1997), 'Effective short-cut modelling of wind park efficiency', *Renewable Energy* **11**(4), 439–457. doi: 10.1016/S0960-1481(97)00011-6.

Kjaer, C., Douglas, B., Bianchin, R. and Zander, E., eds (2009), *Wind Energy–the Facts: A Guide to the Technology, Economics and Future of Wind Power*, Earthscan, Chapter 1. ISBN: 978-1-84407-710-6. [Online] Available at: `www.wind-energy-the-facts.org` [Accessed: 15-04-2014].

Kristensen, L. and Jensen, N. (1979), 'Lateral coherence in isotropic turbulence and in the natural wind', *Boundary-Layer Meteorology* **17**(3), 353–373. doi: 10.1007/BF00117924.

Lamb, H. (1945), *Hydrodynamics*, sixth edn, Dover Publications, Chapter 7.

Larsen, G. C., Højstrup, J. and Madsen, H. A. (1996), Wind fields in wakes, *in* A. Zervos, H. Ehmann and P. Helm, eds, '1996 European Union Wind Energy Conference', H.S. Stephens & Associates, Göteborg Sweden, pp. 764–768. ISBN: 0-9521452-9-4.

Larsen, G. C., Madsen, H. A., Bingöl, F., Mann, J., Ott, S., Sørensen, J. N., Okulov, V., Troldborg, N., Nielsen, M., Thomsen, K., Larsen, T. J. and Mikkelsen, R. (2007), Dynamic wake meandering modeling, Report Risø-R-1607(EN), Risø National Laboratory.

Lee, S., Churchfield, M. J., Moriarty, P. J., Jonkman, J. and Michalakes, J. (2013), 'A numerical study of atmospheric and wake turbulence impacts on wind turbine fatigue loadings', *Journal of Solar Energy Engineering* **135**(3), 031001. doi: 10.1115/1.4023319.

Leishman, J. G. (2002), 'Challenges in modelling the unsteady aerodynamics of wind turbines', *Wind Energy* **5**(2-3), 85–132. doi: 10.1002/we.62.

Leishman, J. G. (2006), *Principles of Helicopter Dynamics*, Cambridge Aerospace Series, second edn, Cambridge University Press, New York, USA. ISBN: 978-0-521-85860-1.

Leithead, W. E. and Watson, S. (2009), Report on current and possible future wind turbine configurations, Deliverable DW.2.1, SUPERGEN Wind.

Lissaman, P. B. S. (1979), 'Energy effectiveness of arbitrary arrays of wind turbines', *Journal of Energy* **3**(6), 323–328. doi: 10.2514/3.62441.

Lubitz, W. D. (2014), 'Impact of ambient turbulence on performance of a small wind turbine', *Renewable Energy* **61**(0), 69–73. doi: 10.1016/j.renene.2012.08.015. World Renewable Energy Congress - Sweden, 8-13 May, 2011, Linköping, Sweden.

Machefaux, E., Troldborg, N., Larsen, G., Mann, J. and Aagaard Madsen, H. (2012), Experimental and numerical study of wake to wake interaction in wind farms, *in* 'Proceedings of EWEA 2012 - European Wind Energy Conference & Exhibition', Vol. 1, European Wind Energy Association.

Mack, S., Brehm, C., Heine, B., Kurz, A. and Fasel, H. (2008), Experimental investigation of separation and separation control on a laminar airfoil, *in* '4th Flow Control Conference', Fluid Dynamics and Co-located Conferences, Seattle, WA, USA., p. 3766. doi: 10.2514/6.2008-3766.

Madsen, H. A. and Paulsen, U. S. (1990), An integrated rotor and turbulent wake model compared with experiment, *in* 'European Community Wind Energy Conference', Madrid, Spain, pp. 269–273.

Maeda, T., Yokota, T., Shimizu, Y. and Adachi, K. (2004), 'Wind tunnel study of the interaction between two horizontal axis wind turbines', *Wind Engineering* **28**(2), 197–212. doi: 10.1260/0309524041211396.

Magnusson, M. (1996), A new approach for evaluating measured wake data, *in* A. Zervos, H. Ehmann and P. Helm, eds, '1996 European Union Wind Energy Conference', H.S. Stephens & Associates, Göteborg Sweden, pp. 813–816. ISBN: 0-9521452-9-4.

Magnusson, M. and Smedman, A.-S. (1999), 'Air flow behind wind turbines', *Journal of Wind Engineering and Industrial Aerodynamics* **80**(12), 169–189. doi: 10.1016/S0167-6105(98)00126-3.

Mann, J. (1998), 'Wind field simulation', *Probabilistic Engineering Mechanics* **13**(4), 269–282. doi: 10.1016/S0266-8920(97)00036-2.

MATLAB (R2013b) (2013), *version 8.2.0.701*, The MathWorks Inc., Natick, Massachusetts, USA.

McKay, P., Carriveau, R. and Ting, D. S.-K. (2013), 'Wake impacts on downstream wind turbine performance and yaw alignment', *Wind Energy* **16**(2), 221–234. doi: 10.1002/we.544.

McNae, D. M. (2013), Unsteady Hydrodynamics of Tidal Stream Turbines, PhD Thesis, Imperial College London, London, UK.

Packard, N. O. (2012), Active Flow Separation Control of a Laminar Airfoil at Low Reynolds Number, PhD Thesis, The Ohio State University.

Pascheke, F. and Hancock, P. E. (2008), Wake development and interactions within an array of large wind turbines, *in* 'European Wind Energy Conference and Exhibition 2008', Vol. 6, European Wind Energy Association, pp. 3008–3016.

Pesmajoglou, S. D. and Graham, J. (2000), 'Prediction of aerodynamic forces on horizontal axis wind turbines in free yaw and turbulence', *Journal of Wind Engineering and Industrial Aerodynamics* **86**(1), 1–14. doi: 10.1016/S0167-6105(99)00125-7.

Platt, A. (2012), 'NWTC design codes (WT_Perf)', http://wind.nrel.gov/designcodes/simulators/wtperf/. Last modified 26.11.2012; accessed 09.02.2014.

Porté-Agel, F., Wu, Y.-T., Lu, H. and Conzemius, R. J. (2011), 'Large-eddy simulation of atmospheric boundary layer flow through wind turbines and wind farms', *Journal of Wind Engineering and Industrial Aerodynamics* **99**(4), 154–168. doi: 10.1016/j.jweia.2011.01.011.

Rados, K., Larsen, G., Barthelmie, R., Schlez, W., Lange, B., Schepers, G., Hegberg, T. and Magnisson, M. (2001), 'Comparison of wake models with data for offshore wind farms', *Wind Engineering* **25**(5), 271–280. doi: 10.1260/030952401760177846.

Ragan, P. and Manuel, L. (2007), 'Comparing estimates of wind turbine fatigue loads using time-domain and spectral methods', *Wind Engineering* **31**(2), 83–99. doi: 10.1260/030952407781494494.

Rathmann, O., Barthelmie, R. and Frandsen, S. (2006), Turbine wake model for wind resource software, *in* 'European Wind Energy Conference', Athens, Greece.

Riziotis, V. A. and Voutsinas, S. G. (2000), 'Fatigue loads on wind turbines of different control strategies operating in complex terrain', *Journal of Wind Engineering and Industrial Aerodynamics* **85**(3), 211–240. doi: 10.1016/S0167-6105(99)00127-0.

Robison, D. J., Coton, F. N., Galbraith, R. A. M. and Vezza, M. (1995), 'Application of a prescribed wake aerodynamic prediction scheme to horizontal axis wind turbines in axial flow', *Wind Engineering* **19**(1), 41–51.

Rohatgi, J. and Barbezier, G. (1999), 'Wind turbulence and atmospheric stability - their effect on wind turbine output', *Renewable Energy* **16**(1-4), 908–911. doi: 10.1016/S0960-1481(98)00308-5.

Rossow, V. J. (1995), 'Validation of vortex-lattice method for loads on wings in lift-generated wakes', *Journal of Aircraft* **32**(6), 1254–1262. doi: 10.2514/3.46872.

Rychlik, I. (1987), 'A new definition of the rainflow cycle counting method', *International Journal of Fatigue* **9**(2), 119–121. doi: 10.1016/0142-1123(87)90054-5.

Sanderse, B. (2009), Aerodynamics of wind turbine wakes, Technical Report ECN-E-09-016, ECN.

Saranyasoontorn, K., Manuel, L. and Veers, P. S. (2004), 'A comparison of standard coherence models for inflow turbulence with estimates from field measurements', *Journal of Solar Energy Engineering* **126**(4), 1069–1082. doi: 10.1115/1.1797978.

Schepers, J. G. (2003), ENDOW: Validation and improvement of ECNs wake model, Technical Report ECN-C-03-034, ECN.

Schepers, J. G. and van der Pijl, S. P. (2007), 'Improved modelling of wake aerodynamics and assessment of new farm control strategies', *Journal of Physics: Conference Series* **75**(1), 012039. doi: 10.1088/1742-6596/75/1/012039.

Schlez, W. and Infield, D. (1998), 'Horizontal, two point coherence for separations greater than the measurement height', *Boundary-Layer Meteorology* **87**(3), 459–480. doi: 10.1023/A:1000997610233.

Schlipf, D., Trabucchi, D., Bischoff, O., Hofsäß, M., Mann, J., Mikkelsen, T., Rettenmeier, A., Trujillo, J. J. and Kuhn, M. (2010), 'Testing of frozen turbulence hypothesis for wind turbine applications with a scanning lidar system', ISARS, Paris, France.

Scully, M. (1975), Computation of helicopter rotor wake geometry and its influence on rotor harmonic airloads, PhD Thesis, Massachusetts Institute of Technology, Department of Aeronautics and Astronautics. doi: 1721.1/64826.

Seydel, J. and Aliseda, A. (2013), 'Wind turbine performance in shear flow and in the wake of another turbine through high fidelity numerical simulations with moving mesh technique', *Wind Energy* **16**(1), 123–38. doi: 10.1002/we.535.

Simoes, F. J. and Graham, J. M. R. (1992), 'Application of a free vortex wake model to a horizontal axis wind turbine', *Journal of Wind Engineering and Industrial Aerodynamics* **39**(1-3), 129–138. doi: 10.1016/0167-6105(92)90539-M.

Simpson, R. J. S., Palacios, R. and Murua, J. (2013), 'Induced-drag calculations in the unsteady vortex lattice method', *AIAA Journal* **51**(7), 1775–1779. doi: 10.2514/1.J052136.

Snel, H. (1998), 'Review of the present status of rotor aerodynamics', *Wind Energy* **1**(S1), 46–69. doi: 10.1002/(SICI)1099-1824(199804)1:1+%3C46::AID-WE3%3E3.3.CO;2-0.

Snel, H. (2003), 'Review of aerodynamics for wind turbines', *Wind Energy* **6**(3), 203–211. doi: 10.1002/we.97.

Snel, H. and Schepers, J. (1992), 'Engineering moles for dynamic inflow phenomena', *Journal of Wind Engineering and Industrial Aerodynamics* **39**(1-3), 267–281. doi: 10.1016/0167-6105(92)90552-L.

Solari, G. (1987), 'Turbulence modeling for gust loading', *Journal of Structural Engineering* **113**(7), 1550–1569. doi: 10.1061/(ASCE)0733-9445(1987)113:7(1550).

Sørensen, J. N. and Shen, W. Z. (2002), 'Numerical modeling of wind turbine wakes', *Journal of Fluids Engineering* **124**(2), 393–399. doi: 10.1115/1.1471361.

Sørensen, J. N., Shen, W. Z. and Munduate, X. (1998), 'Analysis of wake states by a full-field actuator disc model', *Wind Energy* **1**(2), 73–88. doi: 10.1002/(SICI)1099-1824(199812)1:2¡73::AID-WE12¿3.0.CO;2-L.

Sørensen, N. N. and Madsen, H. A. (2006), Modelling of transient wind turbine loads during pitch motion, *in* '2006 European Wind Energy Conference and Exhibition', Athens, Greece.

Spiegel, M. R. (1968), *Mathematical Handbook of Formulas and Tables*, Schaum's outline series, McGraw-Hill, New York, USA.

Stefanatos, N. C., A. B, K. and Voutsinas, S. G. (1996), Interaction of wind turbine wakes, *in* A. Zervos, H. Ehmann and P. Helm, eds, '1996 European Union Wind Energy Conference', H.S. Stephens & Associates, Göteborg Sweden. ISBN: 0-9521452-9-4.

Sutherland, H. J. and Osgood, R. M. (1992), Frequency-domain synthesis of the fatigue load spectrum for the NPS 100 kW wind turbine, *in* 'Presented at the Windpower 1992', Seattle, WA, pp. 19–23.

Taylor, G. (1938), The spectrum of turbulence, *in* 'Proceedings of the Royal Society of London', Vol. 164 of *Series A, Mathematical and Physical Sciences*, pp. 476–490. doi: 10.1098/rspa.1938.0032.

The Crown Estate (2012), Offshore wind cost reduction pathways study, Pathways study, The Crown Estate, London, UK.

Theodorsen, T. (1935), General theory of aerodynamic instability and the mechanism of flutter, Technical Report 496, National Advisory Committee for Aeronautics.

Thomsen, K. and Madsen, H. A. (2005), 'A new simulation method for turbines in wake-applied to extreme response during operation', *Wind Energy* **8**(1), 35–47. doi: 10.1002/we.130.

Thomsen, K. and Sørensen, P. (1999), 'Fatigue loads for wind turbines operating in wakes', *Journal of Wind Engineering and Industrial Aerodynamics* **80**(1-2), 121–136. doi: 10.1016/S0167-6105(98)00194-9.

Thomson, W. (Lord Kelvin) (1869), 'On vortex motion.', *Transactions of the Royal Society of Edinburgh* **25**, 217–260.

Tol, P. (2012), Colour schemes, Technical Note SRON/EPS/TN/09-002, SRON Netherlands Institute for Space Research.

Troldborg, N., Larsen, G. C., Madsen, H. A., Hansen, K. S., Sørensen, J. N. and Mikkelsen, R. (2011), 'Numerical simulations of wake interaction between two wind turbines at various inflow conditions', *Wind Energy* **14**(7), 859–876. doi: 10.1002/we.433.

Troldborg, N., Sorensen, J. N. and Mikkelsen, R. (2010), 'Numerical simulations of wake characteristics of a wind turbine in uniform inflow', *Wind Energy* **13**(1), 86–99. doi: 10.1002/we.345.

Van der Hoven, I. (1957), 'Power spectrum of horizontal wind speed in the frequency range from 0.0007 to 900 cycles per hour', *Journal of Meteorology* **14**(2), 160–164. doi: 10.1175/1520-0469(1957)014¡0160:PSOHWS¿2.0.CO;2.

Vatistas, G., Kozel, V. and Mih, W. (1991), 'A simpler model for concentrated vortices', *Experiments in Fluids* **11**(1), 73–76. doi: 10.1007/BF00198434.

Veers, P. S. (1984), Modeling stochastic wind loads on vertical axis wind turbines, Technical Report SAND-83-1909, Sandia National Labs., Albuquerque, NM, USA.

Veers, P. S. (1988), Three-dimensional wind simulation, Technical Report SAND-88-0152, Sandia National Labs., Albuquerque, NM, USA.

Vermeer, L. J. (2001), A review of wind turbine wake research at TU Delft, *in* '20th 2001 ASME Wind Energy Symposium', Aerospace Sciences Meetings, American Institute of Aeronautics and Astronautics, Reno, NV, USA, pp. 103–113. doi: 10.2514/6.2001-30.

Vermeer, L., Sørensen, J. and Crespo, A. (2003), 'Wind turbine wake aerodynamics', *Progress in Aerospace Sciences* **39**(6-7), 467–510. doi: 10.1016/S0376-0421(03)00078-2.

Vølund, P. (1992), 'Loads on a horizontal axis wind turbine operating in wake', *Journal of Wind Engineering and Industrial Aerodynamics* **39**(13), 317–328. doi: 10.1016/0167-6105(92)90556-P.

von Helmholtz, H. (1978), 'On integrals of the hydrodynamic equations that correspond to vortex motions', Translated from the German, by Parpart, U., *International Journal of Fusion Energy* **1**(3-4), 41–68. (Originally published in 1858 in the *Journal für die reine and angewandte Mathematik* **55**, 25-55).

von Kármán, T. (1948), 'Progress in the statistical theory of turbulence', *Proceedings of the National Academy of Sciences* **34**(11), 530–539.

Vries, O. (1983), 'On the theory of the horizontal-axis wind turbine', *Annual Review of Fluid Mechanics* **15**(1), 77–96. doi: 10.1146/annurev.fl.15.010183.000453.

Whale, J., Anderson, C., Bareiss, R. and Wagner, S. (2000), 'An experimental and numerical study of the vortex structure in the wake of a wind turbine', *Journal of Wind Engineering and Industrial Aerodynamics* **84**(1), 1–21. doi: 10.1016/S0167-6105(98)00201-3.

Whale, J., Barei"s, R., Wagner, S. and Anderson, C. (1996), The wake structure of a wind turbine - comparison between PIV measurements and free-wake calculations, *in* A. Zervos, H. Ehmann and P. Helm, eds, '1996 European Union Wind Energy

Conference', H.S. Stephens & Associates, Göteborg Sweden, pp. 695–698. ISBN: 0-9521452-9-4.

Yang, Z., Sarkar, P. and Hu, H. (2011), An experimental investigation on the wake characteristics of a wind turbine in an atmospheric boundary layer wind, *in* '29th AIAA Applied Aerodynamics Conference', American Institute of Aeronautics and Astronautics. doi: 10.2514/6.2011-3815.

A Calibrations

In the following appendix, the process and results of the various calibrations used in analysing the experimental data are presented. Each calibration consists of the acquisition of a mean value of a signal at a known set point.

The statistical RMS error of a sample is given by:

$$\%\epsilon = \frac{z_\alpha}{\sqrt{N}} \tag{A.1}$$

Where N is the number of samples and the confidence parameter $z_\alpha = 2.57$ for 99% confidence. Unless otherwise stated, in each of the following calibrations $N = 2^{16} = 65536$ samples were recorded per data point. Consequently, the statistical error is 1%.

A.1 Strain gauges

The calibration of a strain gauge bridge is achieved by recording the mean of the voltage signal due to an applied moment, given by suspending a known mass at a known radial position. In all cases a sampling rate of 200 Hz was used in accordance with the experimental procedure.

A.1.1 Blade

The blade root strain gauge bridge was calibrated via the T24-SA wireless strain gauge amplifier using masses of $2 - 50$ g located from $50 - 100$ mm from the centre of the gauge pattern. The combinations of mass and location are listed in Table A.1. Positive bending moment is defined for forces acting in the direction of the free stream velocity.

After processing the experimental data, it became evident that the original strain gauge calibrations did not cover the entire range of readings. Hence a final calibration was taken on the 14-02-2014, augmenting the previous ones with additional

masses of 100 g and 200 g. Due to time limitations, the number of samples was reduced to $N = 2^{14} = 16384$, yielding a statistical error of 2%.

Each of the masses was calibrated using a Mettler PM1200 precision balance (max: 1200 g ±0.001 g) , with the exception of the 100 g mass which was checked using a Mettler Toledo AG245 precision balance (max: 210 g ±0.0001 g); confirming that all measurements are within ±0.03 g. The locations were marked with an accuracy of ±1 mm. Consequently, the measurement error is 0.29×10^{-6} N m.

Mass (kg)	Position (m)		
	0.05	0.10	0.15
0.002	0.10×10^{-3}	0.20×10^{-3} ‡	0.30×10^{-3} ‡
0.005	0.25×10^{-3}	0.50×10^{-3} ‡	0.75×10^{-3} ‡
0.020	1.00×10^{-3}	2.00×10^{-3}	3.00×10^{-3} ‡
0.050	2.50×10^{-3}	5.00×10^{-3} ‡	7.50×10^{-3} ‡
0.100†	5.00×10^{-3}	-	-
0.200†	10.00×10^{-3}	20.00×10^{-3}	$30. \times 10^{-3}$

† Additional data points for 14-02-2014 calibration; ‡ Not included in 14-02-2014 calibration

Table A.1: Blade calibration load points.

The resulting calibration curves are shown in Figure A.1. As expected for a full bridge strain gauge the response is linear in all cases. Applying a linear least squares fit of the form

$$y = mx + c$$

gives $-1.17 < m < -1.19$ and $-5.26 \times 10^{-5} < c < 5.05 \times 10^{-4}$, where the higher magnitude values correspond to the less accurate calibration on the 14-02-2014. As the purpose of this later run was to confirm the linear response, the original calibrations are used in the conversion of the experimental data as they exhibit less disparity.

In order to identify the resonant frequency of the blade, an additional sample set was taken whilst the blade was excited by an impulse type forcing, i.e. the blade was

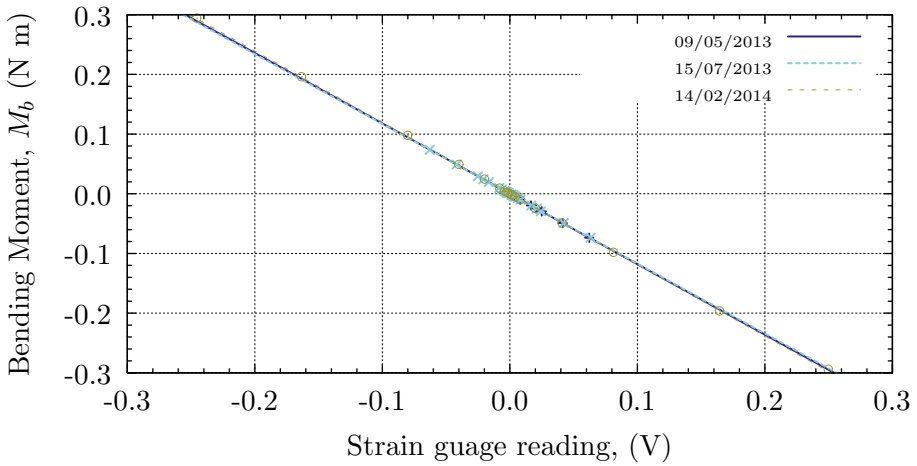


Figure A.1: Blade strain gauge calibration.

tapped with an allen key to excite the resonance. Figure A.2 shows the resulting spectrum, clearly indicating the blade resonance at $f_b = 85.4$ Hz.

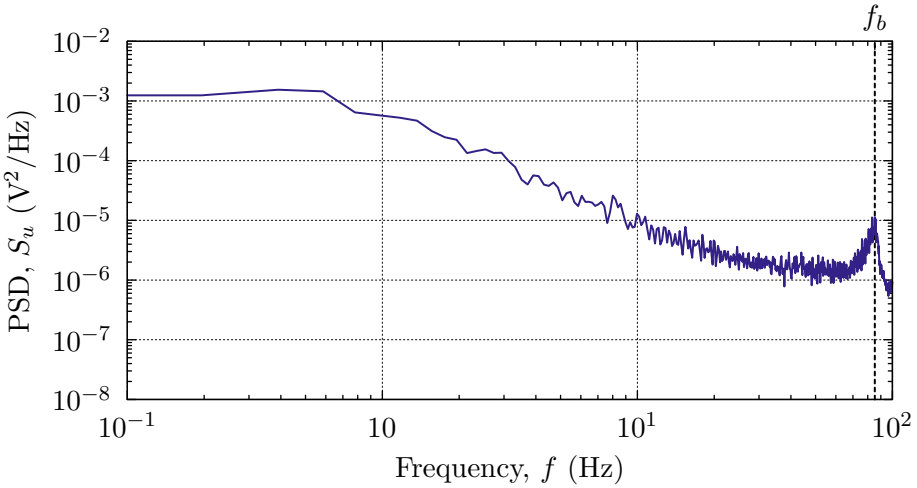


Figure A.2: Blade resonance spectrum.

A.1.2 Strut

The strut strain gauge bridge was calibrated via a Flyde 379TA strain gauge amplifier using masses of 0.2 kg, 1.0 kg and 2.0 kg located 100 mm, 200 mm and 300 mm from the centre of the gauge pattern. The measurement error is the same as for the blade strain gauge. Positive bending moment is defined for forces acting in the direction of the free stream velocity. The resulting calibration curve is shown in Figure A.3. Using a linear least squares fit gives $m = 21.12$ and $c = 3.69 \times 10^{-3}$.

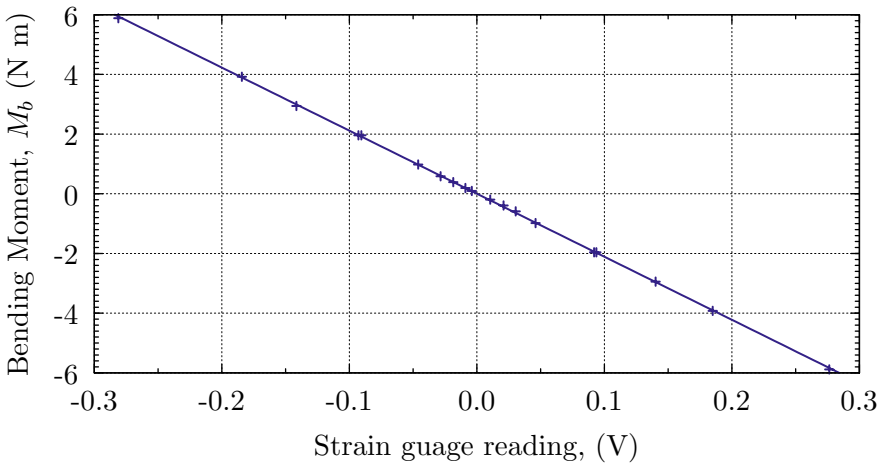


Figure A.3: Strut strain gauge calibration.

Again, the resonant frequency of the strut was identified using an impulse excitation. Figure A.4 shows the resulting spectrum. The strut resonance is clearly identified at $f_s = 9.57$ Hz. It is also noted that there is a clear peak at the grid frequency of $f_g = 50$ Hz, although this is several orders of magnitude smaller than the resonance.

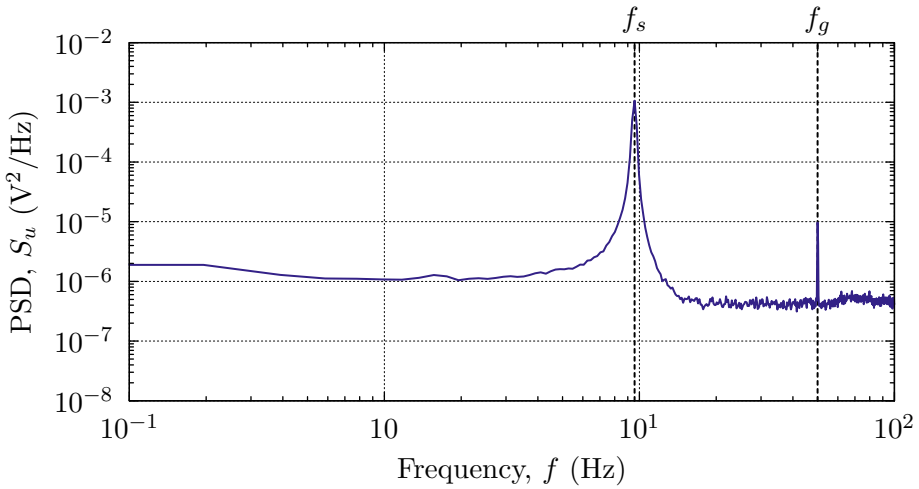


Figure A.4: Strut resonance spectrum.

A.2 Hot-wire

The hot-wires were calibrated against a pitot positioned in close proximity. A preliminary measurement of the mean reading was conducted to determine whether the presence of the pitot accelerated the flow past the hot-wires. The reading at 50 mm separation was found to match that without the pitot tube present. At 0.25

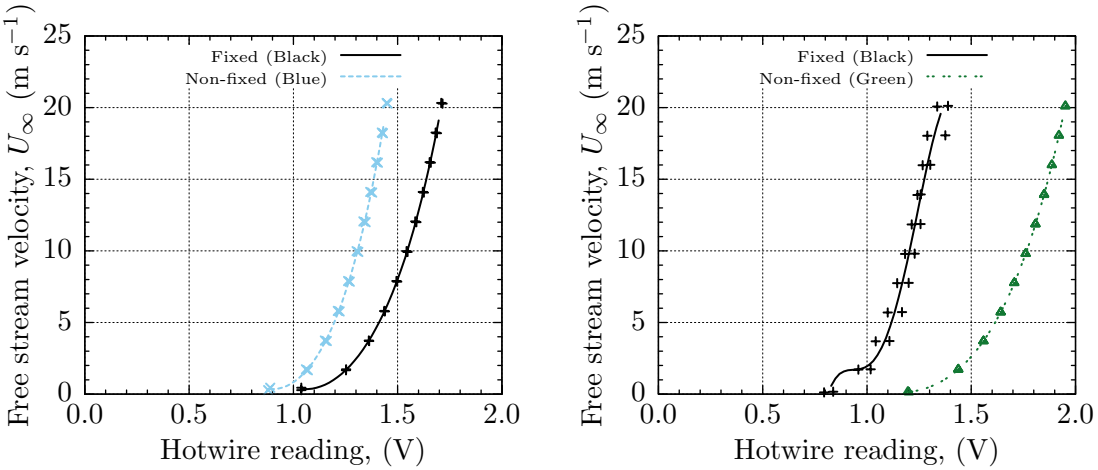
mm separation, corresponding to placing the pitot between the two hot-wire probes, there was a 0.25% increase in the voltage reading. Therefore, the pitot was mounted at hub height, 50 mm from the fixed hot-wire probe, on the opposite side to the non-fixed probe. The tunnel voltage was incremented from 0 to 5 V in 0.5 V steps, corresponding to approximately $0-20$ m s^{-1}, and recordings taken from each of the hot-wires and the pitot tube at each increment after allowing the tunnel velocity to settle.

The calibration process is repeated at the end of each set of measurements. The data is corrected for temperature fluctuations according to Equation 4.3 in Section 4.2. A polynomial curve of the form

$$U = C_0 + C_1 E_c + C_2 E_c^2 + C_3 E_c^3 + C_4 E_c^4$$

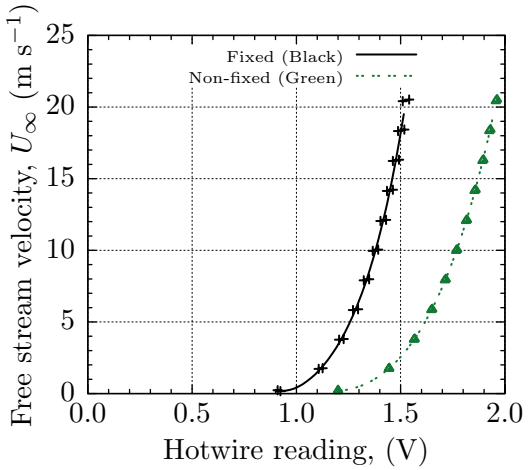
where E_c is the corrected voltage, is then fitted to the results to give a calibration curve for each run (Jørgensen, 2002).

Figures A.5 to A.8 show the calibrations for each of the hot-wire wake measurements. Figure A.9 shows the calibration for the wake meandering measurements.

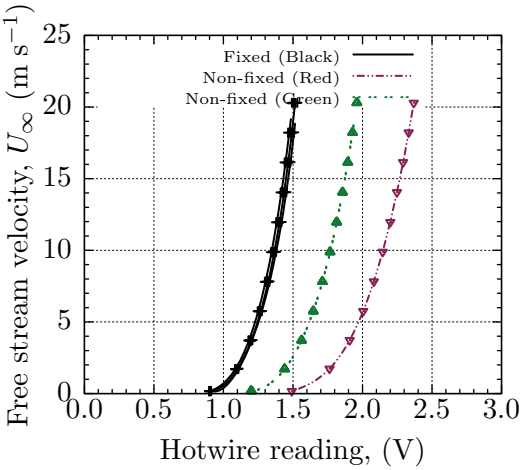


(a) Lateral measurements (13/05/2013). (b) Vertical measurements (23/07/2013).

Figure A.5: Hot-wire calibration: Uniform flow, Aligned upstream Rotor.

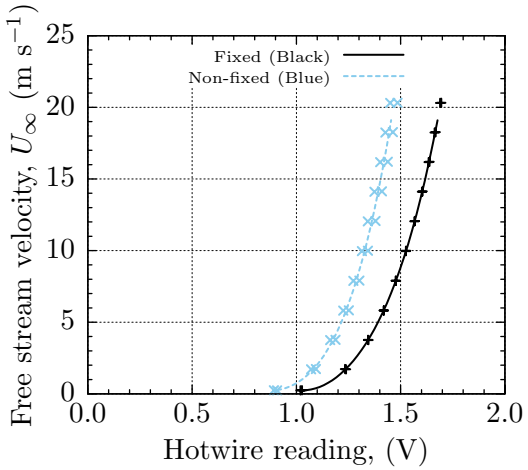


(a) Lateral measurements (25/07/2013).

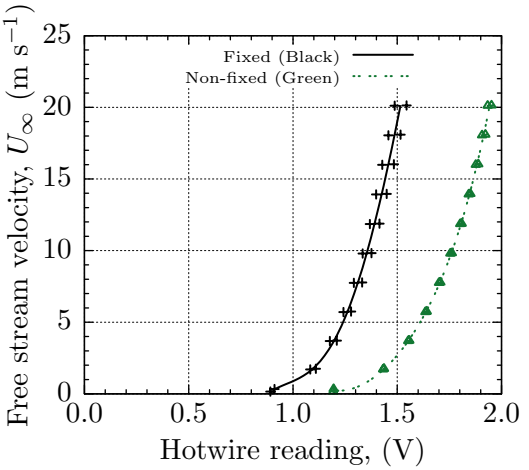


(b) Vertical measurements (19/07/2013).

Figure A.6: Hot-wire calibration: Uniform flow, 1D offset upstream Rotor.

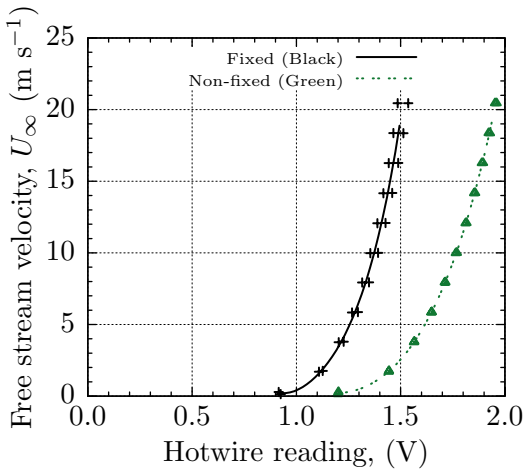


(a) Lateral measurements (12/05/2013).

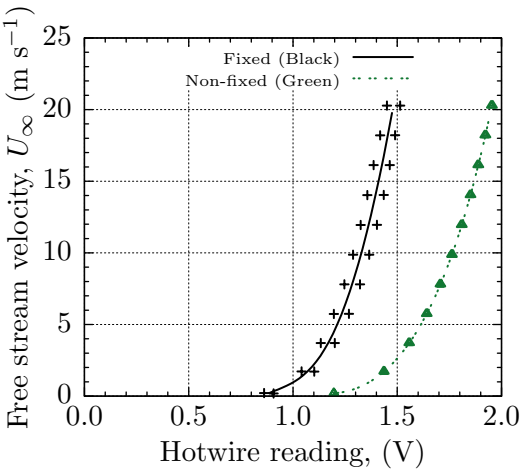


(b) Vertical measurements (22/07/2013).

Figure A.7: Hot-wire calibration: Turbulent flow, Aligned upstream Rotor.



(a) Lateral measurements (26/07/2013).



(b) Vertical measurements (20/07/2013).

Figure A.8: Hot-wire calibration: Turbulent flow, 1D offset upstream Rotor.

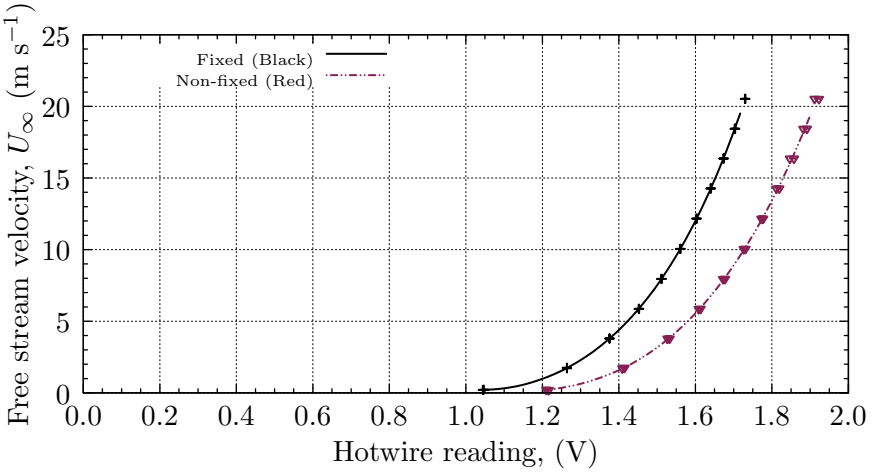


Figure A.9: Hot-wire calibration: Wake meandering (16/05/2013).

A.3 Tunnel

The free stream velocity measurements from the tunnel contraction pressure tappings were calibrated in order to ensure exact agreement with the velocities measured by the pitot tube. This was done by first calibrating a hot-wire at the downstream turbine position according to the method described in the previous section. The hot-wire calibration is shown in Figure A.10. The hot-wire was then used to record the velocities simultaneously with the contraction tappings, both for uniform inflow and with the fractal turbulence grid. The resulting calibrations are shown in Figure A.11. Applying a linear least squares fit yields $m = 0.99$ and $c = -0.02$ for uniform flow and $m = 1.33$ and $c = 0.02$ with the fractal grid installed.

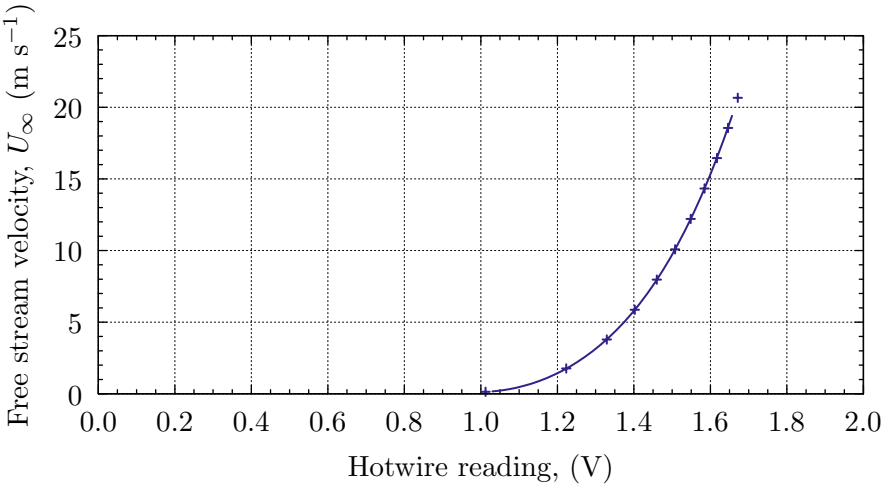


Figure A.10: Hot-wire calibration: Tunnel calibration (29/04/2013).

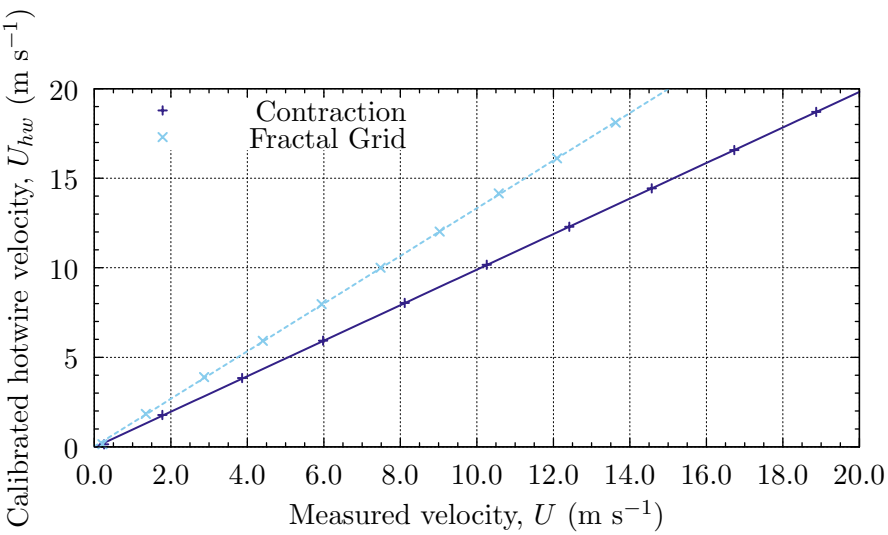


Figure A.11: Tunnel velocity calibration.